Full-field, Conformal Epiretinal Electrode Array Using Hydrogel and Polymer Hybrid Technology

by

Muru Zhou

A dissertation submitted in partial fulfillment
of the requirements for the degree of
Doctor of Philosophy
(Macromolecular Science and Engineering)
in the University of Michigan
2022

Doctoral Committee:

Professor Jinsang Kim, Co-Chair
Professor James D. Weiland, Co-Chair
Associate Professor Tim M. Bruns
Professor Brian Love

Muru Zhou

muru@umich.edu

ORCID iD: 0000-0002-5366-0470

Dedication

This dissertation is dedicated to my family. You are the lighthouse guiding me through the difficult sea. Thank you for your patient love and unconditional support.

Acknowledgements

The five-years journey is a sequence of moments spent with many amazing and special people. It is because of them that this journey glows and shines.

Thank you to my advisor, Dr. Weiland. I still remember the first meeting when you showed me Argus II. Your passion for science and engineering greatly encouraged me to pursue the path in retinal prosthesis. Your generous support and advice taught me more than academic knowledge. You also set a role model of how to be a person caring for others, treating people equally and loving life. Thank you for understanding many difficult circumstances of international students. I am very lucky to have you as my advisor.

Thank you to my co-advisor, Dr. Kim. Your profound knowledge and dedicated work have always motivated me as a scholar and researcher. Your guidance and encouragement taught me critical thinking and dealing with challenges and failures. You are my heart's best Macro program director, always caring and supportive. Macro keeps growing firmer and tighter with your leading.

Thank you to my committee members, Dr. Bruns and Dr. Love. You have generously shared your expertise and advice with me to better refine and construct the research.

Thank you to my lab mates Dorsa, Elena, Beomseo, Kate, Negin, Hojun, Wennan, and Swetha. I will miss those laughs and sighs we shared together working in the lab, having lunch, playing games, and hanging out. Your beautiful personality and wisdom always inspire me to be better. This is the best group and the best second family I can ever ask for.

Thank you to my friends in the Macro program, Shamalee, Ying, Mengjie, Shuqing, Yanan, Jiayue, Mira, Jiwon, and many others. I would like to specifically thank Shamalee for the two years together as the co-presidents of ACS POLY/PMSE, and for always being there for me with ups and downs. Thank you to my friends in Michigan, Hans, Julianna, Ouyang, Elissa, Bobby, Paras, Wenhao, Deokwon, Wenyi, Zihao, Ruiting, and Jingcheng. I am a lucky person to meet and know you. Your wise opinions, selfless support, and unconditional encouragement make me believe and persist during my Ph.D. Special thanks to Hans for the game nights, coco trips, and occasional presences of Dr. Pepper.

Thank you to my family. Mom, dad, grandpa, grandma, Cangkai, Wei, uncle Wang, aunt Ying, aunt Zhou, and many others. You listen to my cries and cheer for my success. Our love brings our hearts together even though we are so far apart physically.

Thank you to my partner, Shengtuo. Meeting you, knowing you, and falling in love with you at Ann Arbor are the most romantic things that happened to me. We hold hands to climb the hills and valleys. We never let each other fall. Our bond grows stronger and stronger. You showed me how to love and to care. With your generous love backing me up, I grow the courage to explore the unknown, and I cannot wait to begin the next journey with you.

Table of Contents

List of Tables

List of Figures

Abstract

Neural interfaces with good conformability and flexibility are highly desired for neural stimulation and modulation because they are close to the neural systems and have comparable mechanical properties with the tissue, therefore, improving the efficiency of the device and reducing neuronal loss. Notably, the retina requires a spherical interface with wide coverage and minimized surgical trauma. However, most clinically and commercially available electrode arrays are rigid and planar. A smart electrode array that incorporates advanced materials with shape reconfiguration ability is a potential solution to these challenges. In this thesis, I developed a full-field array with a hydrogel layer that can 1) cover a visual field of 113° based on the substrate size, 2) compact into a temporary shape before implantation, 3) deploy into a curvature that fits the retina by responding to moisture after implantation. The responsive full-field retinal array can maximize the coverage of vision restoration and minimize the scleral incision.

Developing the hydrogel and its hybrid system is the first step to achieving a responsive retinal array. I fabricated PDMS/hydrogel bilayer strips and investigated the relationship between the formed curvature and hydrogel properties. By increasing the initial monomer concentration of hydrogel pre-solution, the curvature of the bilayer strips increased. Timoshenko's model fitted with the experimental data well, identifying the effect of hydrogel properties on the curvature. The robust adhesion using benzophenone between PDMS and hydrogel guaranteed the long-term salability of the bilayer in the aqueous environment.

Fabrication of electrodes and metal traces on flexible materials such as PDMS is challenging. I experimented with two different protocols to fabricate electrode arrays. Parylene C

coated PDMS as the substrate resulted in a low yield of functional electrodes and a cracked surface. Eventually, I combined a PDMS substrate (for hydrogel bonding) with a polyimide electrode array (for robust electrical connections) with a total thickness of around 240 μm. Polyimide functioned as the substrate and the insulation layer for electrodes. The top layer of PDMS, with manually opened electrode sites, functioned as the interface with the hydrogel layer, while the bottom layer of PDMS provided mechanical support. The electrode array was shaped as a 6-petals flower via laser ablation.

Artificial vision generated from retinal prosthesis highly relies on the efficient electrical charge transfer, but adding a hydrogel layer to the electrode array carried the risk of blocking charge transfer. I coated the multilayered electrode array with hydrogel, characterized the electrical performance of the electrodes, and investigated the feasibility of implantation using *ex vivo* pig eyes. Electrodeposition of a film of Pt/Ir alloy significantly lowered the impedance at 1 kHz by 91.54% and improved the charge storage capacity of the electrodes. In addition, electrodeposition reduced the variation induced by contaminations. Hydrogel coating compromised the electrical properties but still maintained better performance compared with electrodes before electrodeposition. An equivalent circuit model was used to further analyze the effects of electrodeposition and hydrogel coating. Then, the full-field array was compacted into a temporary shape and inserted into pig eyes *ex vivo*. The full-field array was self-deployed into a 3D curved surface fitting to the retina once implanted. The electrodes demonstrated similar electrical performance after implantation compared with before implantation.

The smart full-field electrode array can improve not only epiretinal prostheses but also provide novel solutions for other neural interfaces preferring conformability and flexibility.

Chapter 1 Introduction

1.1 Neural interfaces

Neural interfaces are electrical devices interacting with neural systems [1]. Neural interfaces utilize electrodes to record, activate, and/or inhibit nearby neurons. For stimulation, the electrode will create a voltage field that causes ions to move to depolarize neurons and initiate action potential firing, modulating neural functions [2]. While in recording, the signals from the action potential of neural activity will be detected by electrodes, which enables decoding of neural circuit function [3]. Since the first electrical shock from a torpedo fish was used on humans, neural interfaces have been widely used in various clinical applications [4], including prostheses for spinal cord injury [5], deep brain stimulation to treat Parkinson's disease, dystonia, epilepsy, and tremor [6], spinal cord stimulation for chronic pain [7], cochlear implant to restore hearing [8], and retinal and cortical prosthesis to restore vision [9].

The early work in neural interfaces, including the Utah array [10] and Michigan probes [11], are fabricated using silicon, glass, and metals. They are commercially available tools and widely used in preclinical research. Silicon has Young's modulus of more than 100 GPA [12], which causes a significant mechanical mismatch compared with neural tissues, which typically have Young's modulus of a few hundreds of Pa to kPa (**Figure 1**). This stiffness allows neural interfaces to penetrate into the brain with a driving force, but long-term consequences of the stiffness mismatch is significant loss of neurons [13]. While microelectrode arrays are commonly made in planar structures, neural structures are contoured, and planar arrays do not conform well with dynamic and irregular neural tissues, increasing the contact impedance and electrical

stimulation threshold [14]. Additionally, stiffness and non-conformability result in relative motion on the interface, inducing random mechanical strain on the interface [15]. Even worse, those limitations can contribute to the foreign body response generated from the targeted neural tissues, resulting in tissue damage, low efficiency of stimulation, and even device failure [16], [17]. Other factors, including surface geometry and roughness, chemistry properties, and duration of contact and implantation, can also determine the reliability and biointegration of the device [18].

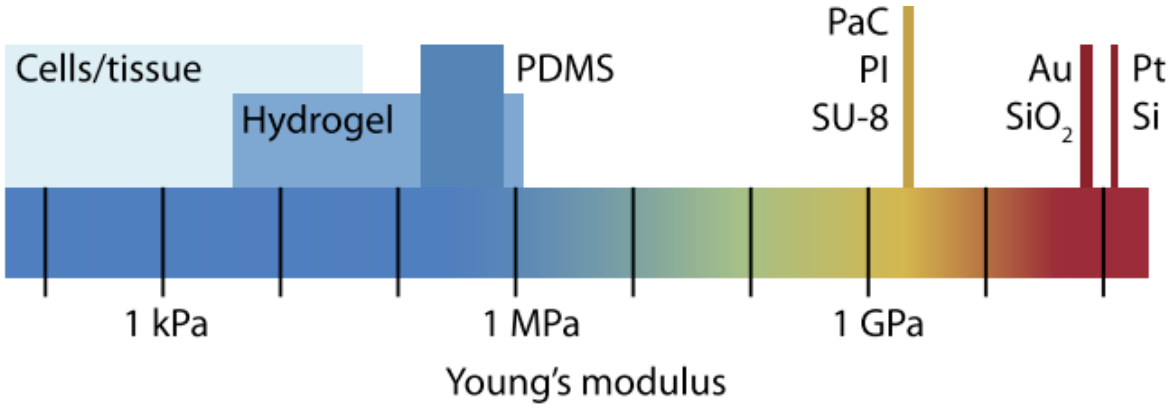

Figure 1 Young's modulus of tissues and common materials used in electrode array fabrication. Adapted from [19].

Researchers have explored different approaches to reduce mechanical mismatch and improve the conformability of neural interfaces. Surface coatings using biocompatible and soft materials [20], geometry modifications fabricating minimized shanks [21], serpentine and fractal shapes [22], and mesh designs [23], materials that are intrinsically soft and flexible to fabricate electrode arrays [24], bioabsorbable materials [25], and adaptive electrode arrays [26] are explored as potential options for next-generation neural interfaces. Other neuromodulation technologies that do not require an electrical neural interface include magnetic stimulation, ultrasound, and optogenetic therapy [27].

Adaptive neural interfaces using smart and responsive materials show potential as the next-generation conformable bioelectronic implants. Neural tissues like the peripheral nerve and the retina have three-dimensional structures and neural interfaces with good conformability will improve recording and stimulation efficiency. In addition, responsive electrode arrays can be made via traditional planar procedures and coated with shape-morphable polymers post fabrication. Adding the polymer as the final step removes the requirement that the adaptive polymer tolerates all the steps of fabrication, which can include aggressive etchants and high temperatures. Neural interfaces with shape memory polymers are reported to change the shape into a three-dimensional (3D) structure after implantation to conform to the peripheral nerves [28], [29], and the retina [30]. Electrode arrays using novel adaptive materials with viscoelastic properties [31] and softening ability [32] are reported to adapt to the mechanism of tissues. With conformable neural interfaces, fragile and soft neural tissues will experience less strain and compression, thus, less damage and foreign body responses.

The retina, having a curved surface and delicate structure, could benefit from the conformability and flexibility of the adaptive neural interface. Retinal prosthesis is one of the commercially available treatments for patients with retina degeneration diseases. The following introduction will provide a thorough overview of the state-of-art technologies and achievements of retinal prosthesis.

1.2 Retinal prosthesis

Retinitis pigmentosa (RP) is one of the leading and incurable forms of retinal degenerative diseases, often leading to blindness [33]. Statistically, RP affects 1.5 million people

worldwide [34]. As human life spam extends nowadays, a growing population suffers from the consequences of RP [35].

RP is typically characterized as the dysfunction of cone and rod photoreceptors [36]. Individuals with RP usually experience sequential loss of night vision, peripheral vision, and central vision, which will eventually progress into blindness [37]. For individuals in the early stage of RP, therapies coping with complications and supportive management can slow down the progression [38], but there is no cure for RP. Other treatments, including retinal prosthesis [39]–[41], optic nerve and cortical prosthesis [42], gene therapy [43], regenerative medicine [44], and neuroprotective agents [45] are at various stages of development for patients at different stages of RP [46].

Although gene therapy targeting a *RPE65* mutation has shown promising improvement in patients in clinical trials [38], RP can results from a large number of distinct genetic mutations. Each mutation will require its own treatment, and most are more complicated compared to RPE65. More genetic targets need to be uncovered to benefit a larger population of patients [47]. Other clinical trials of regenerative stem cells and neuroprotective agents are opening more potentials for RP patients but still are far from commercialization [44], [45].

Among all the treatments, the retinal prosthesis is approved commercially. Retinal prosthesis utilizes the relatively intact inner retina and injects electrical pulses to the remaining neural cells to evoke phosphenes in users [48]. Although far different from normal vision, retina prostheses can improve the blind individuals' ability to localize objects, discriminate motion, and even read letters [49], [50]. In general, the quality of generated vision depends on the resolution of electrodes, the stimulation strategy, training program, and visual perceptions of individuals.

Depending on the position of the implantation, retinal prostheses are classified as epiretinal, subretinal, and suprachoroidal prostheses (**Figure 2**) [51]. The epiretinal prosthesis is placed on the inner side of the retina in the eye and aims to stimulate bipolar cells or retinal ganglion cells (RGC). The surgery of implanting epiretinal prosthesis is more established and the relatively ambient space allows wide-field prostheses. However, epiretinal prostheses usually require tacks to fix them in position. Additionally, electrical stimulation near the nerve fiber layer can lead to off-target activation. The subretinal prosthesis is placed between the bipolar cells and retinal pigment epithelium (RPE). In this location, the distance between the electrodes and the bipolar cells is decreased to improve stimulation efficiency, but the space to implant the microelectrode arrays is limited, and surgeons are less familiar with the implantation procedures [52]. Alpha-IMS, with the European Conformity (CE) mark, is one of the examples of the subretinal prostheses and has been reported to reach the visual acuity of 20/546 in patients [53]. PRIMA implant, a subretinal photovoltaic device, has demonstrated the visual acuity of 20/460 on patient [54]. The suprachoroidal prosthesis is placed between the choroid and the sclera. The simplification of the surgical process makes the implantation less invasive, but the stimulation has decreased efficacy and lower spatial resolution because of the increased distance from the target neurons [55].

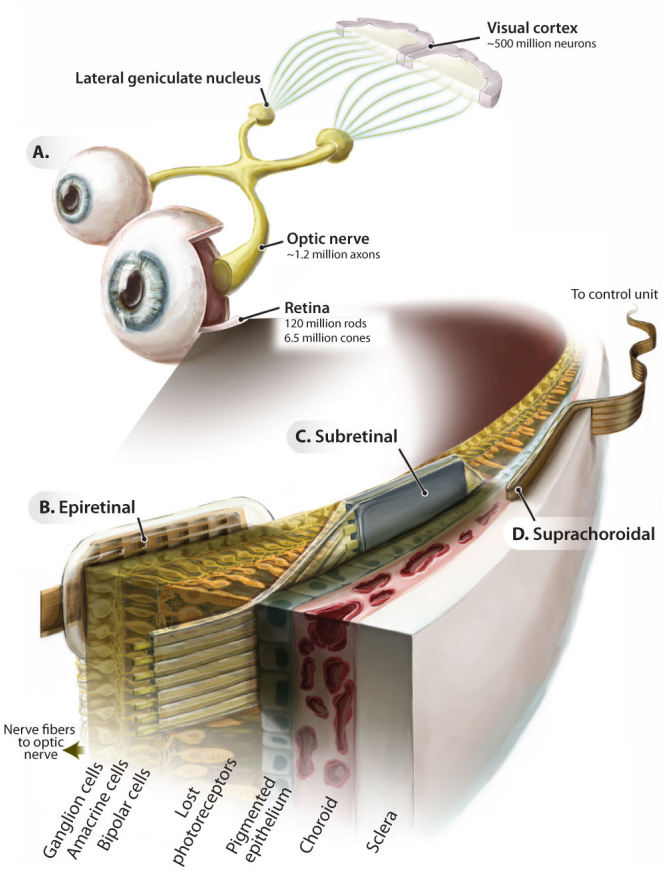

Figure 2 Pathway of visual signals and implantation locations of different retinal prostheses, including epiretinal, subretinal, and suprachoroidal prostheses. Adapted from [51].

1.2.1 Epiretinal prosthesis

The most well-known example of epiretinal prostheses is Argus II (Second Sight Medical Products Inc., Sylmar, CA, USA), approved by both Food and Drug Administration (FDA) and CE for blind individuals with RP. Argus system has an external camera on the glass frame to capture the surrounding environment of the user. Then, the data of the image will be transmitted to the video processing unit (VPU) and coded into signals to be used by the implanted retinal stimulator. Eventually, the multielectrode array placed on the inner layer of the retina will stimulate retinal cells to induce phosphenes [56]. Argus I was an investigational device with 16 electrodes in a 4 x 4 array with alternating electrode diameters of 250 μm and 500 μm [57]. The

refined Argus II consists of 60 platinum grey electrodeposited electrodes with a diameter of 200 μm with 520 μm spacing, and covers a visual field of approximately 11° × 19° (~22° diagonally) [58]. The implantation of the Argus II electrode array requires an incision on the sclera of 5 mm [59]. The best reported visual acuity achieved by Argus II is 20/1260, which is still defined as legally blind [9]. Patients' ability of object localization, motion discrimination, mobility, discrimination of oriented gratings, and even letter reading have been improved with the implantation [49].

Other epiretinal prostheses are under clinical trials, including the Intelligent Retinal Implant System (IRIS), 256-channel Intelligent Micro Implant Eye (IMIE 256), and EPI-RET 3. The newest version of IRIS II developed by Pixium Vision has an electrode array of 150 electrodes and was approved by CE in 2016 [60]. IMIE 256 has slightly larger coverage than Argus II with 256 electrodes [61]. EPI-RET 3 is refined from its previous version and intends to cover a large area on the retina with a visual field of 37° [56].

1.2.2 Limited coverage of epiretinal prosthesis

Studies have shown that the loss of peripheral vision can greatly impair the mobility of individuals [62]. A simulated study of real and virtual mobility tests suggests that 16 x 16 electrodes covering a 27° × 27° visual field can help inexperienced individuals with navigation ability, and a lower resolution of 60 electrodes may help users achieve the same level of performance with training [63]. In reality, in addition to the coverage of the visual field and resolution of electrodes, other factors also affect the capacity of stimulation, including cortical plasticity [64], patients training [65], and retina physiology [66].

However, current epiretinal electrode arrays anticipating human studies usually cannot provide enough coverage, and Argus II as an example only covers an area of 3 x 5 mm on the retina [67]. The monocular visual field of healthy individual consists of a 30° central vision, and the peripheral vision extends to 100° laterally and upward and 75° downward [68]. Argus II theoretically can cover a maximum visual field of around 11° × 19°, which is still far below the central visual field. Suprachoroidal prostheses allowing a larger electrode array have sizes up to 17 mm x 8.5 mm, but the resolution is relatively low, consisting of 44 electrodes, each with a diameter of 1 mm [69]. The limitation of the dimensions of the state-of-art retinal arrays comes from the requirement of minimizing the scleral incision to avoid post-surgery complications. In addition, most retinal arrays are fabricated using relatively rigid materials like polyimide and cannot match the curvature of the retina [70]. Nevertheless, increasing the size of an array made with rigid materials and planar shapes leads to more damage and further distance between the electrode and the retina [71], eventually leading to an increased threshold and decreased efficiency of stimulation [72]. Some retinal electrode arrays are made from flexible materials such as silicone, but fitting a planar sheet of silicone to a curved surface requires designed geometry to prevent buckling and wrinkling of the sheet [73]. To develop a wide-field retinal array, improving the coverage and the conformability of the electrode array are equally necessary.

1.2.3 State-of-art wide-field retinal arrays

Researchers approach wide-field retinal prostheses with different methods, including modifications of geometries of the shape of the prosthesis and utilization of new materials.

Some designed geometries allow electrode arrays with a planar shape to achieve curved surfaces. The study demonstrates a wide-field dummy polyimide array with two movable peripheral arms to form a curvature once implanted, and the array is expected to cover a visual field of 34° [74]. The flexibility of polyimide allows the folding of the array into a compact shape to some extent. Although the peripheral arms can move and create a local curvature, the main and central area of the polyimide array remains planar. A similar design utilizes various geometries based on the projections of a sphere into a flat surface to produce polyimide-based electrode arrays, but the multi-armed polyimide device imposes significant difficulty in compacting each arm during implantation [75]. Another study produces a truncated icosahedron design of an optoelectronic device based on polyimide. The device demonstrates a fitting curvature and wide coverage on the rat retina, but further enlarging the device to fit the human retina can make the manipulation of the segmented device difficult [76]. A parylene-based wide-field array that can be folded into an origami structure demonstrates the possibility of deployable arrays [77]. However, patterning electrodes on such a substrate can be challenging because the small angles required by the folding process can possibly break electrical connections. Also, the manual deployment of the origami device is time-consuming and complicated. Other than using the array itself to create the curvature, it is also possible to use a supporting structure with a predetermined curvature. A photovoltaic array consistsing of high-resolution islands of electrodes on a polydimethylsiloxane (PDMS) substrate shows its flexibility and softness to be attached and adapted to dome-shaped support. Therefore, the electrode array attached to the dome-shaped support achieves a curved surface. Both the electrode array substrate and the support are made from PDMS and can be folded during the implantation [78]. The photovoltaic array has no need for cables and conductive tracks, which allows more freedom for folding, but

the unfolding process triggered only by the elasticity of PDMS is not controllable. With a large electrode array covering a visual angle of 46.3° as the photovoltaic array, uncontrolled unfolding can impose a potential risk of damaging the retina.

In addition to geometry modifications, integrating novel material with shape reconfiguration ability opens new avenues for wide-field arrays. A 126 channeled microelectrode array with a shape memory polymer coating self-unfolds once implanted [30]. Shape memory polymer coated on the polyimide electrode array responds to temperature and allows the electrode array to have a customized curvature depending on the mold used. The array can be fixed manually at a compact temporary shape before implantation. When presented to body temperature, the shape memory polymer gradually recovers its permanent and predesigned 3D shape. Nevertheless, the array with the shape memory polymer coating is still relatively small (10 mm x 10 mm) and the shape memory polymer has Young's modulus of 1.10 MPa, which still has a mechanical mismatch with the retina [79]. Shape-morphable materials prove their potential in wide-field arrays and are worth exploring broadly.

By combining the smart and responsive materials with electrode arrays, the retinal prosthesis can have the final shape, the temporary shape, and the unfolding process all in a controllable fashion. Therefore, a smart retinal implant with 1) large coverage of the retina for maximal restoration; 2) compact temporary shape to minimize the incision; 3) curvature fitting the retina to increase efficiency; 4) tunable curvature for personalized therapy can greatly advance the development of retinal prostheses.

1.3 Smart materials that change shapes

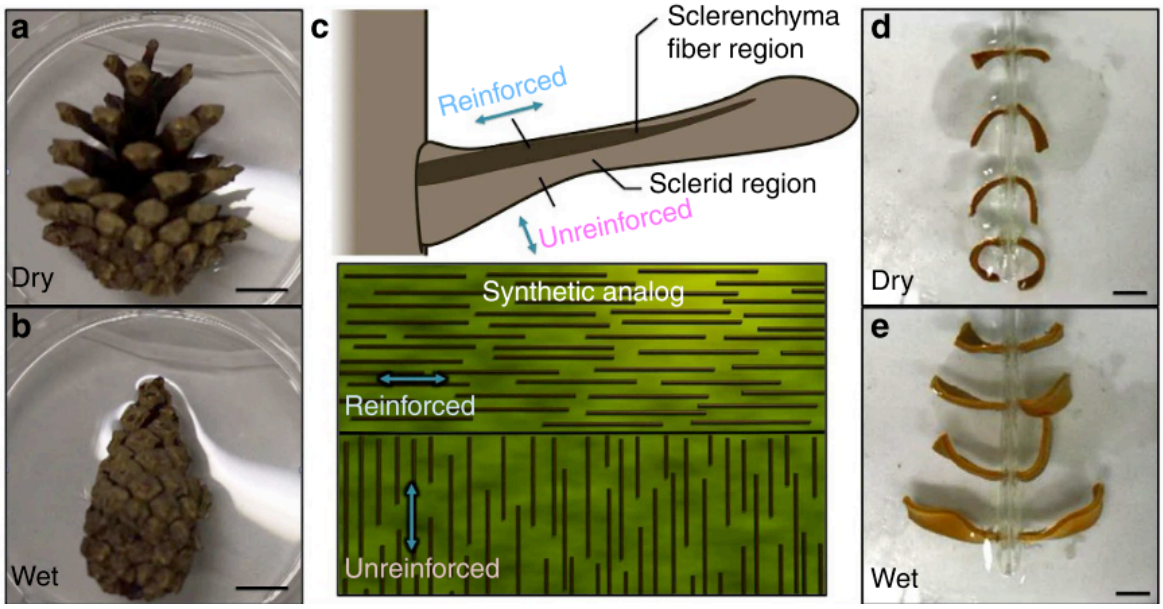

Figure 3 Pinecones have special structure to open or close scales responding to different levels of humidity. Adapted from [82].

The abundance of shape-morphable materials provides researchers with a vast toolkit to select from. The development of shape-changing materials was greatly inspired by nature, in which many living creatures transform their shapes in different conditions [80]. For example, pine cones close or open their scales according to the humidity in the atmosphere (**Figure 3**) [81]. Similarly, synthetic shape-morphable materials are designed to respond to external stimuli and undergo shape transformation to reach a rationally designed shape [82]. They have attracted attention from researchers because of their wide range of applications, not limited to robotic actuators [83], cell therapy and medicine [84], tissue engineering [85], sensors [86], and neural interfaces [26].

Shape-morphable materials consist of a wide range of materials, including shape memory polymers, polymer composites, liquid crystals, and hydrogel [87]. Shape-morphable materials usually experience changes in volume, twisting motion, and bending motion, leading to shape

reconfiguration when responding to various external stimuli, including temperature, magnetic field, electrical field, pH, light, and biomolecules. The reconfigured shape responding to stimuli is usually a predetermined 3D shape. Some materials, for example, the shape memory polymers and hydrogel, can be fixed at a temporary shape [88]. The permanent shape and the temporary shape can be designed and customized to meet different needs.

Electrode array fabrications are mainly producing planar arrays. Shape-changing materials have the advantage of transforming from a planar status into a complex and programmable geometry. This advantage allows electrode arrays combined with shape-morphable materials to have a complicated 3D shape with traditional microelectrode arrays fabrication processes. Different research groups use shape memory polymers for epiretinal implants [89] and peripheral nerve implants [28], [29],[90] and demonstrate both geometrical and mechanical fit with the target tissues.

Among the different shape-changing materials, hydrogels are notably promising because of their softness, excellent shape transformation ability, and good biocompatibility [91]. Recently, advances in fabricating and patterning hydrogel have paved for broadening the applications of hydrogel as the shape actuator [92]. Hydrogel itself usually has a good permeability of water and gas, thus hydrogels in general cannot be used as electrical insulators However, hydrogel hybridized with different layers of materials allow differentiating functions of each layer (**Figure 4**) [93]. Therefore, a hybrid structure consisting of the electrode array and a shape-changing hydrogel layer could be an excellent option for responsive electrode arrays.

Hybrid materials with laminated structures should have robust and long-lasting adhesion between each layer. Different bonding techniques have been applied to bond hydrogel with materials that are commonly used as substrates for electrode arrays, including PDMS and

polyimide [94]–[96]. In addition to hydrogel, integrating flexible materials into the hybrid layers can further improve the overall flexibility and softness of the electrode array.

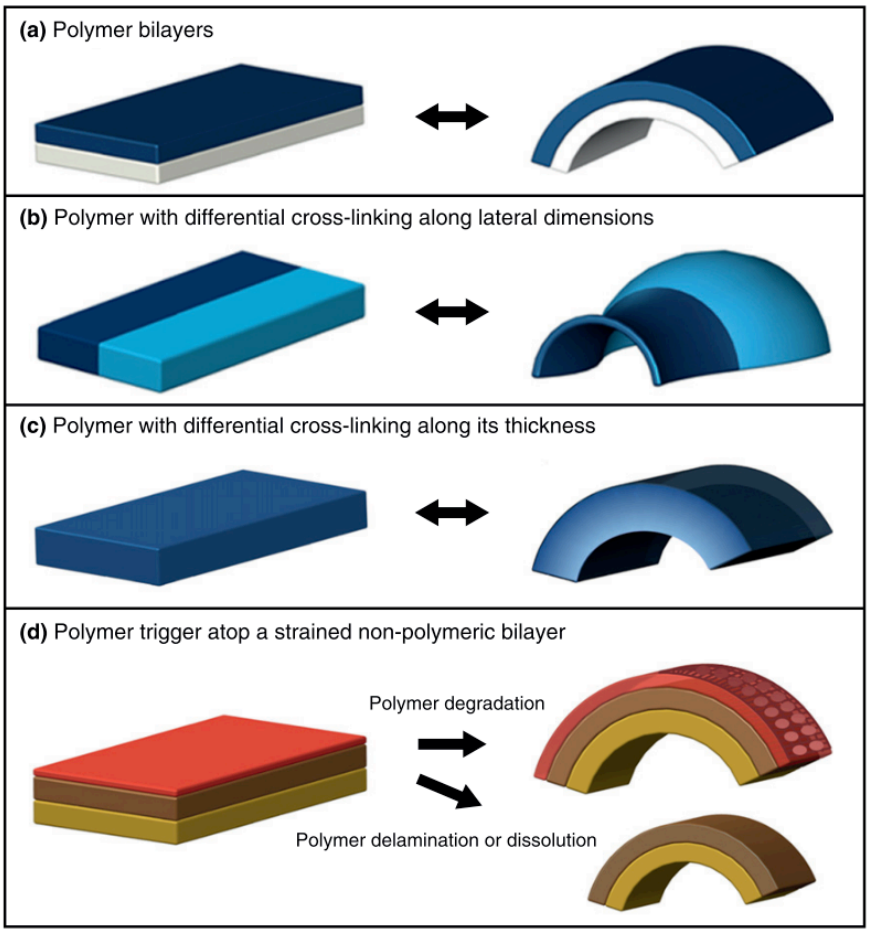

Figure 4 Different patterns of shape transformation using hydrogel. Adapted from [94].

1.4 State-of-art fabrication of electrode arrays on mechanically compliant substrates

Many different factors contribute to the mechanical compliance of the electrode array. Ultra-thin substrate [97], geometrical variations of conductive tracks [98] and pre-buckling [99], and intrinsically soft materials [100] are all different ways to achieve flexibility and stretchability to some extent. Among all, silicone, an intrinsically soft material with good biocompatibility, has shown great potential as the substrate for the next generation of flexible neural interfaces [101].

However, fabricating electrodes and leads with high resolution on mechanically compliant substrates is not easy due to the low chemical and thermal stability of those materials. For instance, PDMS has a high heat expansion coefficient, significant volume change in the vacuum and organic solvents, and high sensitivity to various surface treatments. Therefore, traditional microelectrode array fabrication procedures on PDMS lead to low yield of functional connections and limited lithographic resolution [102], [103]. Different studies have demonstrated novel procedures to fabricate electrodes on silicone. As for metal electrodes, an epidural neural interface uses the shadow mask and screen printing to fabricate electrodes on PDMS, and it is implanted not only in rats but also in primates [24], [100], [104]. In addition, the utilization of flexible and conductive composites as electrode materials shows good compatibility with PDMS [105]–[107].

Other materials that are commonly used in electrode array fabrication, including polyimide, parylene C, and SU-8 are more compatible with microelectrode array fabrication procedures. Using those materials as the substrate and insulation layer for the electrodes, then combining them with PDMS can yield a high resolution of electrodes and guarantee flexibility of the overall device at the same time [108]–[110].

1.5 Summary of thesis

In this thesis, I design and develop a smart epiretinal prosthesis with hydrogel to provide wide-field coverage for vision restoration and minimize sclerotomy to prevent surgical trauma. In addition to the retinal prosthesis, the technique of combining shape-morphable hydrogel and electrode array can apply to other neural interfaces requiring 3D shape, good conformability, and softness.

In Chapter 2, I fabricate and characterize the PDMS/hydrogel bilayer strips to study the feasibility of the bilayer system as the substrate for epiretinal prosthesis [111]. I design the fabrication process to produce a reliable PDMS/hydrogel bilayer. I test two methods to bond PDMS and hydrogel robustly. I also investigate the relationship between the curvatures of the bilayer and the hydrogel properties by varying the initial monomer concentration of hydrogel pre-solution. I also fit the experimental data to Timoshenko's model. I identify the relationship between the curvature and hydrogel pre-solution formula, which can be used as rational design guidance to achieve the desired curvature in future bilayer systems. The robust adhesion between PDMS and hydrogel, along with the intrinsic flexibility and softness of PDMS provide justification for fabricating the electrode array using PDMS.

In Chapter 3, I test two fabrication routes to yield reliable electrodes on flexible substrates. I first fabricate electrodes on PDMS with a parylene C intermediate layer. I identify the challenges in this process, including cracking of metal traces and ineffective opening of electrode sites on PDMS. Therefore, I adopt another method and use polyimide as the substrate and the insulation for metal electrodes and traces, then the polyimide-based electrode array is sandwiched between two layers of PDMS. PDMS provides mechanical support for the electrode array and functions as the interface with the hydrogel. I verify this fabrication protocol can guarantee a stable yield of functional electrodes.

In Chapter 4, I characterize and evaluate the full-field array coated with hydrogel. I analyze the results of electrical properties and simulation surgery. I evaluate the effects on electrical properties after different treatments on the electrodes, including electrodeposition of platinum/iridium alloy, coating with hydrogel, and acute *ex vivo* implantation in porcine eyes. I investigate the feasibility of implanting the full-field array in porcine eyes using simulated *ex*

vivo surgery. I verify the full-field array can be compact in a temporary status before implantation and self-deploy in porcine eyes after implanted.

In summary, this thesis develops and evaluates a full-field array that can respond to moisture and reconfigure from a compact status into a 3D curvature to fit the retina. This thesis can lay a foundation for next-generation wide-field retinal prosthesis and other applications that require good conformability to the target tissues.

Chapter 2 Shape Morphable Hydrogel/Elastomer Bilayer for Implanted Retinal Electronics

A version of this chapter has been published in the Micromachines.

M. Zhou, D. H. Kang, J. Kim, and J. D. Weiland, "Shape morphable hydrogel/elastomer bilayer for implanted retinal electronics," *Micromachines*, vol. 11, no. 4, p. 392, 2020.

2.1 Abstract

Direct fabrication of a three-dimensional (3D) structure using soft materials has been challenging. The hybrid bilayer is a promising approach to address this challenge because of its programable shape-transformation ability when responding to various stimuli. The goals of this study are to experimentally and theoretically establish a rational design principle of a hydrogel/elastomer bilayer system and further optimize the programed 3D structures that can serve as substrates for multi-electrode arrays. The hydrogel/elastomer bilayer consists of a hygroscopic polyacrylamide (PAAm) layer cofacially laminated with a water-insensitive polydimethylsiloxane (PDMS) layer. The bonding agent between the two layers was initially with 3-(Trimethoxysilyl)propyl methacrylate (TMSPMA), and then optimized by using benzophenone instead. The asymmetric volume change in the PAAm hydrogel can bend the bilayer into a curvature. We manipulate the initial monomer concentrations of the pre-gel solutions of PAAm to experimentally and theoretically investigate the effect of intrinsic mechanical properties of the hydrogel on the resulting curvature. By using the obtained results as a design guideline, we demonstrated stimuli-responsive transformation of a PAAm/PDMS

flower-shaped bilayer from a flat bilayer film to a curved 3D structure that can serve as a substrate for a wide-field retinal electrode array.

2.2 Introduction

Flexible and soft shape-morphing materials undergo shape transformation when responding to certain stimuli and have gained an increasing interest in both research and industry [112]–[114]. The hybrid bilayer is one feasible and promising approach to create a soft, shape-changing material. A hybrid bilayer consists of a responsive layer, which can contract or expand when responding to a given stimulus, and a passive layer, which constrains the motion of the responsive layer. Torsion, bending, and buckling can be generated by the residual stress and eventually lead to the shape transformation from a two-dimensional (2D) to a three-dimensional (3D) structure [115], [93]. Hybrid bilayers have various applications including cell encapsulation [116]–[118], drug delivery [119], micro robots [120], actuators [83], [121], [122], and flexible electronics [28]–[30], [123], [124].

Metallic bilayer actuators [125], [126] have a long history in sensing, but exhibit small shape changes and usually are responsive only to temperature change. In contrast, hydrogels can respond to various stimuli, including temperature, pH, light, chemicals, and electrical field [127] and have a larger extent of shape change [118]. When hydrogel is constrained by the passive layer with a different swelling property, the swell or de-swell of the hydrogel can induce internal residual stress and result in shape transformation. The transformed shape is determined by the mechanical properties of each layer, the thickness ratio between the two layers, and also the dimensions and size of the bilayer. Studying how those parameters affect the final shape can help to design the shape transformation precisely and rationally. Kim et al. have studied the shape transformation of a hydrogel bilayer with different thickness ratios between the two layers [128].

Stoychev et al. have reported that the folding behavior varies with the aspect ratio of the hydrogel bilayer [129]. However, less research has focused on varying the intrinsic mechanical property of hydrogel to tune the transformed shape. Intrinsic properties of hydrogel can be modulated by varying the initial monomer concentration [130], cross-link density [131], initiator concentration [132] of the pre-solution, and also the ultraviolet (UV) intensity for photo-curing [133]. Decoding the relationship between intrinsic properties of hydrogel and the 3D structure of the bilayer can help to guide bilayer fabrication to achieve the ideal shape transformation, as a necessary first step towards more complicated designs and applications. For example, the bilayer has the potential to be used as a substrate for epiretinal prosthesis. Current retinal electrode arrays stimulate only the central retina, due to the size limit of the array for implantation [59]. A compact array that can gradually unfold to a desired curvature to reach peripheral retinal areas will expand the visual field of the retinal implant patient [30], [74], [75], [77], [78]. The potential application of the bilayer for epiretinal electrode arrays requires the fine-tuning of the programed 3D structure.

Here, we investigated the effect of intrinsic properties of hydrogel on the transformed shape using a hydrogel/elastomer bilayer system responsive to moisture. The findings from this study will provide design guidance for a wide-field epiretinal electrode array. The responsive part of the bilayer consists of polyacrylamide (PAAm), a biocompatible, and soft hydrogel. Polydimethylsiloxane (PDMS) acts as the passive layer because PDMS is a common soft electrode array substrate. Benzophenone is chosen as a bonding promoter to prevent delamination between the two layers [94]. First, we fabricated the hydrogel/elastomer bilayer with different PAAm hydrogel properties by varying the initial monomer concentration in the pre-solution of PAAm hydrogel while keeping the same cross-linker ratio, the initiator ratio, and

the UV light intensity. The robust bilayers transformed from a flat to a curved structure in water without delamination. We found that the curvature of the bilayer increased with the initial monomer concentration of the pre-solution. A simple model agrees with the experimental data well and provides theoretical validation of our design. This result can help us to formulate the hydrogel pre-solution to achieve the desired curvature. Guided by the relationship between the intrinsic properties of hydrogel and the final shape, we demonstrated a flower-shaped bilayer for future retinal electrode array applications.

2.1. Materials and methods

2.2.1 Materials

Poly(N-isopropylacrylamide) (PNIPAAm; Sigma–Aldrich A3553; Mn ~40,000, Sigma–Aldrich, St. Louis, MO, USA), acrylamide (AAm; Sigma–Aldrich A3553; ≥99%), 2-hydroxy- 2-methylpropiophenone (Irgacure 1173; Sigma–Aldrich 405655; 97%), N, N′-Methylenebisacrylamide (MBAM; Sigma–Aldrich M7279; ≥99.5%), 3-(Trimethoxysilyl)propyl methacrylate (TMSPMA; Sigma–Aldrich 440159; 98%) and benzophenone (Sigma–Aldrich B9300; ≥ 99%) were purchased from Sigma Aldrich. Polydimethylsiloxane (PDMS; Dow Corning Sylgard 184 Silicone Elastomer Kit, Dow Corning, Midland, MI, USA) was purchased from Dow Corning. PAAm hydrogel layer was molded from a Teflon mold (65 mm × 40 mm × 0.1 mm (length × width × thickness)).

2.2.2 Fabrication of PDMS/Hydrogel bilayer with TMSPMA

PDMS prepolymer and its curing agent (10:1 weight ratio) were mixed with hexane for better spreading. The mixture was poured into an acrylic mold with a height of 0.5 mm, and

hexane evaporated after 20 minutes. Another laser-roughened acrylic sheet was flipped onto the mold to make one side of PDMS rough.

Following curing at 60 ℃ for 1 h, the rough side of PMDS was treated with oxygen plasma. The duration of oxygen plasma was varied and set as 1 min and 5 min to optimize the extent of hydrolyzation on PDMS. Dynamic contact angle (Ramé-hart instrument co., Succasunna, NJ, USA) was measured to characterize the hydrolyzation of the PDMS surface. Then, two different methods of depositing silane on the PDMS surface were explored: 1) PMDS film was immersed into the TMSPMA solution (100 mL deionized water, 10 μL of acetic acid, and 2 wt. % of TMSPMA) for 30 min [134]; 2) PDMS and a petri dish with 100 μL TMSPMA were put into a vacuum chamber, and TMSPMA was chemical vapor deposited (CVD). The duration of CVD was varied and set as 2 h, 12 h, 13 h, and 24 h. After the surface modification of PDMS, the pre-gel AAm solution was poured into a Teflon mold and covered by the PDMS elastomer. The pressure from the PDMS ensured the even distribution of the pre-solution in the mold. The pre-gel solution was cured under an ultraviolet lamp (ML-3500C, Spectroline, Westbury, NY, USA) for 5 min. After curing, the PDMS-hydrogel bilayer was immersed in deionized (DI) water at room temperature.

2.2.3 Fabrication of PDMS elastomer

PNIPAAm was used as the sacrificial layer between the PDMS and the glass slide. 10 mg/mL PNIPAAm in ethanol was spin-coated on glass slides with a spin speed of 4000 rpm for 60 s, using a spin coater (Solitec Spinner, Solitec Wafer Processing Inc., Milpitas, CA, USA) at the Lurie Nanofabrication Facility (LNF) at the University of Michigan. Then, the glass slides were heated at 80 °C for 90 s to evaporate the excess solvent [135]. PDMS prepolymer and its curing agent (10:1 weight ratio) was mixed for 2 min and degassed in a vacuum desiccator for 40

min. The mixture was carefully poured on the glass slide to avoid bubbles and spin-coated with a spin speed of 250 rpm for 30 s. The PDMS was cured at 80 °C for 2 h on a hotplate. After curing, the PDMS was patterned with a laser (HL40-5g “Hobby Advanced”, Full Spectrum Laser, Las Vegas, NV, USA) into rectangular strips (17 mm × 2.5 mm (length × width)) for later release.

2.2.4 Fabrication of PDMS/Hydrogel bilayer with benzophenone

Cured PDMS was immersed into benzophenone solution (10 wt% in ethanol) for 4 min. Then, PDMS was washed with methanol three times and dried in air. Different amounts of acrylamide (AAm) were dissolved in water to form pre-solutions with acrylamide wt% in the range of 5% to 20%. The cross-linker ratio (the weight ratio of MBAM to AAm) was fixed at 3.89%, and the initiator ratio (the weight ratio of Irgacure 1173 to AAm) was fixed at 0.356%. The pre-gel solution was poured into the Teflon mold and covered by the PDMS elastomer. The pressure from the PDMS insured the even distribution of the pre-solution in the mold. The pre-gel solution was cured under an ultraviolet lamp (ML-3500C, Spectroline, Westbury, NY, USA) for 5 min. After curing, the slides were immersed in deionized (DI) water at room temperature, and the bilayer strips were released. For the fabrication of the flower-shaped bilayer, the hydrogel covered only the petals, but not the center area, with a diameter of 3.8 mm.

2.2.5 Mechanical test

Tensile tests of PDMS and PAAm hydrogel were completed with Texture Analyzer (TA. XT plusC, Stable Micro Systems, Surrey, UK) at Van Vlack Lab at the University of Michigan. The testing strain speed used for PAAm hydrogel was 0.1 mm/s, and for PDMS was 0.5 mm/s. The testing samples were fabricated into a dog bone shape using an acrylic mold (gauge width 11

mm, gauge length 40 mm). The PAAm hydrogel dog bone had a thickness of 7 mm and the PDMS dog bone had a thickness of 0.3 mm. The Young's modulus data were calculated from the stress–strain curve of the hydrated hydrogel. The expansion strain of PAAm hydrogel was defined as the ratio of the difference in lengths between dried and swollen states to the length of the dried state ($expansion\ strain = \frac{length_{\text{hydrated}} - length_{\text{dried}}}{length_{\text{dried}}}$). The samples were immersed in ethanol overnight to de-swell, then put in an oven at 40 °C for 10 min to evaporate the ethanol thoroughly. After measuring the dimensions, the dried PAAm hydrogel was immersed in DI water overnight to swell and the dimensions were measured again to calculate the expansion strain.

2.2.6 Image analysis

Bilayer strips were put into DI water at room temperature until reaching stable configurations. A camera (D7200, Nikon, Tokyo, Japan) was used to take photos of the hydrated hydrogels, and the curvature analysis was done using the digital imaging processing software Fiji and the plugin Kappa. Kappa measured the curvature of each point on the bilayer spline, then the average of the curvature was used to represent the curvature of each bilayer strip. For imaging the morphology and adhesion of the bilayer interface, bilayer strips were pre-frozen in liquid nitrogen for 5 min and then freeze-dried for 24 h. The samples were imaged by scanning electron microscopy (SEM; TESCAN RISE, TESCAN, Brno, Czech Republic) at Michigan Center for Materials Characterization (MC2) at the University of Michigan. To get the thickness input for the computational simulation, the bilayer strips were dried using ethanol with the method mentioned above. Then, the fully dehydrated bilayer strips were imaged with SEM to determine the thickness of PAAm hydrogel and PDMS. The input PDMS thickness was set as 300 μm, and

the PAAm hydrogel thickness was normalized according to the actual PDMS thickness as: 74.5 μm (5 wt%), 77.9 μm (7 wt%), 87.7 μm (10 wt%), 96.4 μm (15 wt%), and 196.1 μm (20 wt%).

2.3 Results

2.3.1 Fabrication of PDMS/Hydrogel bilayer using TMSPMA

To produce a thin layer of PDMS, we used hexane to dilute the mixture of PDMS pre-polymer to better fill the mold. A laser-roughed acrylic sheet was flipped onto the mold to fabricate a PDMS film with one side rough [95]. Then, we used oxygen plasma to hydrolyze the surface of PDMS to react with the following TMSPMA. Dynamic contact angle tests showed that 5 min of oxygen plasma significantly enhanced the hydrophilicity of the PDMS surface (**Figure 5**). Then two different methods were tried to deposit the silane, TMSPMA, on PDMS, shown in **Figure 6**. First, we immersed the PDMS film into the TMSPMA solution (100 mL deionized water, 10 μL of acetic acid, and 2 wt. % of TMSPMA) to graft silane [134]. However, the PDMS film became partially opaque and viscous after soaking in the solution for 30 minutes, which might indicate both the inhomogeneous surface modification and potential degradation of PDMS.

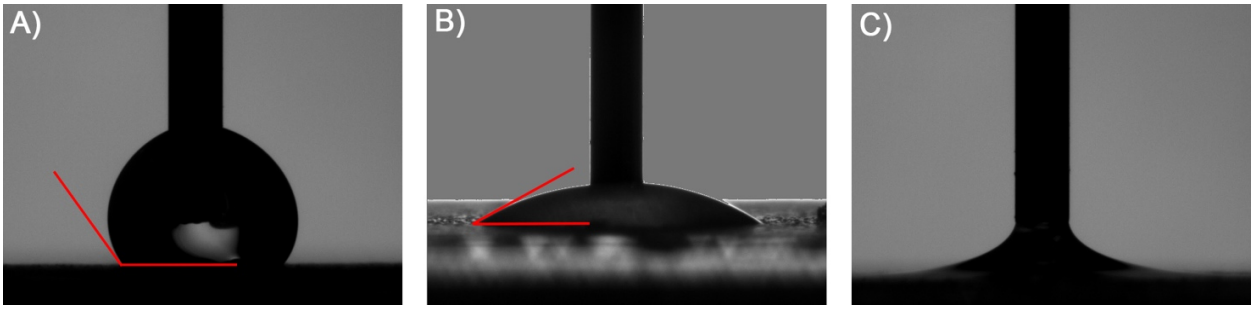

Figure 5 Dynamic contact angle of PDMS surfaces after different treatments. Deionized water acted as the wetting agent. Red lines labeled the contact angle. (a) native PDMS surface with no treatment. The contact angle was around 128 degrees. (b) PDMS surface after 1 min of oxygen plasma. The contact angle decreased to around 30 degrees, which suggested the presence of hydroxy groups. (c) PDMS surface after 5 min of oxygen plasma. The contact angle was not measurable because the surface was completely wetted by water.

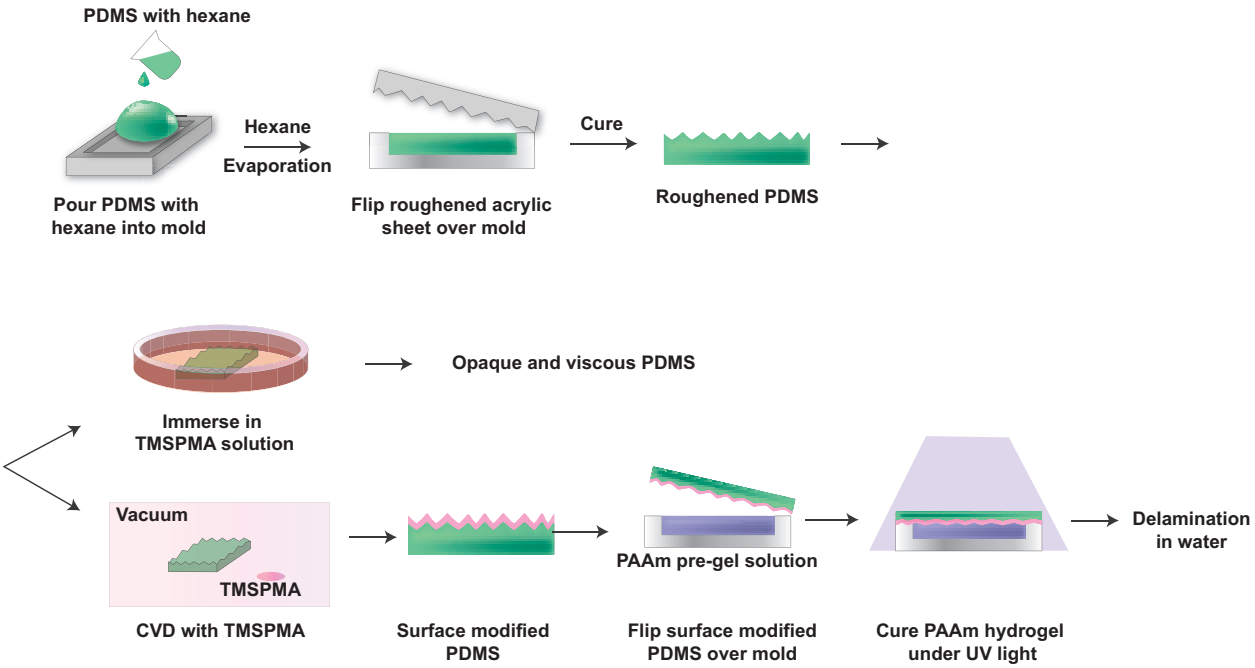

Figure 6 Schematic illustration and results of the fabrication of the hydrogel/elastomer bilayer with TMSPMA.

Because of the unsuccessful surface modification using the TMSPMA solution, we adopted CVD to graft TMSPMA onto the PDMS surface instead. We put oxygen-plasma-treated PDMS film and a petri dish with TMSPMA into a vacuum chamber for a period. To optimize the adhesion, we also varied the duration of CVD (2 h, 12 h, 13 h, and 24 h). Then we coated the surface with a layer of hydrogel. Although CVD preserved the integrity and transparency of PDMS, no matter how long CVD lasted, the bilayer delaminated after a few hours of soaking the bilayer in DI water, which indicated unstable bonding. This result suggests that the bonds formed using TMSPMA can be cleaved by water and eventually lead to unstable adhesion between the two layers.

2.3.2 Fabrication of PDMS/Hydrogel bilayer using benzophenone

PDMS layers less than 120 μm were fragile and difficult to handle without tearing. To ensure both the flexibility and durability for future use as a retinal electrode array, PDMS

thickness was set to 300+/− 50 μm [100]. The fabrication scheme is shown in **Figure 7 a**. First, the PNIPAAm solution was spin-coated on glass slides as a sacrificial layer, based on PNIPAAm's dissolution in water lower than 32 °C. Then, the PDMS prepolymer mixture was spin-coated on top of the PNIPAAm-coated glass slides and cured. The thickness of PDMS decreased as the spin speed and spin time increased. We noted that a spin speed at 250 rpm for 30 s could produce a PDMS layer with a thickness around 300 μm. After curing, the PDMS was cut by laser into rectangular strips (17 mm × 2.5 mm (length × width)). Next, surface modification was done by immersing the slide into the benzophenone solution for 4 min, followed by washing three times with methanol and drying with air. Hydrogel pre-solution of varying monomer concentrations was poured into a Teflon mold, and surface-modified PDMS attached to the glass slide was flipped onto the mold. After curing with the UV irradiation for 5 min, the glass slides were immersed into DI water to release the bilayer strips quickly. Released bilayer strips curved in water instantly (**Figure 7 b**).

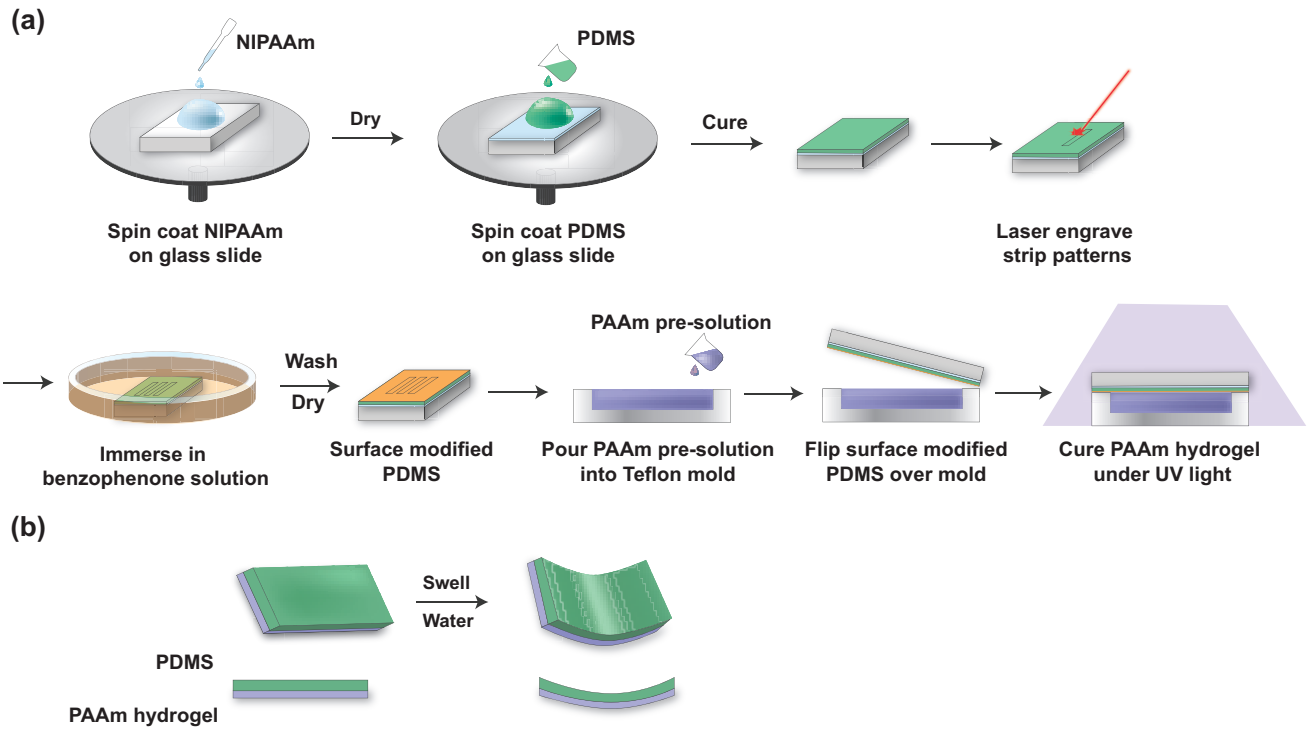

Figure 7 Schematic illustration of fabrication of the bilayer and the swelling process. (a) Schematic illustration of the fabrication of the hydrogel/elastomer bilayer. (b) Mechanism of the shape transformation of the bilayer strip. Images not to scale.

2.3.3 Initial monomer concentration is proportional to final bilayer curvature

To explore how the intrinsic properties of hydrogel affect the bilayer curvature, we first investigated the intrinsic properties of PAAm hydrogel with different initial monomer concentrations. Prior work has shown that a higher initial monomer concentration led to a decreased swelling ratio and a higher modulus of hydrogel [130], [136], [137], shown in **Figure 8 a**, we found that with a high initial monomer concentration, the PAAm hydrogel had (1) a decreased expansion strain, (2) an increased Young's modulus when hydrated, and (3) an increased thickness when fully dried. Preparing hydrogel in a dilute pre-gel solution with low monomer concentration leads to ineffective usage of cross-linkers and a reduced cross-link density. At the same time, the resulting polymer concentration of the formed gel also decreased,

which led to a decreased thickness in the dried hydrogel. While the elastic modulus is related to the effective cross-link density, the modulus was expected to reduce with a low initial monomer concentration. Meanwhile, the reduced polymer concentration allows the PAAm gel to disentangle more easily during hydration, effectively increasing the swelling ability [130], [138]. Notably, the highest modulus of PAAm hydrogel (20 wt% initial monomer concentration) was 217.86 kPa, which remained lower than that of PDMS (562.40 kPa). Therefore, hydrogel was softer and presumably more tissue compatible than PDMS.

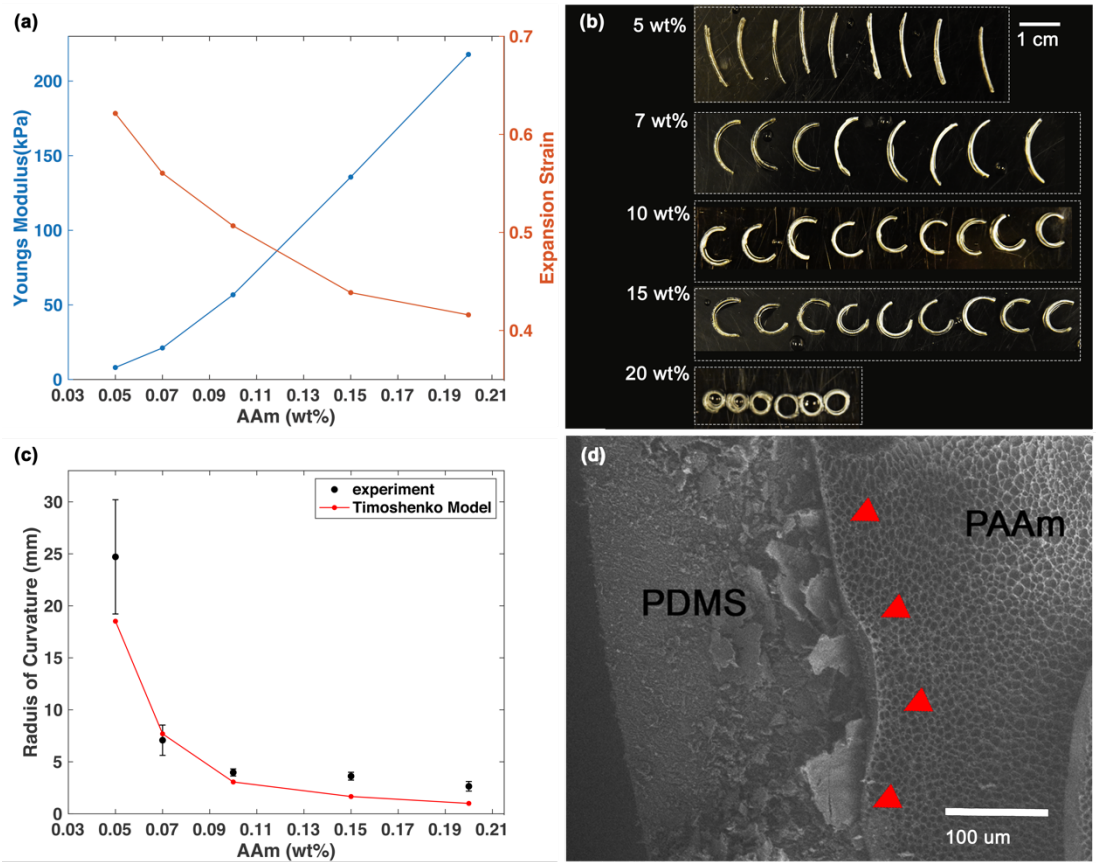

Figure 8 Characterizations of hydrogels and curvature measurement of bilayer strips. (a) Young's modulus and expansion strain of hydrated hydrogels with different AAm initial concentrations. (b) Hydrated bilayer strips (17 mm × 2.5 mm (length × width)) with different AAm wt%. Images were captured with samples on a dry surface to allow consistent arrangement of the samples, but the dry environment slightly affected the curvature. The images used for curvature analysis were taken with the samples in deionized (DI) water. The scale bar is 1 cm. (c) The radius of curvature of bilayer strips with different initial monomer concentrations. The black dots represent experimental data. The sample size is six for bilayer with 20 wt% AAm and nine for other concentrations. The error bar represents standard deviation. The red line represents simulation results from Timoshenko model. (d) SEM image of the bilayer interface (red arrows) with 10% wt% AAm initial monomer concentration. This sample underwent swelling, then freeze-drying. The scale bar is 100 μm. The contrast was enhanced (Adobe Photoshop).

When constrained by a non-swelling passive layer, the responsive layer of the hydrogel can only swell asymmetrically. The tensile stress on PDMS and the compressive stress on PAAm hydrogel induced bending moments, producing a curved structure with PDMS on the concave side. We investigated the curvature of bilayer strips with five different initial monomer AAm concentrations: 5, 7, 10, 15, 20 wt%. At the same time, we kept constant the molding conditions, cross-linker ratio (the weight ratio of MBAM to AAm), and the initiator ratio (the weight ratio of Irgacure 1173 to AAm). We noted that with high initial monomer concentration, the curvature of the bilayer increased (**Figure 8 b and c**). Because the radius of curvature is the reciprocal of the curvature, the radius of curvature decreased with a higher monomer concentration.

The bimetallic strip model developed by Timoshenko [139] and its derivatives are widely used to explain the mechanical behaviors of the hydrogel bilayer strip [95], [128], [140]:

$$\frac{1}{\rho} = \frac{6 \times \varepsilon_{PAAm} \times (1+m)^2}{h(3(1+m)^2 + (1+mn)(m^2 + \frac{1}{mn}))} \quad 1)$$

where ρ is the radius of curvature at a given time, ε_{PAAm} is the expansion strain of PAAm hydrogel, $\varepsilon_{PAAm} = \frac{\Delta l}{l}$. Here, Δl is the difference of dimensions of hydrogel between dried state and hydrated state, and l is the dimensions of the hydrogel in the dried state. $m = \frac{h_{PDMS}}{h_{PAAm}}$ is the thickness ratio between the two layers. h is the total thickness of the bilayer. $n = \frac{E_{PDMS}}{E_{PAAm}}$ is the ratio of Young's modulus of two layers.

The radius of curvature is related to the expansion strain, the Young's modulus, and the thickness ratio of the bilayer, as shown in Equation (1) [139]. Changing the monomer concentration will change all of these parameters in ways that will have opposing effects on the radius of the curvature. The decreased expansion strain of the hydrogel layer leads to a decrease in the curvature, while the increased Young's modulus and thickness of the hydrogel leads to a

larger curvature. Shown in **Figure 8 c**, we used Equation (1) as the model and input the mechanical data and thicknesses of the two layers. The predicted and experimental curvature follow a similar trend.

The SEM image (**Figure 8 d**) of the freeze-dried sample shows a robust interface between PAAm hydrogel and PDMS. The monomers together with cross-linkers formed a network of porous PAAm hydrogel, similar to previously reported work [120], [141] The relationship between the initial monomer concentration and the transformed curvature can help us to design the bilayer formula to achieve a desired curvature.

2.3.4 PAAm/PDMS bilayer can be retinal array substrate

We further investigated the potential of the bilayer to be used as the substrate for a wide-field epiretinal prosthesis. Given the importance of peripheral vision with respect to mobility [33], [142], our design will provide visual perception over 100° of the visual field. We fabricated a six-petal flower-shaped bilayer with a diameter of 34 mm by means of the same technique shown in **Figure 9 a**. If we assume that a human eye is a perfect sphere with a radius of curvature of 11.5 mm and 1° of visual field is equal to 300 μm on the retina [49], [143], the Argus II electrode array (6.19 mm diagonally) requires a 31° bending and can restore approximately 21° of visual field, while our bilayer with a diameter of 34 mm requires a 169° bending and can restore 113° of visual field. From **Figure 9**, we demonstrated that PDMS without hydrogel had negligible curvature, while the bilayer flower had a curved shape because of the swelling of the PAAm hydrogel. Based on PDMS and PAAm hydrogel thickness, the bilayer with a 34 mm diameter can be rolled into a spiral tube with a theoretical diameter of 1.58 mm. The bilayer can be fixed by drying and would expand once implanted. Argus II requires a

surgery with a 5-mm incision in the eye wall to insert the retinal electrode array [59]. Our rolled bilayer will easily pass through a 5 mm incision and may allow the incision size to be reduced.

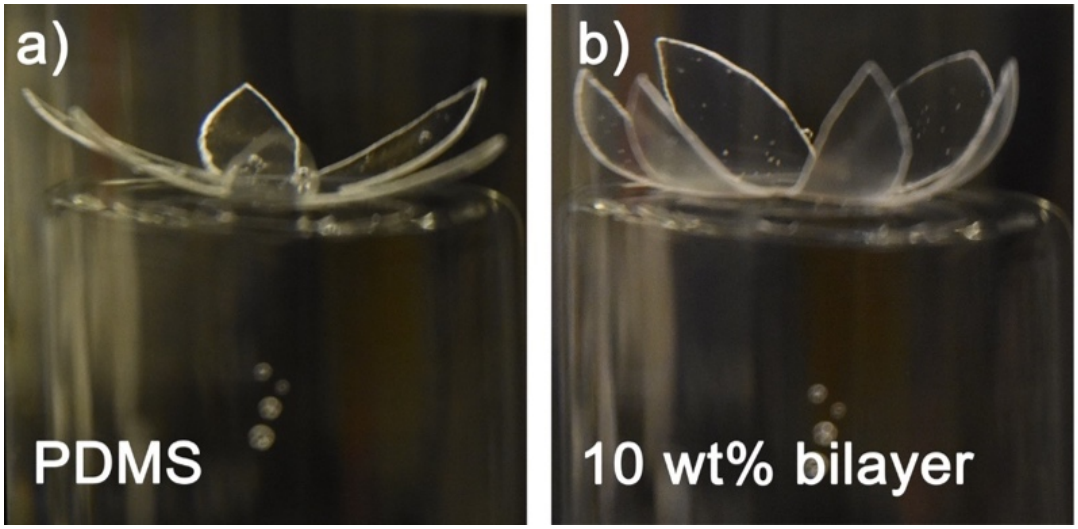

Figure 9 Photo of swollen bilayer flower in water. (a) Polydimethylsiloxane (PDMS) without polyacrylamide (PAAm) layer. (b) Bilayer samples with 10 wt% initial monomer concentration. All samples in DI water. The flower shape is designed to unfold after implantation in the eye. This structure shown would cover 34 mm on the retina, equivalent to a visual field of about 113° [49].

2.4 Discussion

In this study, we demonstrated the design of a robust hydrogel/elastomer bilayer system that can transform from 2D to 3D after immersion in water. Preliminary results showed that TMSPMA as the bonding agent grafted on a roughed surface resulted in poor adhesion between the two layers of PDMS and hydrogel after staying in water for hours. However, for epiretinal application, the bonding between the PDMS/PAAm bilayer needs to stay robust in an aqueous environment for as long as possible. Benzophenone was eventually proved feasible and robust as the bonding agent instead of TMSPMA. Spin-coating and molding fabrication methods are used to achieve reproducible thickness control and bending behaviors. We investigated the effect of the initial monomer concentration of hydrogel pre-solution on the curvature of the transformed shape. The expansion strain, Young's modulus, and the thickness ratio between the two layers all

contributed to the final curvature. A higher monomer concentration in the pre-solution produced a larger curvature and a smaller radius of curvature. While the expansion strain of hydrogel decreased as the monomer concentration increased, the enlarged modulus and thickness of the hydrogel had a dominant effect and consequently produced a larger bending motion. Swelling was performed in DI water. The aqueous environment in the eye after vitrectomy is similar to saline (NaCl) [59]. NaCl does affect the swelling properties of PAAm hydrogel, but to a relatively small degree at the physiological concentration [144]. As we get closer to in-vivo testing, we will recalibrate the bilayer curvature in physiological saline. Timoshenko's model provides a theoretical basis for the effect of varying initial monomer concentration on the bilayer curvature. The effect of the aspect ratio and thickness ratio on the transformed curvature have also been reported [128], [129]. Although those factors could all effectively tune the curvature, our application of a retinal prosthesis required a relatively thin layer of PDMS and a fixed-shape design. Therefore, varying initial monomer concentration is more feasible and practical to precisely adjust the transformed curvature.

With the understanding of how the intrinsic mechanical properties of hydrogel affect the final shape, we were able to rationally design the hydrogel formula to make a 3D shape with the desired curvature (**Figure 9**). **Figure 10** illustrates a concept for incorporating these design features into a wide-field epiretinal prosthesis. In our proposed design, the epiretinal prosthesis uses PDMS for the multielectrode array substrate and insulation layers. Conducting lines will be gold (Au), with additional adhesion layers as needed—for example, chromium (Cr). Our electrode array design is expected to have 100 electrodes in the central area with a diameter of 200 μm and up to four electrodes on each peripheral petal [145]. To enable chronic stimulation, electrodes can be electrodeposited platinum [146] or platinum–iridium [147]. To facilitate

pattern stimulation, electrodes are denser and smaller in the central area. Peripheral electrodes are more sparse and larger, since their role is to alert the user to objects in the periphery. Even though the petals of the proposed array will not cover the entire peripheral retina, the accompanying camera and video processing system can be programmed to map continuous regions of the peripheral camera field-of-view to each of the petals. Central electrodes will have a lower allowable stimulus charge due to their small size [1]. Thus, the central electrodes must be close to the retina for low perceptual thresholds [148], and hydrogel will not be on the central part of the array, since the hydrogel layer separates the electrodes from the retina. A hydrogel layer outside the central region will ensure the curvature of the array, which will also help the central electrodes be in close retinal contact. The hydrated hydrogel in DI water has a comparable conductivity to DI water [149]; therefore, the large peripheral electrodes can still pass stimulus currents through the hydrogel into the retina. Although separating the peripheral electrodes from the retina will increase the perceptual threshold, large peripheral electrodes will safely pass more currents to overcome this issue. This bilayer system can be used in other neural or biological interfaces requiring a 3D anatomical interface and soft materials as well.

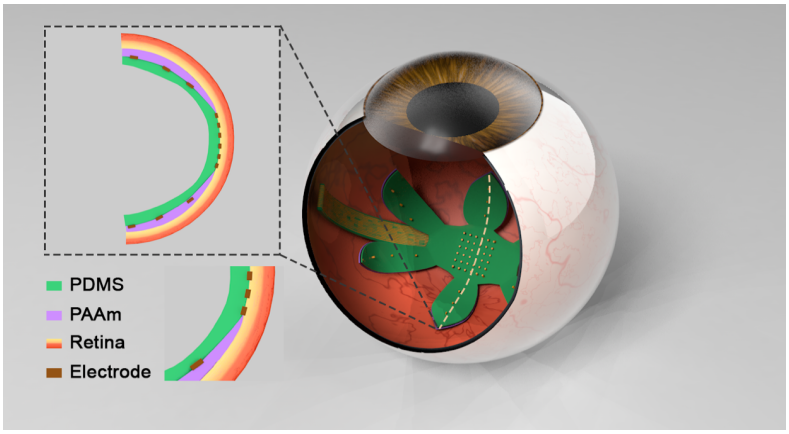

Figure 10 Conceptual illustration of the wide-field bilayer array implanted in the eye. Inserted picture demonstrates the cross-section of the interface between the array and the retina.

Other approaches to wide-field array have been demonstrated, including foldable arrays made of polyimide [74], parylene C [77], PDMS [78], and shape-memory polymers (SMP) [30]. Most wide-field arrays utilized the elasticity of the substrate or manipulation by the surgeon for the unfolding of the array. The SMP bilayer wide-field array is similar to our work and the two approaches share the advantage of unfolding to a pre-determined curvature. However, the unfurling time of the SMP bilayer was less than one minute. This unfolding can be sudden and unpredictable, which may lead to unintended contact with the retina. In contrast, a hydrogel bilayer approach allows slow, controlled unfolding as the functional polymer layer changes shape. Furthermore, the SMP bilayer array used polyimide as the electrode array substrate, which is significantly stiffer than PDMS and hydrogel. The hydrogel-coated array has a significantly lower modulus to better conform to the curvature of the retina. Since curvature mismatch will result in pressure on the retina, the hydrogel/elastomer wide-field array will be less damaging to the retina in this scenario.

In the follow-up work, we will use the PAAm/PDMS bilayer as the substrate and will deposit metal electrodes onto it. Prior works have shown the possibility of fabricating electrodes on PDMS [100], [150], [151]. Initial fabrication based on the procedure in [150] provided successful deposition of a Cr/Au/Cr metal layer on PDMS (**Figure 11**). Importantly, stretching the metal lines was plausible owing to the micro-wrinkles in the metal film. Flexible and stretchable metal leads are necessary when making an electrode array that has a small form factor for minimally invasive implantation followed by unfolding in the vitreous body after implantation. A prior study further demonstrated that a thin layer of metal on PDMS had an improved stretchability [103], due to micro-cracks in the layer. It was proposed that the micro-cracked layer formed a network that maintained electrical continuity under stretching. We will

further systematically investigate the metal electrode deposition and the feasible extent of folding in due course.

Figure 11 Cr/Au/Cr metal layer deposited on PDMS. Conductive tracks were designed to be 100 μm in width and the circular electrode to be 200 μm in diameter.

5. Conclusion

We demonstrated a hydrogel-PDMS bilayer structure that curves in a predictable manner when immersed in water. Initial monomer concentration was directly related to the resulting curvature. Our planned application of this technology is a wide-field retinal prosthesis, but this bilayer technology has applicability to other neural interface or biosensor systems that require a compliant 3D interface.

Chapter 3 Fabrication of Polydimethylsiloxane (PDMS)/polyimide (PI)/PDMS Based Electrode Array for Full-field Epiretinal Prosthesis

3.1 Abstract

Most clinically and commercially available electrode arrays are made from rigid materials, which have a mechanical mismatch and non-conformability with organic neural tissues. Flexible and soft devices can prevent damage to fragile tissues. However, the fabrication of electrodes and metal traces on mechanically compliant substrates such as PDMS remains a challenging process to implement reliably. However, PDMS is considered biocompatible in a wide array of applications, and the surface of PDMS can be modified relatively easily, which makes it an ideal material to interface with the hydrogel layer (as shown in Chapter 2). The goal of this study is to fabricate a flexible electrode array with electrode sites and a layer of PDMS on the same side of the array. This will allow us to use hydrogel/PDMS bilayer to curve the array and will position the electrode sites in the right location to stimulate the retina. We experimented with two different methods to fabricate functional electrode arrays on flexible substrates. Using parylene C coated PDMS as the substrate resulted in a low yield of functional electrodes and cracks on both parylene C and PDMS. Wet etching as the method to open electrode sites on PDMS was uncontrollable and led to undesirable openings across the array. Eventually, we adopted a PDMS/polyimide-based electrode array/PDMS sandwich as the foundation of the multilayered electrode array. Polyimide functioned as the substrate and insulation layer for electrodes. The top layer of PDMS, with manually opened electrode sites, functioned as the interface with the hydrogel layer, while the bottom layer of PDMS provided further mechanical

support. This sandwich electrode array has a high yield of functional electrodes and is flexible, demonstrating the potential to be integrated with hydrogel to form a compactable and full-field epiretinal prosthesis.

3.2 Introduction

Retinitis pigmentosa progressively causes peripheral and central vision loss, and results in blindness in patients [152]. While central vision is essential for daily activities, the loss of peripheral vision can also greatly impair the mobility of patients [153]. Epiretinal prosthesis showed the feasibility of restoring vision to some extent [48]. However, the majority of epiretinal prostheses covers a small area of the retina. Argus II electrode array covers a 5x3 mm^2 area of retina and thus only provides limited stimulation of the central macula [70]. A significant limitation of the size of the state-of-art epiretinal arrays is the requirement of the minimal scleral incision. Also, most retinal arrays are fabricated using rigid materials and cannot form a conformal interface to the retina. Novel electrode arrays incorporating new materials are needed to meet the demands imposed by implantation (small array for insertion through an eyewall incision) and function (large array to stimulate both central and peripheral retina).

In general, there are two aspects to consider when developing a wide-field epiretinal array: the flexibility and foldability of the material to minimize sclerotomy, and the conformability of the electrode array to the curvature of the retina to minimize compression on the retina while keeping the stimulating electrodes close to the retina over a wide area of retina. Although research groups have proposed and developed wide-field epiretinal prostheses, they are typically made from less flexible materials such as polyimide, and the folding process of the electrode array is uncontrollable [75], [77], [78], [154].

The incorporation of soft materials such as PDMS as the main structural component can potentially improve the next generation of the wide-field prosthesis. PDMS has good biocompatibility [101] and has a low Young's modulus compared with other materials used in neural interface fabrication [155]. There are multiple examples of using PDMS in flexible neural interfaces [24], [105]. PDMS in combinations with other materials such as parylene C and polyimide have been explored as well [156], [157], [110].

Nevertheless, fabrication using microelectrode arrays procedures on soft materials such as PDMS is difficult. PDMS tends to swell with certain organic solvents [158], and has a higher thermal expansion coefficient than other common materials used in fabrication [159]. In this chapter, we will discuss our attempts to deposit and pattern metals on PDMS with a parylene C intermediate layer, which resulted in unstable electrical connections and poor reproductivity. We eventually abandoned this approach, but we include the information in this dissertation to benefit others who may work on PDMS-based arrays in the future. The alternative approach was using a polyimide/PDMS hybrid. Polyimide has been used for neural electrodes for decades and is the material used for the retinal array in the Argus II retinal prosthesis. In our hybrid, polyimide is used for the electrical signal routing and electrodes, while PDMS is the mechanical substrate and hydrogel interface. With this approach, we can keep the flexibility of the substrate, by minimizing the polyimide thickness and width, and fabricate reliable electrode arrays using established methods for polyimide microfabrication. In this chapter, we describe the fabrication steps. In Chapter 4, we describe hydrogel coating and evaluation of the full-field array (FFA).

3.3 Materials and methods

The responsive epiretinal prosthesis needs to bond with a hydrogel layer to configure into a 3D curvature. Therefore, the fabrication protocol of the electrode array must result in a PDMS

encapsulation layer and exposed electrodes on the same side of the array. This is required since hydrogel, which will attach to PDMS, will impart curvature such that the hydrogel and electrode openings will face the retina.

To meet the requirement that PDMS layer and electrode openings are on the same side, we first attempted to pattern metals on PDMS/parylene C hybrid substrate and to micro-machine the openings on the encapsulated PDMS layer. We have found different failure modes during the processes, including cracks on the surface and unconnected electrodes, unopened electrodes, and residual encapsulations on the openings.

To prevent the failures, we fabricated electrodes and conductive tracks on polyimide instead, and sandwiched the polyimide-based electrode array between two layers of PDMS. By establishing this protocol, we were able to have a high yield of functional electrodes.

All the above-mentioned fabrication methods will be described in detail as follows.

3.3.1 Fabricate electrodes on parylene C coated PDMS

Our fabrication involved patterning metal layers on PDMS/parylene C hybrid, and then patterning another layer of PDMS on top as the encapsulation layer. Parylene C was introduced as an intermediate layer on PDMS to facilitate the photolithography process [150]. We also used a thick photoresist dry film to micro-pattern the second layer of PDMS to open electrodes and conductive pads [160]. Stepwise processes are outlined in **Figure 12-14**.

Figure 12 shows the preparation of PDMS/Parylene C substrate. First, a parylene C releasing layer was deposited on the clean borosilicate glass wafer in a parylene C coater (SCS PDS 2035CR, Specialty Coating Systems, Indianapolis, IN, USA). The parylene C layer was treated with oxygen plasma for 1.5 minutes to promote adhesion on the surface(PlasmaTherm 790 RIE, Plasma-Therm LLC, Saint Petersburg, FL, USA). Then, PDMS (PDMS, Dow Corning

Sylgard 184 Silicone Elastomer Kit, Dow Corning, Midland, MI, USA) prepolymer and curing agent were weighed at a ratio of 10:1 and mixed well for 2 mins. Degassing under a vacuum desiccator helped to eliminate the air in the mixture. Degassed PDMS was poured on the parylene C coated glass wafer and spin coated at 200 rpm for 30 s to form a layer of PDMS around 239 um thick. Then the wafer was put on a hotplate at 50 °C overnight. Cured PDMS was coated with another layer of parylene C as an intermediate layer. A positive photoresist (Megaposit SPR 220, DuPont, Wilmington, DE, USA) was spin coated and developed as a mask. Then, the exposed parylene C was etched by oxygen plasma (PlasmaTherm 790 RIE, Plasma-Therm LLC, Saint Petersburg, FL, USA). The underneath PDMS was treated with argon plasma and showed a micro-wrinkled surface. After that, a Cr/Au layer of thickness 10 nm/100 nm was deposited (Enerjet Evaporator) on the wafer. The photoresist was lifted off and the patterned metal layers demonstrated a micro-wrinkled surface because of the micro-wrinkles on the PDMS substrate.

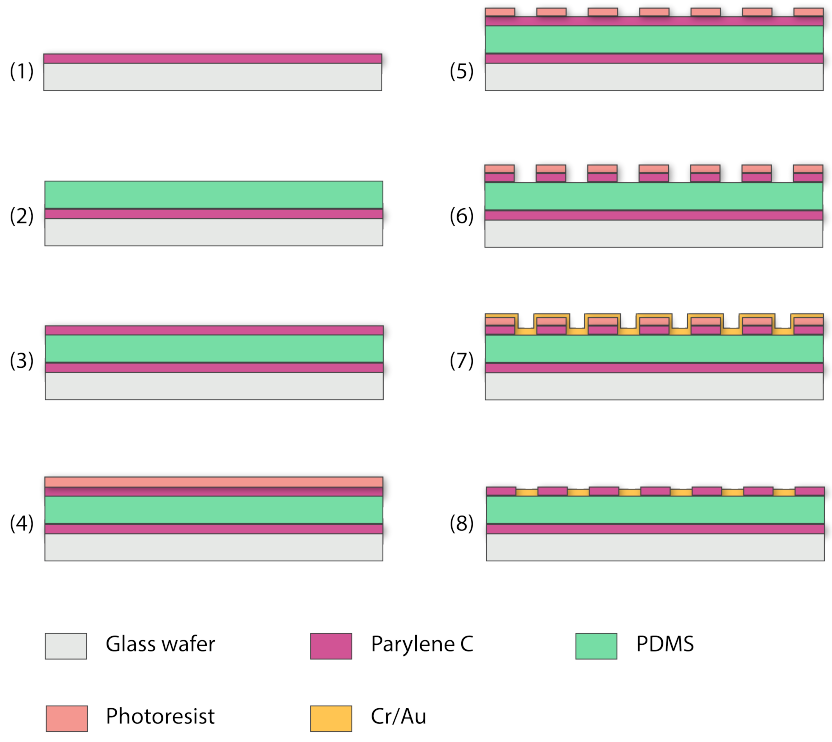

Figure 12 Scheme of stepwise fabrication of patterning electrodes and conductive tracks on PDMS/Payrlene C hybrid.The fabrication involved the deposition of parylene C on top of spin-coated PDMS, then followed by the patterning of parylene C.

Figure 13-14 showed the process of micro-pattern a thin layer of PDMS on top as the insulation layer. The micro-patterning was approached with two different methods. **Figure 13** shows the first method of using a thick photoresist dry film as sacrificial posts. First, a layer of dry film (Riston LDI 7299, DuPont, Wilmington, DE, USA) of thickness around 100 um was annealed. Then the dry film was patterned and developed in 1 wt% K_2CO_3 solution. The formed photoresist pillars aligned with the opening sites of the electrodes and conductive pads. A thin layer of PDMS of around 20 um thick was spin coated. Because of the difference in the heights of the dry film pillars and the thin layer of PDMS, the PDMS, which covers the pillars and where the electrode and conductive pad openings were, was removed after lifting off the photoreist pillars in a 3 wt% KOH solution. Before conducting the lifting off, oxygen plasma can be used to etch the PDMS on the sidewalls of the pillars to further facilitate the removal of the PDMS.

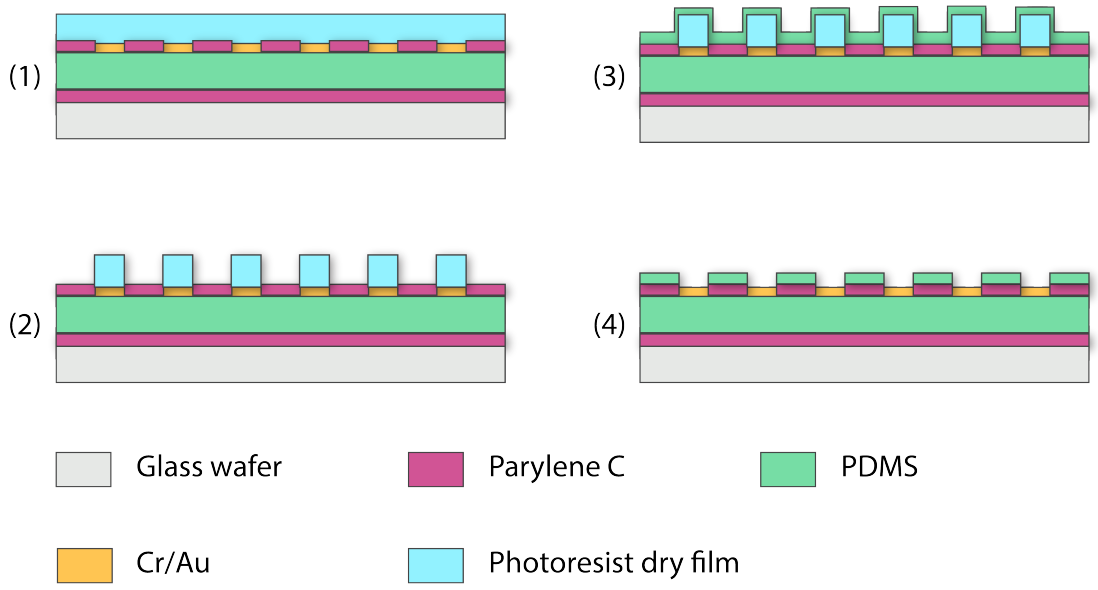

Figure 13 Scheme of micro-patterning the second layer of PDMS using a thick dry film as the sacrificial posts. A sacrificial photoresist dry film was laminated on parylene C-coated PDMS, then the dry film was patterned by photolithography. Because of the height difference of the dry film pillars and later spin-coated PDMS, the top layer of PDMS was patterned by lifting off the dry film.

Figure 14 shows the second micro-patterning method using wet etching. First, PDMS was spin coated on top with a thickness of 20 um. Following argon plasma, a Ti/Al layer of 5 nm/1000 nm was sputter deposited (Closed Frame PRO Line Sputter System, Kurt J. Lesker Company, Jefferson Hills, PA, USA) on PDMS. A photoresist was later spin coated and patterned, and the exposed Ti/Al layer was etched. Afterward, the exposed PDMS was wet etched at room temperature in a solution of 1-Methyl-2-pyrrolidinone (NMP; Sigma-Aldrich 443778; ≥99%) and tetra-butyl ammonium fluoride (TBAF 75 wt% in H2O, Sigma-Aldrich 361399). The volume ratio of NMP to TBAF/water was 3:1 [161]. Finally, the Ti/Al hard mask was etched.

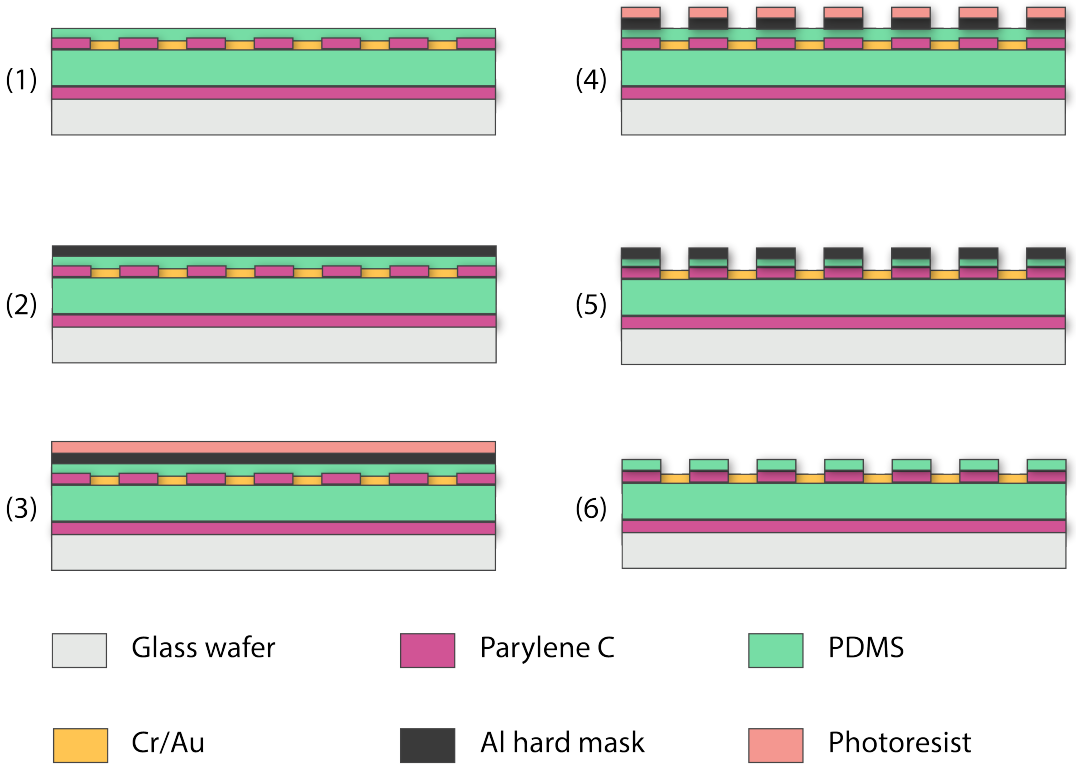

Figure 14 Scheme of micro-patterning the second layer of PDMS by wet etching. An aluminum-based hard mask was deposited and patterned on parylene C-coated PDMS. Then, wet etching removed the exposed PDMS defined by the hard mask. Finally, the hard mask was removed.

Both microscopic images and SEM (TESCAN RISE, TESCAN, Brno, Czech Republic) images were used to visualize the surface of the electrodes.

3.3.2 Electrical charaterization

Electrochemical impedance spectroscopy (EIS) was performed on one device using the wet etching method. The conductive pads were covered by carbon ink (PELCO conductive carbon glue, Ted Pella) and cured at room temperature. Before curing, a crimp socket soldered with wires was placed on carbon ink to provide electrical connection to the electrodes.

EIS was collected using Gamry 600+ potentiostat (Gamry Inc., Warminster, PA, United States). EIS was performed at a frequency range of 10 Hz–1 MHz, and in a solution of 0.01 M PBS (phosphate buffered saline) with a three-electrode set-up.

3.3.3 Fabrication process for polyimide-based electrode array

Our fabrication process involves polyimide as the direct substrate and insulation for electrodes and conductive tracks, and the polyimide-based electrode array was later sandwiched between two layers of PDMS. Polyimide is compatible with microelectromechanical systems procedures and could provide reliable electrical connections. Flexibility was achieved by making the thickness and width of the polyimide structure small. The steps of the fabrication are shown in **Figure 15** and are described as follows.

As shown in **Figure 15**, polyimide (PI 2611, Hitachi DuPont MicroSystems, Parlin, NJ, USA) was spin coated at 4000 rpm for 60 seconds on a Si wafer with 2 um of SiO_2. PI was soft baked at 90 °C for 10 minutes and then at 115 °C for 10 minutes on a hotplate. The partial cure of PI was done in a vacuum oven (YES PB8-2B-CP Vacuum Oven, Yield Engineering Systems,

Inc., Fremont, CA, USA). Then, a photoresist (Megaposit SPR 220, DuPont, Wilmington, DE, USA) was spin coated, patterned, and developed as a mask for the following metal layers. The wafer was cleaned with oxygen plasma (YES-CV200RFS, Yield Engineering Systems, Inc., Fremont, CA, USA). A Cr/Au/Cr layer of thickness 20 nm/200 nm/20 nm was deposited. Afterward, electrodes and conductive tracks were patterned by lifting off the photoresist in acetone. Then, the second layer of PI was spin coated and fully cured in the vacuum oven. An Aluminum mask was patterned on the second layer of PI, and the exposed PI was completely etched by oxygen plasma (PlasmaTherm 790 RIE, Plasma-Therm LLC, Saint Petersburg, FL, USA). Finally, the PI-based device was lifted after soaking in deionized water overnight.

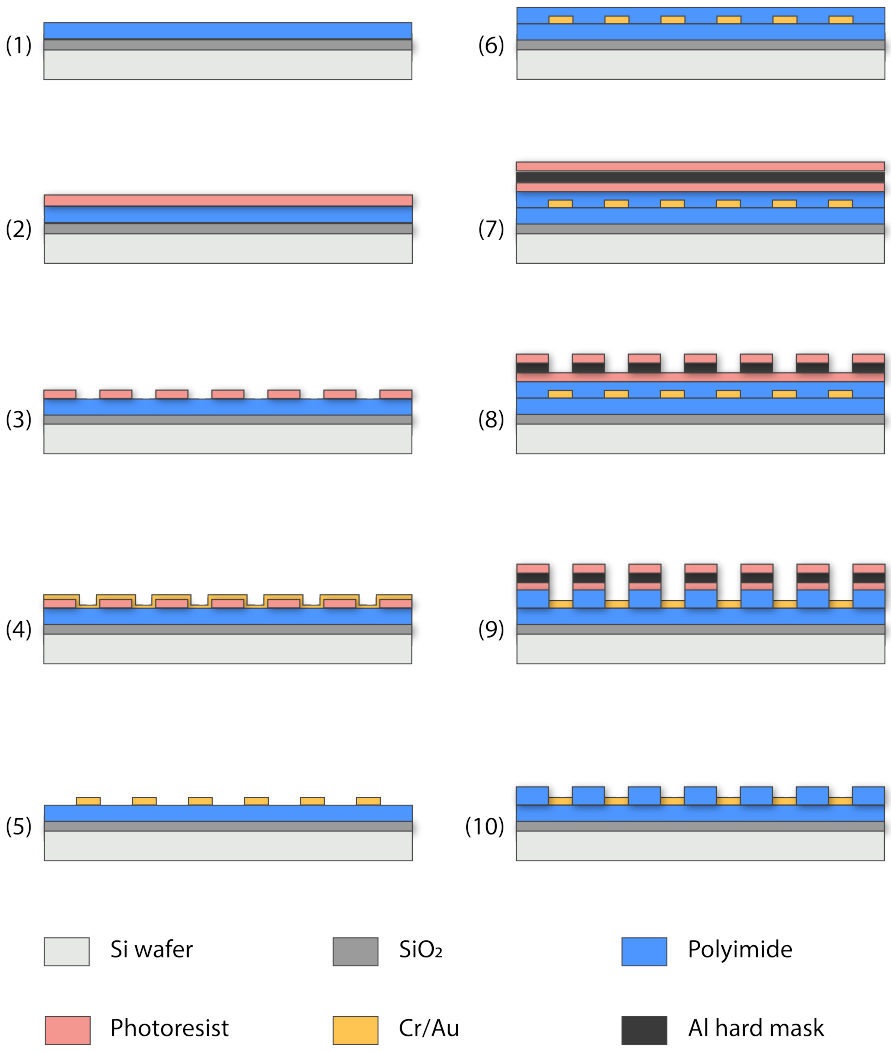

Figure 15 Schematic illustration of sequential fabrication processes for polyimide-based electrode array. The bottom layer of polyimide was spin coated on the wafer and partially cured. Then, metal electrodes and conductive lines were patterned on polyimide by photolithography. Finally, the top of layer of polyimide was spin coated on top and patterned with electrode sites open.

3.3.4 Sandwich Polyimide electrode array between PDMS and build the connectors

The PI-based device was sandwiched by two layers of PDMS. The bottom layer of PDMS was around 230 um thick and functions as the mechanical support. The top layer of PDMS was around 20 um thick with openings for the electrodes, and this layer will be the interface to bond with a hydrogel layer.

Figure 16 a demonstrated that the bottom layer of PDMS was spin coated on the releasing agent (Sigmacote, Sigma-Aldrich) treated glass wafer.

Figure 16 b showed a manual approach to remove PDMS on the electrode and conductive pad openings. In this method, a photoresist layer was spin coated and patterned at the back of the glass wafer as alignment guidance. Then, a punchcutter was used to mark the area of removal on PDMS, and a razor blade was used to remove the PDMS for complete exposure of the openings.

Afterward, as demonstrated in **Figure 16 c**, both layers of PDMS were activated with oxygen plasma (PE series, Plasma Etch Inc., Carson City, NV, USA) at 50 W for 1 minute. Then, the two layers were carefully aligned and laminated for full contact. The laminated two wafers were baked in an oven at 70 °C for 10 minutes to promote the bonding between the two layers. Finally, the top layer of PDMS was released from the wafer by soaking the laminated layers in acetone. Following the laser ablation to cut the outlines of the device, the sandwiched electrode array was peeled off from the bottom wafer.

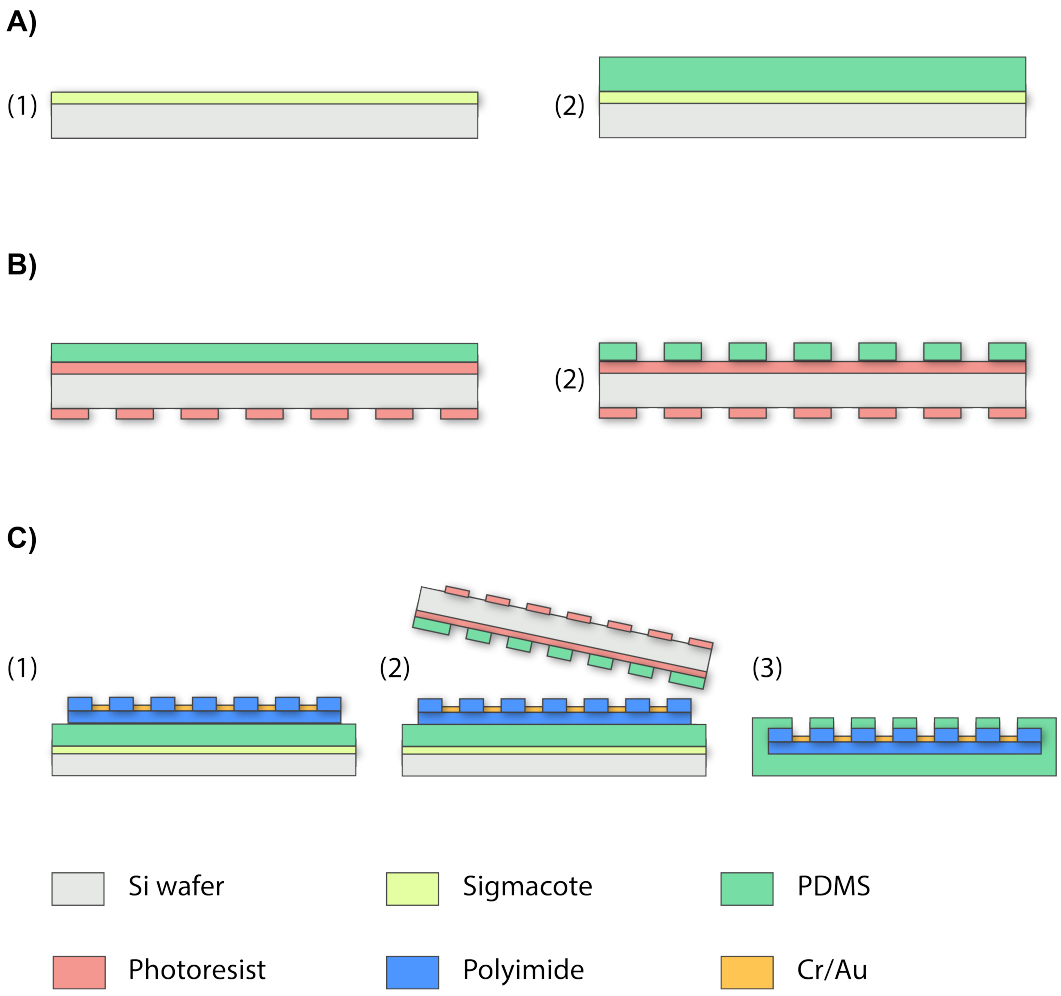

Figure 16 Illustration of procedures to build sandwiched electrode array. (a) Fabrication of the bottom layer of PDMS; (b) Farbication of the top layer of PDMS with the guidance of back alignment marks; (c) Sandwiching polyimide-based electrode array between two layers of PDMS.

3.4 Results and discussion

3.4.1 Fabrication on PDMS/ parylene C hybrid

Our PDMS/parylene C hybrid based electrode array faced challenges during the fabrication. The main challenges are discussed below.

A. Parylene C as the releasing layer

The releasing layer between the glass wafer and spin coated PDMS facilitates the easy release of the device after the finish. Parylene C has a low interface adhesion force with PDMS, which makes it a potential releasing material [162]. On the other hand, the releasing layer needs to maintain a stable adhesion with PDMS throughout stepwise fabrication processes till the end.

Initially, we used physical vapor deposited parylene C without any surface treatments as the releasing layer, and we observed bubbles generated between PDMS and parylene C layer during subsequent processes (**Figure 17 a**). We explored methods to increase the adhesion force, and various surface modifications, including oxygen plasma were known to activate the inert surface of parylene C [163]. Therefore, we treated parylene C with oxygen plasma to promote surface adhesion before we spin coated PDMS. Adding this surface treatment result in less unexpected delamination between PDMS and releasing layer was found. The electrode array was still able to be released after the finish.

B. Parylene C as the intermediate layer

Other than the surface energy, many other factors, including the deposition method, can affect the interface adhesion force between the two layers of parylene C and PDMS [162]. PDMS has a porous structure allowing the diffusion of other materials. During the physical vapor deposition, an adhesion promoter was first deposited on the porous surface of PDMS, then parylene C was filled into the porous structure of PDMS[150]. We eventually had a strong bonding between PDMS and the intermediate layer parylene C, but this bonding depends on parylene C deposition onto PDMS.

Parylene C acts as an intermediate layer to facilitate the deposition of the photoresist and metals. Prior research has shown that parylene C could prevent cracking compared with direct fabrication on naïve PDMS, and the cracking behavior was related to the thickness of parylene C and its surface treatments [150]. After our processes described in methods 3.1.1, we observed cracking of parylene C. Cracks were found across or extending from the edge of conductive pads and electrodes (**Figure 17 b and c**). Micro-wrinkles also formed on PDMS surface, which agreed with previous studies [151], [164].

Then, we spin coated another layer of PDMS as the insulation layer. However, as mentioned in the previous results, parylene C and PDMS had low interface adhesion force. While depositing parylene C into the porous PDMS results in good adhesion, when we spin coated PDMS on top of parylene C, the adhesion between the insulation PDMS and intermediate parylene C was not robust. This challenge can possibly be further addressed by adding adhesion promoters between parylene C and PDMS.

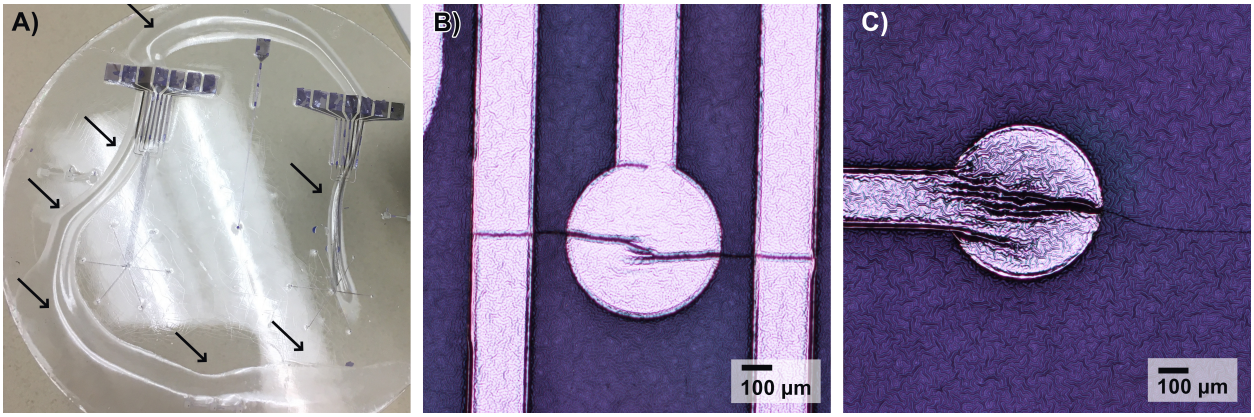

Figure 17 Challenges of patterning metal layers on PDMS/Parylene C hybrid. (a) Permanent deformation on the PDMS/parylene C hybrid was induced by the delamination between the PDMS and the releasing layer during processes. Arrows indicated the location of the deformation. (b) and (c) Cracks were found across the electrode surface, conductive track, and at the edges of the metal electrodes.

C. Insulation layer of PDMS

Approaches to micro-patterning on PDMS were reported, including dry etching [165], [166], wet etching [167], laser ablation [168], and utilization of sacrificial posts [169]. In our study, we experimented with patterning the PDMS top layer both by using a thick dry film as sacrificial posts and by using wet etching to remove PDMS.

We laminated a thick photoresist film on the parylene C and metal layer at a temperature of 110 °C (**Figure 13)**. We found that after patterning and developing the photoresist dry film, the sacrificial posts tended to maintain good adhesion to larger features but not to small features, such as an electrode with a diameter of 500 um. Consequently, not all the electrodes were reliably opened. When looking closely at the opened electrodes, the SEM image suggested residual photoresist on the surface (**Figure 18 a and b**). Using negative photoresist that can be spin coated instead of laminating dry films could possibly guarantee the improved adhesion and a higher resolution of micro-patterning on PDMS [170].

Then, we experimented with wet etching in a solution of TBAF and NPM (**Figure 14**). The rate of wet etching of PDMS was reported to change constantly throughout the process, and the final etched surface was reported to have a high roughness [161]. It was also reported that undercut could happen because of isotropic etching [165]. In our study, because of the cracks on parylene C generated from the previous steps, some of the cracks propagated to the hard mask, which induced unwanted regions exposed and eventually led to defects on the surface after wet etching (**Figure 18 c**). We also observed globular residuals of unetched PDMS on openings, especially on the small features such as electrodes (**Figure 18 d**). It was difficult to extend the etching time further because of the extensive undercut after a longer period of wet etching.

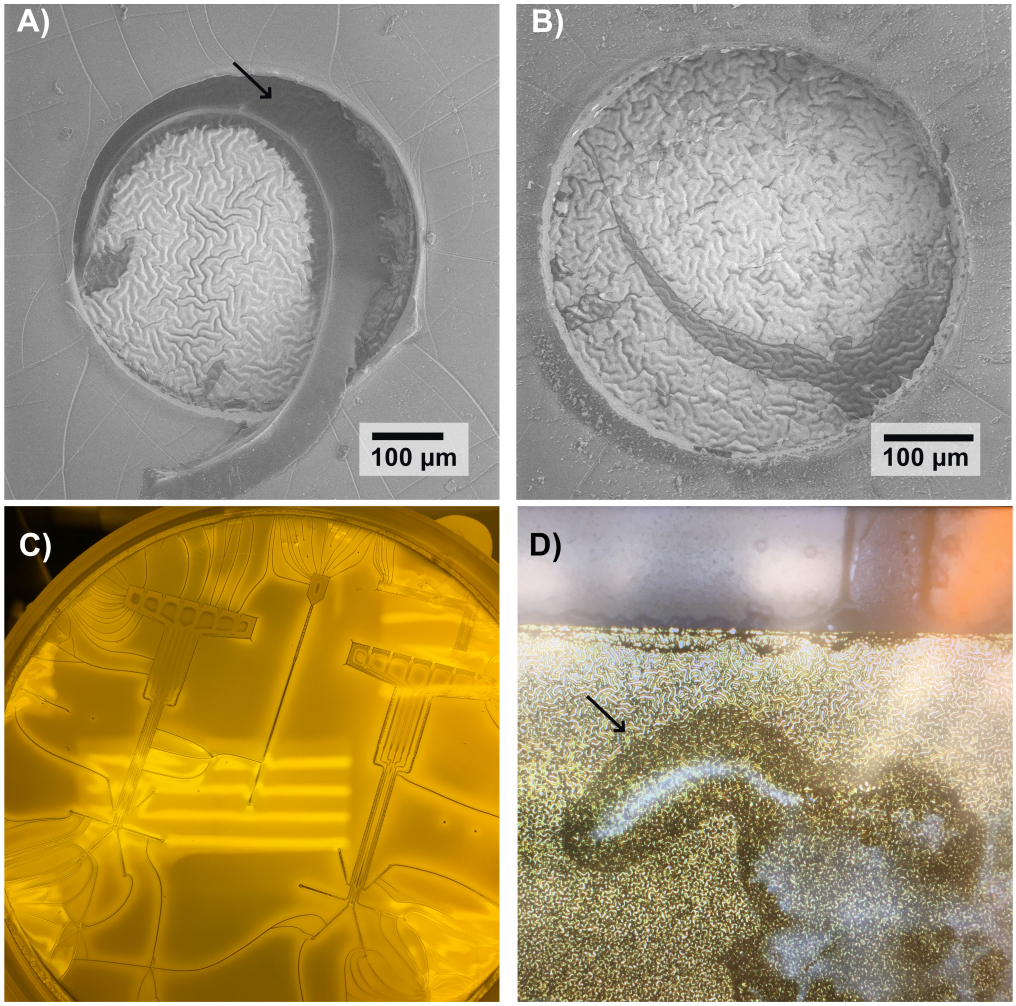

Figure 18 Challenges of micro-patterning on the second layer of PDMS. (a) and (b) different electrode surface morphology after lifting off the sacrificial posts. Arrow indicated the residual dry film, which was not lifted off successfully. Micro-cracks were also observed on the PDMS surface around the electrodes. (c) Cracked were found on the surface of the aluminum hard mask used for wet etching. (d) Arrow indicated the globular residuals of PDMS that were not etched thoroughly on a conductive pad surface.

3.4.2 EIS of PDMS-based electrode array

We characterized the 4 functional electrodes on one electrode array out of seven fabricated electrodes (**Figure 19 a**). Since all electrode sites are the same size, the impedance should be very similar between sites (for example, with a standard deviation of 5.52% of impedance at 1 kHz, data can be found in Chapter 4). The varied impedance at the high frequency indicated contamination on the electrode surface. After electroplating the electrodes with platinum and

iridium alloy (method detailed in Chapter 4), we confirmed that the contamination was from the insufficient opening of the electrode sites, and the residual PDMS still covered the majority of the area on the electrodes with only a few locations where gold was available for electroplating (**Figure 19 b and c**).

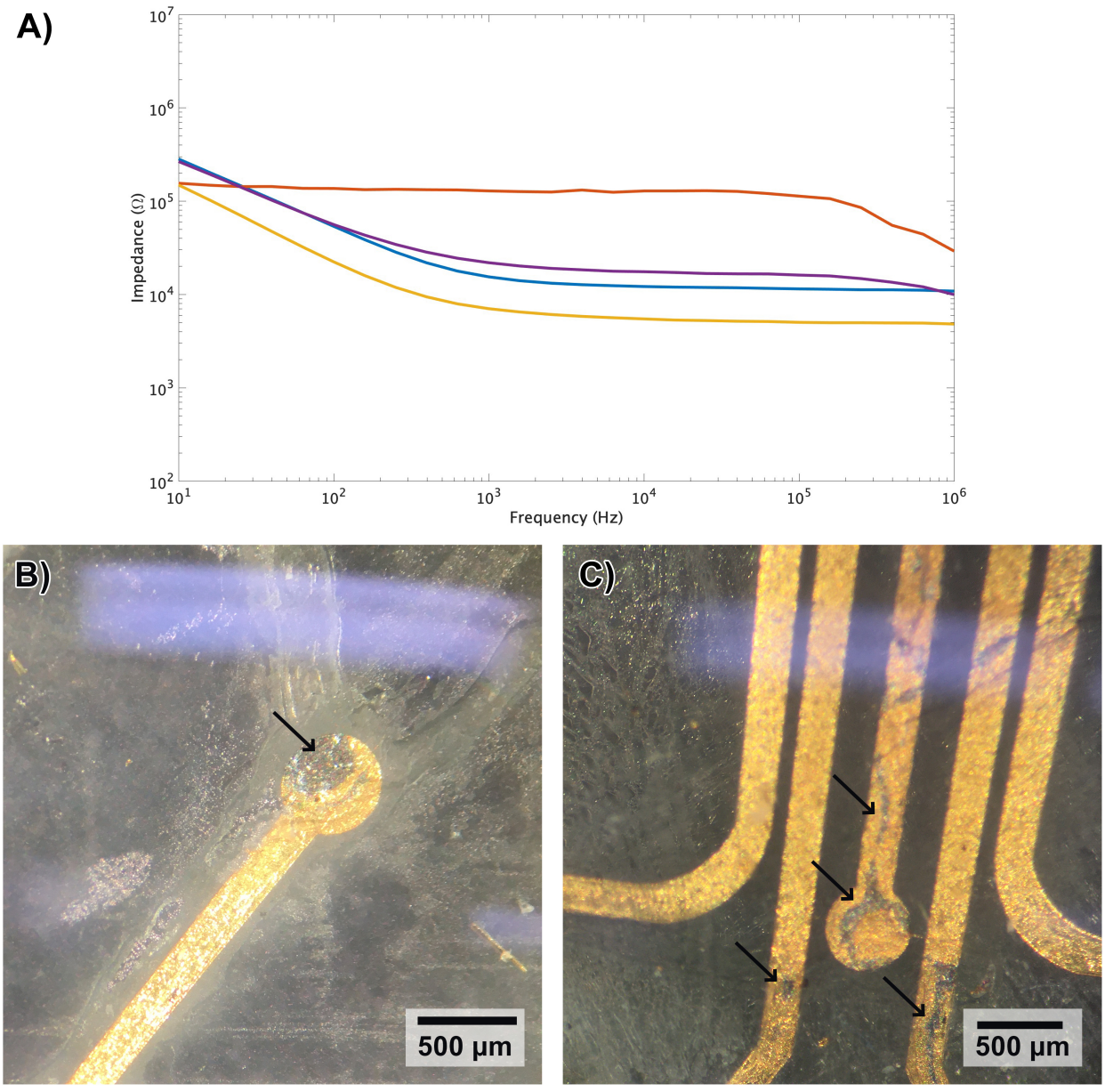

Figure 19 Electrical performance and surface characterization of PDMS/Parylene C hybrid electrode array. (a) EIS spectrum of 4 functional electrodes out of 7 fabricated electrodes indicated by 4 colors. (b) and (c) Arrows indicated the silver-colored regions as fully opened area, which were electroplated with platinum/iridium. The gold-colored surface was unopened. Openings on electrodes were not sufficient and unwanted exposure was also found on the conductive tracks.

3.4.3 Fabrication of polyimide/PDMS hybrid electrode array

Based on the experiences we gained from the fabrication of PDMS/parylene C hybrid, we decided to deposit and pattern metal layers on polyimide to avoid including PDMS in photolithography procedures. Then we sandwiched the polyimide-based electrode array between two layers of PDMS. The fabrication of electrodes and conductive tracks on polyimide had fewer defects and resulted in a higher yield of functional electrodes. SEM images showed the uniform surface of the gold electrode and the conductive tracks were fully insulated by the polyimide (**Figure 20 a**).

Some research groups had reported on different surface treatments to promote bonding between sandwiched polyimide and PDMS, including oxygen plasma [110] and using poly(methyl methacrylate) (PMMA) [171]. Print transferring PI to PDMS was also reported [109]. We used oxygen plasma to treat the surface of the two layers of PDMS and laminated them to form a strong bond [172]. Eventually, because the area of the PI-based electrode array was much smaller than the PDMS contact surface, the PI-based device was enveloped tightly between the two layers of PDMS. SEM images suggested the full exposure of the electrode sites (**Figure 20 b**). Notably, the openings on PDMS layer were larger than the dimension of the electrode. In this case, because PI insulation defined the electrode area, the extra width of the PDMS opening had not effect on electrode properties. This method was established as the process for making retinal arrays that we evaluate in for the next chapter.

As discussed before, micromachining on PDMS remained a challenging topic. Some research groups have demonstrated micro-patterning capability on PDMS with a higher

resolution, but specialized equipment is needed that was not available to us for this project [100]. Future optimization of the protocol could benefit from those new solutions.

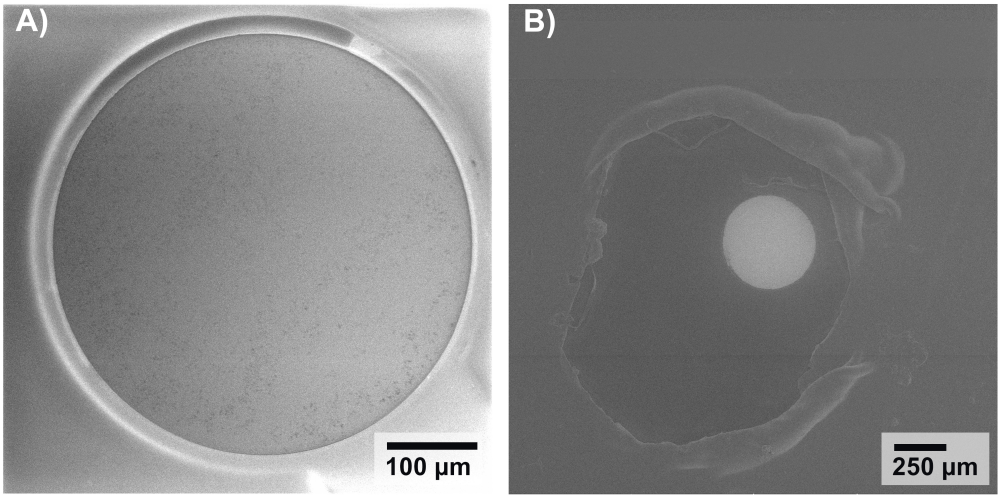

Figure 20 SEM images characterized the surface of the electrodes. (a) Gold electrode with a diameter of 500 um was well insulated by polyimide. (b) Polyimide electrode array was sandwiched between two layers of PDMS. The openings on the top layer of PDMS were larger than the diameter of the electrode.

3.5 Conclusion

PDMS is flexible, biocompatible, and transparent, which makes it a promising material as the substrate for retinal prosthesis. However, because of its low surface energy, high thermal expansion coefficient, and porous structure, which is sensitive to organic solvents and vacuum, standard photolithography is challenging on PDMS.

We have explored different methods to approach a PDMS-based electrode array and established a protocol with the polyimide device sandwiched between two layers of PDMS. We were able to produce electrode arrays with better yields and good electrical performance. The results will be discussed in detail in the following chapter.

Chapter 4 Characterizations of the Responsive Full-field Array as Epiretinal Prosthesis

4.1 Abstract

Shape-morphable electrode arrays can demonstrate their ability to form 3D surfaces conforming to organic neural tissues. Notably, retinal prostheses need a curved interface to fit the spherical retina and wide coverage to restore peripheral vision. In this study, we developed a 6-petals full-field array (FFA) with hydrogel coating that can 1) cover a visual field of 57° based on electrode position and 113° based on the substrate size; 2) compact and fix in a temporary shape before implantation; 3) self-deploy into a curvature fitting the retina responding to moisture after implantation. We characterized the electrical performance of the FFA. We found electrodeposition or high surface area platinum/iridium (Pt/Ir) alloy significantly lowered the impedance and improved the CSC_C of the electrodes, and at the same time reduced the variation induced by contaminations on the electrode surface. Hydrogel coating compromised the electrical properties but still demonstrated better electrical performance compared with before electrodeposition. An equivalent circuit model was used to further analyze the effects of electrodeposition and hydrogel coating. Then, we compacted the FFA into a temporary shape and inserted it into *ex vivo* pig eyes. The planar FFA transformed into a 3D curved surface responding to moisture in the eye. After implantation, electrodes demonstrated comparable electrical properties compared with before implantation.

4.2 Introduction

Neural prostheses are widely used to treat and modulate various neural disorders [173]. However, traditional flat electrode array using planar processes may not conform well to soft neural tissues, which have organic curvatures and dynamic movements. Thus, compression and shear created by on the neural interface can damage the nerves and induce severe immune responses and formation of fibrosis [174]. In addition to mechanical damage, increased distance from electrodes to the target tissue due to non-conformity can reduce stimulation efficiency and safety [72]. In particular, the need for a curved electrode array is essential for retinal prosthesis because of the natural spherical structure of the eye.

Shape morphable neural interface attracted a wide range of studies in recent years because of its ability to reconfigure into 3D shapes to conform to its target tissues [29], [30], [123], [175]. Materials including shape memory polymers [82] and hydrogels [176] can not only provide shape reconfiguration responding to various stimuli but also can have multi-steps shape transitions, which makes a temporary compact status of the prosthesis available to reduce surgical complications.

Among those materials, hydrogel can be designed to respond to different stimuli, including temperature [121] and moisture [111], which are two factors common in the human body. Hydrogel can be fixed at a random shape by dehydration and recover to its permanent shape after swelling. In addition, hydrogel is very soft with an elastic modulus ranging 1-100 kPa, and can be biocompatible depending on the compositions [177], [178], which make it a promising material for implantable electronics.

We have designed a full-field array (FFA) coated with a polyacrylamide (PAAm) hydrogel layer as an epiretinal prosthesis. We studied the electrical properties of the fabricated

electrode array and found the electrodes had significantly lower impedance and higher charge storage capacity after electrodeposition with platinum/iridium (Pt/Ir) alloy. The electrical properties were compromised after hydrogel coating but maintained a better performance than before electrodeposition. Then, a simulation surgery was performed to implant the FFA with a compact temporary shape in pig eyes. The FFA deployed into a 3D flower shape in aqueous environment. The conformed curvature of the device can effectively reduce damage to the retina, and the ability to be compact and folded is beneficial for the fabrication of wide-field prosthesis with the potential for an acceptable sclerotomy size. Neural interface combining with shape-morphable hydrogel has promising potentials in many applications that require conformation with a 3D anatomical structure.

4.3 Materials and methods

4.3.1 Materials

For hydrogel coating, acrylamide (AAm; Sigma–Aldrich A3553; ≥99%), 2-hydroxy- 2-methylpropiophenone (Irgacure 1173; Sigma–Aldrich 405655; 97%), N, N′-Methylenebisacrylamide (MBAM; Sigma–Aldrich M7279; ≥99.5%), benzophenone (Sigma–Aldrich B9300; ≥ 99%) were used. Sodium hexachloroiridate (III) hydrate ($Na_3IrCl_6H_2O$; Sigma–Aldrich 288160), sodium hexachloroplatinate (IV) hexahydrate ($Na_2PtCl_6H_2O$; Sigma–Aldrich 288152; 98%), nitric acid (HNO3; Sigma–Aldrich 438073, 70%) were used in electrodeposition. For electrical characterization, phosphate buffered saline (PBS; Sigma–Aldrich P4417) was used.

4.3.2 Packaging the PDMS/polyimide/PDMS electrode array

To build the connectors for electrodeposition and electrical characterizations, each contact pad on the PDMS/polyimide/PDMS electrode array (Chapter 3) was covered with silver epoxy (silver epoxy adhesive, Epo-Tek H20E Adhesive) as an adhesive conductive layer. Then a tinned copper wire (bus bar wire 28 awg, Alpha Wire, Elizabeth, NJ, USA) adhered to the silver epoxy, and the wire was long enough to allow connection with alligator clips for electrical access to each electrode. The silver epoxy was cured at 50 °C overnight to prevent excessive thermal stress on PDMS.

4.3.3 Platinum/Iridium (Pt/Ir) alloy electrodeposition

As described in prior work [179], the plating solution was prepared and consisted of 0.2 g/L $Na_3IrCl_6H_2O$ and 0.186 g/L $Na_2PtCl_6H_2O$ in 0.1 M of nitric acid (HNO_3). The solution was boiled until the color turned reddish, and then was cooled down to 45°C. The temperature was kept at 45°C throughout the deposition. A pulsing sonication (A700 Qsonica, Qsonica L.L.C. Newtown, CT, United States) at a power of 2 W (sonication on = 1 minute and sonication off = 30 seconds) was used to maintain the constant mass transfer.

The Pt/Ir electrodeposition was done using a potential cycling method (Gamry 600+ potentiostat, Gamry Instruments, Warminster, PA, United States). A three-electrode setup was used during the potential cycling, which consists of a Pt/Ir wire with a diameter of 70 μm (A-M System, Sequim, WA, United States) as the counter electrode, an Ag/AgCl (3M NaCl, BASi, West Lafayette, IN, United States) reference electrode, and the PDMS/polyimide/PDMS electrode array as the working electrode. The potential was scanned from -0.1 to 0.1 V with a scan rate of 200 mV/s for 1500 cycles.

4.3.4 Hydrogel coating and curvature analysis

The top layer of PDMS with electrodes openings was covered by benzophenone solution (10 wt% in ethanol) for 4 min. Then, the surface was washed with methanol three times and dried in air to remove excessive benzophenone. AAm was dissolved in water to form a pre-solutions with 15 wt% of AAm. The cross-linker ratio (the weight ratio of MBAM to AAm) was fixed at 3.89%, and the initiator ratio (the weight ratio of Irgacure 1173 to AAm) was fixed at 0.356%. The pre-gel solution was poured into the Teflon mold with a height of 100 μm. The benzophenone-treated PDMS surface was flipped on top of the mold. The pressure from the PDMS ensured the even distribution of the pre-solution in the mold. The pre-gel solution was cured under an ultraviolet lamp (ML-3500C, Spectroline, Westbury, NY, USA) for 10 min. After curing, the FFA was carefully peeled off along the laser-ablate outline, and the FFA was put in 0.01 M PBS, which caused the hydrogel to swell and the electrode array to form a 3D flower shape.

After the FFA swelled and reached the final curvature, a camera (D7200, Nikon, Tokyo, Japan) was used to take photos of the hydrated multilayer, and the curvature analysis was done using the digital imaging processing software Fiji and the plugin Kappa. Kappa measured the curvature of each point along the diameter spline of the electrode array, then the average of the curvature was used to represent the curvature of the electrode array.

4.3.5 Electrochemical impedance spectroscopy and cyclic voltammetry

Electrochemical impedance spectroscopy (EIS) was collected using a potentiostat (Gamry 600+ potentiostat, Gamry Inc., Warminster, PA, United States). EIS was performed with a 10 mV (peak) sine wave at a frequency range of 10 Hz–1 MHz in a solution of 0.01 M PBS with the three-electrode setup. Experimental data were fitted to an equivalent circuit model, and

the values of the electrolyte resistance (Ru), the admittance (Y0), the exponent (α) of the constant phase element (CPE), and the parasitic capacitance (C) were calculated [179].

Cyclic voltammetry (CV) was measured with the three-electrode setup using the potentiostat in 0.01 M PBS. The voltage was swept from -0.6 to 0.8 V vs. Ag/AgCl at a scan rate of 50 mV/s. Cathodal charge storage capacity (CSC_C) was calculated from the integration of the area of the time-dependent cathodic current curve.

4.3.6 Voltage transients

An electrical stimulator system (PlexStim Electrical Stimulator System, Plexon, Dallas, TX, United States, software version 2.3) was used to deliver cathodic first biphasic electric pulses with a charge density of 0.1 mC/cm^2 in 0.01 M PBS. A Pt/Ir wire with a diameter of 70 μm was used as the counter electrode. The voltage transient and the current was captured using an oscilloscope (Tektronix TBS 1032B, Tektronix, Beaverton, OR, United States). The most negative maximum polarization E_{mc} and maximum negative potential were extracted from the data [1].

4.3.7 Ex vivo acute implantation surgery in pig eyes

Pig eye is used as the eye model because of its availability and similarity to human eye [180].

The FFA was carefully rolled up with polyvinyl alcohol (PVA) film (water soluble stabilizer, Superpunch, Quebec, Canada) and placed in a straw. PVA film was water soluble and facilitated the rolling process. Following overnight dehydration of the hydrogel, the electrode array was fixed at a temporary compact shape.

The porcine eye was fixed to a styrofoam block. Three DORC (EVA Phaco-Vitrectomy system, Dutch Ophthalmic USA, Inc., Exeter, NH, USA) 25g valved trocars were placed 4mm posterior to the limbus at 2, 4 and 10 o'clock. Then, a central 7mm ring was measured in the cornea, and excised using curved scissors. The Landers keratoprosthesis (The Landers Widefield Temporary Keratoprosthesis, Ocular Instruments, Bellevue, WA, USA) was then sutured into position using six 9-0 nylon sutures. The infusion line was inserted into the 4oc trocar, and opened. Then porcine crystalline lens was removed using a 25g microvitrector. Then, a wide-field contact lens was placed onto the keratoprosthesis, and a core vitrectomy was performed. Once adequate vitrectomy was completed, a 90-degree peritomy was performed from 6 to 9 o'clock. Then, a 12 mm scleral wound was fashioned using a 64 blade scalpel 4mm posterior to the limbus.

The device was implanted in one of two fashions: either a rolled insertion, where the device was rolled, grasped in non-toothed forceps, then directly driven through the scleral incision, or by a "Petal Walk" technique, where the device was not rolled, but each petal was individually introduced through the scleral tunnel. Care was taken to minimize trauma to the device during the petal walk to avoid shearing the plastic housing. With rolled insertion, it was critical to insert the device quickly, in one movement, to avoid the PVA coating from dissolving on contact with fluid and allowing the device to unroll prematurely. Once the device was inserted with either method, its conformation to the retina was observed. Then, three to four 9-0 nylon sutures were placed in simple interrupted fashion to close the sclerotomy.

An open-sky method was used to cut the pig eye in half after the implantation to better image the deployed device in the pig eye.

4.3.8 SEM and statistical analysis

SEM images were taken (Tescan Rise, Tescan Orsay Holding, Brno-Kohoutovice, Czech Republic) in a low vacuum mode to prevent the deposition of conductive films on top of the electrodes. The electrode was steadily adhered to an SEM stub using carbon tapes.

A paired t-test was used to compare the data before and after each of the following treatments: electrodeposition, hydrogel coating, and *ex vivo* acute implantation. Data including the impedance of electrodes at 1 kHz, CSC_C, and the parameters calculated from the circuit model were analyzed. Outliers of electrodes are defined if their impedance at 1 kHz is less than q1 – 1.5 × (q3 – q1) or greater than q3 + 1.5 × (q3 – q1), in which q1 and q3 are equal to the first and the third quartiles of the impedance data based on all the 14 electrodes. Notably, because of the existence of the outliers, we presented *p*-value from the paired t-test both with and without outliers in most of the analyses, and the alpha level was 0.05. Sample sizes with or without the outliers are described case by case in the results section.

4.4 Results

4.4.1 Design and fabrication

Our goal is to conduct a pilot study of the novel FFA. The multilayered epiretinal prosthesis is a flexible, foldable, and responsive full-field prosthesis with a 3D curvature in an aqueous environment. The prosthesis is based on the PDMS/polyimide/PDMS electrode array (processes discussed in detail in Chapter III), which consists of a polyimide-based electrode array sandwiched between two layers of PDMS, combine with a hydrogel layer (**Figure 21 b**). Polyimide, widely used neural interfaces, provides a high yield of well-insulated and functional electrodes. PDMS, on the other hand, functions as both the mechanical support and the direct interface with the hydrogel. The shape of the device was made as a 6-petal flower with a central circular area of 6 mm. The diameter of the flower from a petal tip to the opposite petal tip was 34

mm, and was designed to cover a visual field of 113.9° [154]. 7 electrodes with a diameter of 460 um were patterned on the substrate (1 in the center and 1 on each petal), and they can cover a visual field of 57°. The electrodes were electrodeposited with Pt/Ir alloy to improve the electrical performance of electrodes.

Then, the top layer of the PDMS was coated with a polyacrylamide (PAAm) hydrogel layer [111]. The transparency of PDMS allowed the UV light to pass and cure the hydrogel. The hydrogel can swell with water and increase the volume, while the volume of PDMS remained constant in water. The residual stress on the interface between the hydrogel and PDMS induced the FFA to form a 3D curvature in an aqueous environment, resembling a flower **(Figure 21 a)**. Ideally, the radius of curvature of the device should be around 11 – 12.5 mm to fit to the retina based on the ocular axial length of human eyes being around 22 – 25 mm [181]. **Figure 21 c** demonstrated a device with the radius of curvatures of 15.63 mm in 0.01 M PBS.

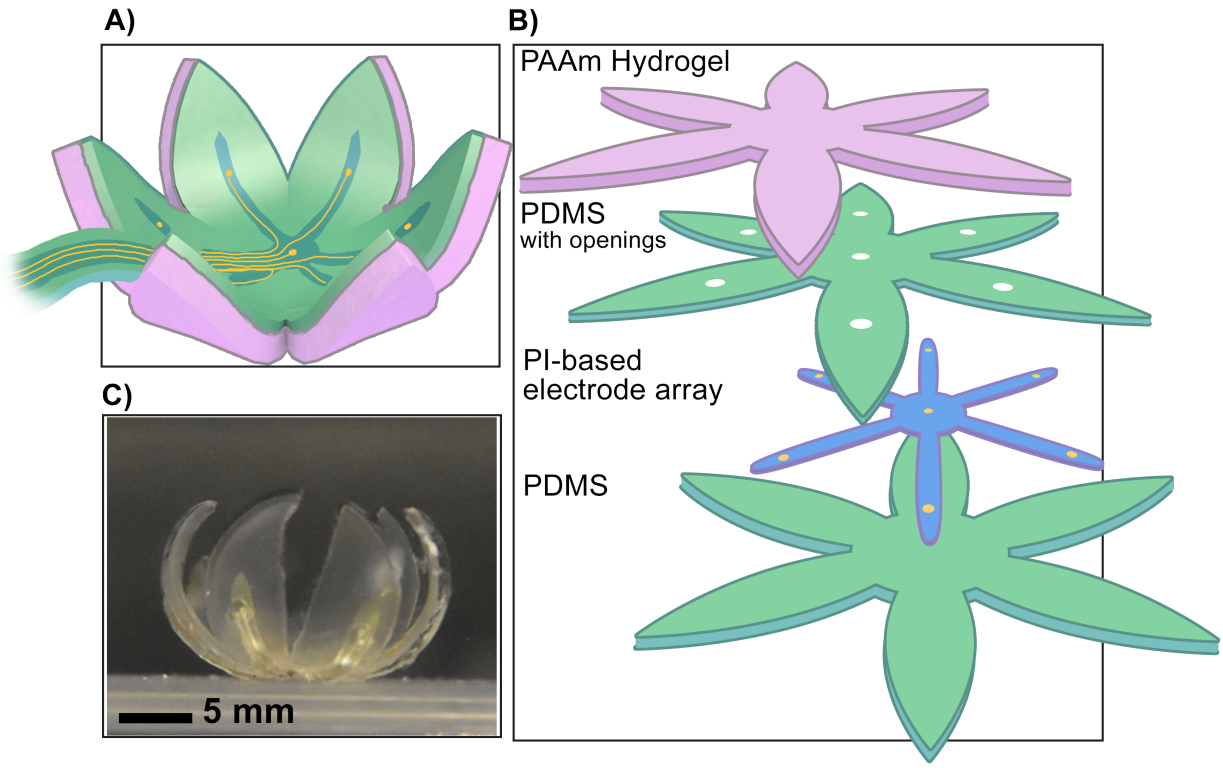

Figure 21 Conceptual illustration of the FFA and photo of a curved electrode array in 0.01 M PBS. (a) Illustration of the device with a fully swollen hydrogel layer. Notably, the illustrated metal electrodes were only an indication of the location of the electrodes, and the electrodes were opened on the same side as the hydrogel. (b) Layer-to-layer composition of the FFA. (c) A photo of the curved FFA placed on a supportive platform in 0.01 M PBS.

4.4.2 Electrical performance evaluation

Different surface modifications are performed on the electrodes, including electrodeposition and hydrogel coating. It is important for us to understand how the modifications affect the electrical properties. The electrodeposition of Pt/Ir alloy on the electrode surface aims to increase the charge storage capacity and lower the electrochemical impedance of the electrodes [147]. PAAm hydrogel is reported to have an increased resistivity as concentration increases [182], and it is our interest to study the effect of hydrogel coating on the electrode properties.

We evaluated 14 electrodes on 2 devices in total and compared their impedance, the CSC*c*, and voltage transients before/after the electrodeposition, and before/after the hydrogel coating. **Figure 22 a** showed a box plot of the impedance at 1 kHz of 14 electrodes on two FFAs (7 electrodes each), device A and device B. The average impedance at 1 kHz of the 14 electrodes was measured before electrodeposition as 42.92 ± 82.06 kΩ, after electrodeposition as 0.95 ± 0.05 kΩ, and after hydrogel coating as 7.50 ± 20.95 kΩ. The impedance of the electrodes decreased after electrodeposition, and increased after hydrogel coating, but was still lower than electrodes before electrodeposition. Notably, the huge variation of the impedance of naïve electrodes, especially comparing between two FFAs, was induced by contaminations on the electrode surfaces. Since the fabrication steps involved bonding the electrode array with another layer of PDMS outside of the cleanroom, we have found some contaminations, including residual PDMS and SEM-induced contaminations. There were also slightly different processes used to characterize the two devices. Device A, demonstrating more variation of the impedance, was contaminated with carbon deposition during SEM imaging, while Device B was not imaged using SEM. Two EIS spectrums of representative electrodes suggested that some electrodes had a higher increase of the impedance at high frequency than other electrodes after hydrogel coating, suggesting increased resistivity in the conducting path due to the hydrogel coating (**Figure 22 b**).

When including the outliers for statistical analysis (**Table 1**), a significant decrease of the impedance at 1 kHz of 14 electrodes was noted after electroplating with Pt/Ir alloy (one-tail paired t-test, *p*-value of 0.039), and no significant difference was observed after hydrogel coating. However, with outliers excluded and 8 electrodes analyzed, we found not only the decrease of the impedance after electrodeposition was significant (one-tail paired t-test, *p*-value

of 0.009), but also the increase of the impedance after hydrogel coating showed statistical significance (one-tail paired t-test, p-value of 5.042×10^{-4}).

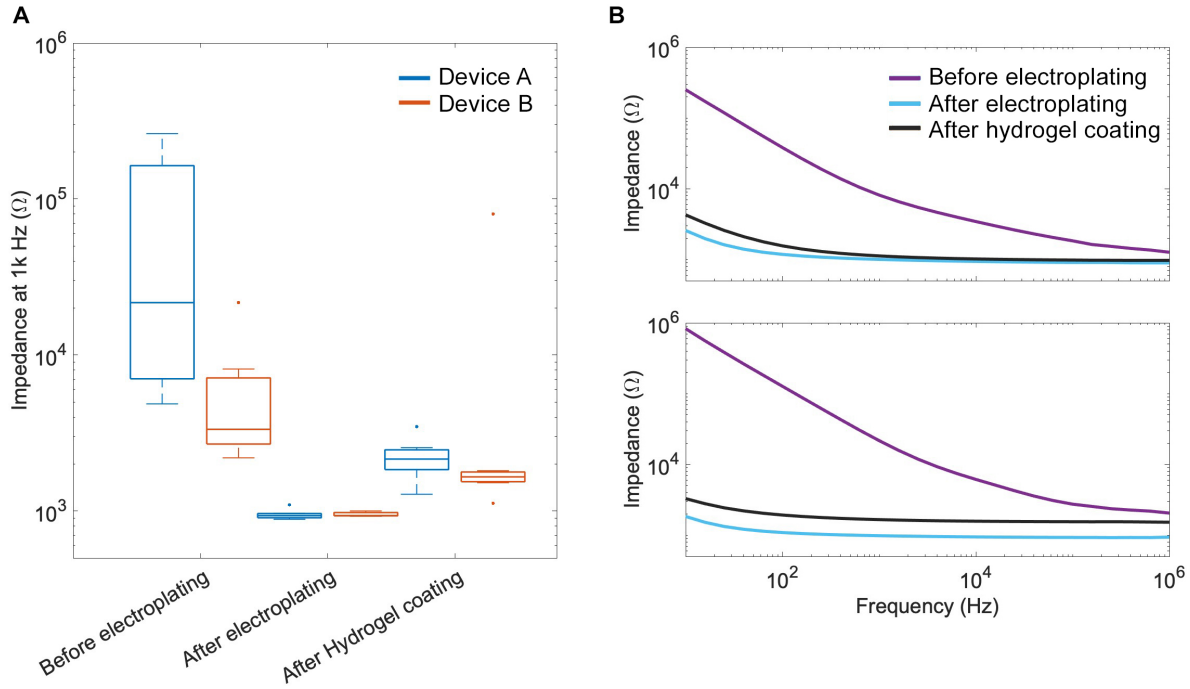

Figure 22 Impedance characterization of electrodes. (a) A box-and-whisker plot demonstrated the distribution of impedance of electrodes at 1 kHz. Device A (7 electrodes) was labeled blue and Device B (7 electrodes) was labeled orange. The box represented the range of data between the first and the third quartile, and the whiskers represented the maximum and minimum data points without outliers (labeled in dots). The solid line inside the box was the median value. (b) Two representative EIS spectrums of two electrodes.

Table 1 One-tailed p-value using paired t-test. The impedance at 1 kHz and CSC_C were compared after sequential treatments. Evaluations were made both with outliers (14 electrodes) and without outliers (8 electrodes). BE: before electroplating; AE: after electroplating; AH: after hydrogel coating. *p: p*-value of all data; *p': p*-value of data with outliers excluded.

Comparison	Impedance at 1 kHz		CSC_C	
	p	*p'*	*p*	*p'*
BE vs.AE	0.039	0.009	1.997×10^{-8}	1.115×10^{-4}
AE vs. AH	0.132	5.042×10^{-4}	4.632×10^{-8}	1.051×10^{-4}

The EIS data were fitted into an equivalent circuit model (**inset in Figure 23**) to further analyze the electrical properties, and the model fitted the experimental data well. The circuit

model consists of the electrolyte resistance (Ru), the admittance (Y0), and the exponent (α) of the constant phase element (CPE), and the parasitic capacitance (C). One fitting spectrum was selected as a representative example (**Figure 23**). The parameters calculated by the fitting model were listed in **Table 2** with standard deviation and two-tailed t-test *p*-value. Increased admittance (Y0) confirmed a lower impedance of the electrodes after electrodeposition. The difference of electrolyte resistance (Ru) indicated the change of the electrode geometry after deposition and after hydrogel coating, the former induced by the cleaning during electrodeposition, and the latter caused by adding an extra hydrogel layer on top of the surface. When analyzing the statistical significance, we again confirmed that outliers can heavily affect the results. Paired t-test two-tail *p*-value suggested significance in Y0 and α before/after electroplating, and Ru and α before/after hydrogel coating. When excluding the outliers, all four parameters showed significance before/after electrodeposition. Ru and α showed significant change before/after hydrogel coating. In conclusion, electrodeposition modified the electrode surface by depositing Pt/Ir alloy (Y0 changed) and changed the electrode geometrical shape due to electrodeposition-induced cleaning (Ru changed). While hydrogel coating changed the electrode geometrical shape by covering electrode with hydrogel (Ru changed) but showed less surface modification (Y0 unchanged).

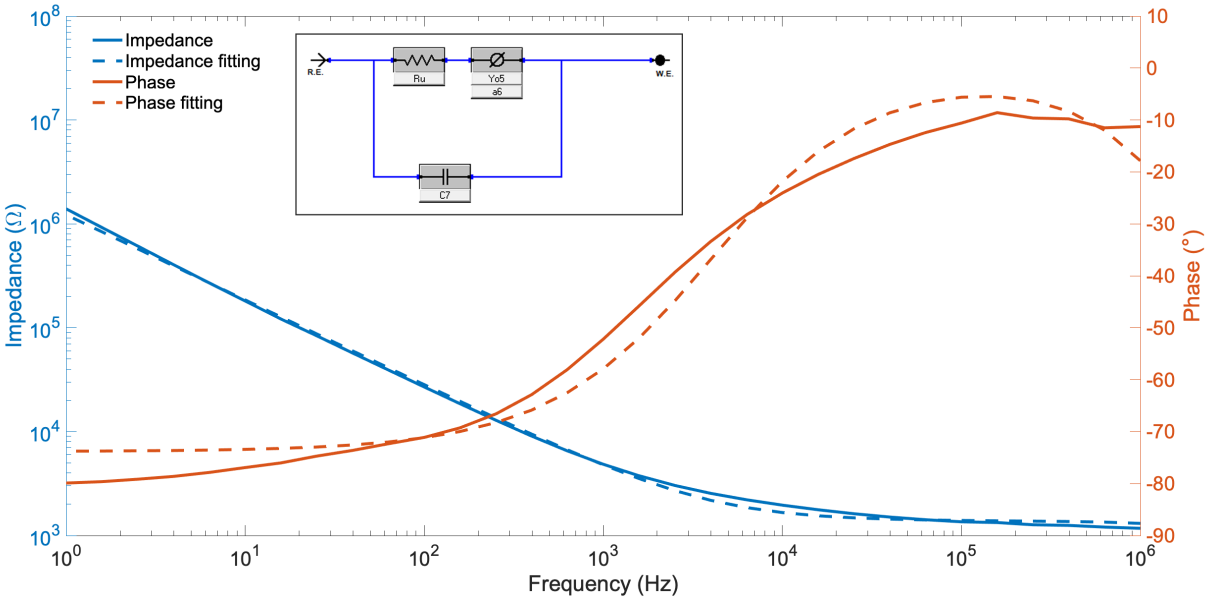

Figure 23 Representative plot of model fitting of the EIS measurements of one electrode using an equivalent circuit model before electrodeposition. The experimental data was reported in solid blue line for impedance and solid orange line for phase. The fitted impedance was reported as blue dashed line and orange dashed lines separately. The inset showed the equivalent circuit model used to fit the experimental data.

Table 2 List of all the components extracted from the equivalent circuit model shown in **Figure 23** and two-tailed *p*-value using paired t-test, including the electrolyte resistance (Ru), the admittance (Y0), the exponent (α) of the constant phase element (CPE), and the parasitic capacitance (C). Evaluations were made both with outliers (14 electrodes) and without outliers (8 electrodes). BE: before electroplating; AE: after electroplating; AH: after hydrogel coating. *p: p*-value of all data; *p': p*-value of data with outliers excluded.

	Ru/Ω		Y0/(S×s$^{\alpha}$)		α		C/F	
BE	6216.86 ± 110.80		$1.42 \times 10^{-7} \pm 2.23 \times 10^{-9}$		0.784 ± 0.002		$3.27 \times 10^{-11} \pm 2.05 \times 10^{-12}$	
AE	911.79 ± 5.55		$1.53 \times 10^{-5} \pm 3.47 \times 10^{-7}$		0.862 ± 0.006		$2.81 \times 10^{-11} \pm \times 10^{-12}$	
AH	1583.44 ± 3848.57		$1.42 \times 10^{-5} \pm 6.62 \times 10^{-7}$		0.652 ± 0.007		$2.58 \times 10^{-11} \pm 2.03 \times 10^{-12}$	
p-value	*p*	*p'*	*p*	*p'*	*p*	*p'*	*p*	*p'*
BE vs. AE	0.101	0.011	2.367×10^{-7}	1.314×10^{-5}	0.016	0.033	0.259	0.014
AE vs. AH	0.001	0.001	0.257	2.628×10^{-5}	0.002	3.780×10^{-5}	0.547	0.255

CV was performed on all the electrodes, and a representative CV curve was shown in

Figure 24. The calculated CSC_C characterized the amount of charge the electrode can inject

during the reversible cathodic phase of a stimulation pulse. The average CSC*c* of 14 electrodes increased from 0.78 ± 0.39 mC/cm^2 to 28.90 ± 9.31 mC/cm^2 after electroplating with Pt/Ir, suggesting a significant improvement of the charge injection limit (one-tailed paired t-test, *p*-value of 2.00× 10^{-8}). After hydrogel coating, there was a significant reduction of the CSC*c* to 13.06 ± 4.12 mC/cm^2 (one-tailed paired t-test, *p*-value of 4.63× 10^{-8}), but still much higher than before electrodeposition.

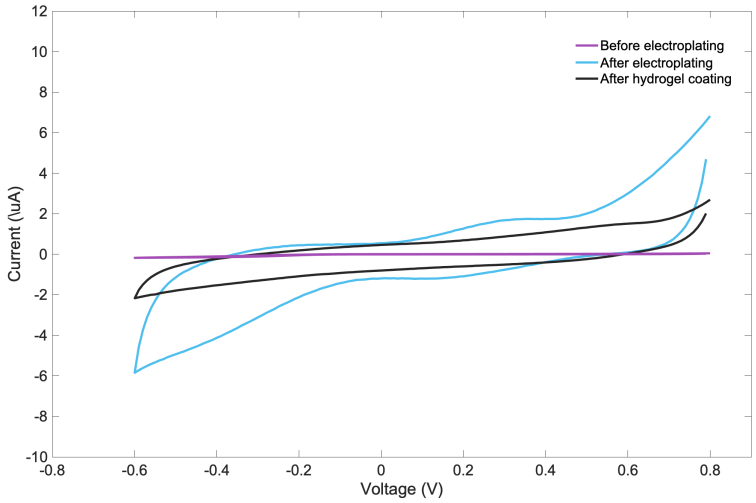

Figure 24 CV of an electrode before (purple) and after (blue) the Pt/Ir electrodeposition, and after hydrogel coating (black).

Voltage transients using a biphasic stimulation pulse were used to estimate the maximum charge that can be safely injected through the electrode without exceeding the water window. Three-electrode setup was commonly used, but we used a two-electrode setup here without the reference electrode. Pulsing the electrode at 0.1 mC/cm^2 demonstrated that the most negative maximum polarization E_{mc} was within the water window of Pt/Ir both before and after hydrogel coating, suggesting the safety of stimulation with the hydrogel layer. When comparing before and after hydrogel coating, the average maximum negative potential decreased from -318.57 mV

to -264.29 mV, which was opposite from our observation from the impedance and CSC*c*. However, the change was not statistically significant.

4.4.3 Surface morphology of electrodes

Electrodeposition plated the electrode surface with a thin layer of Pt/Ir alloy. SEM images were collected after the electrodeposition, and a homogenous thin film of Pt/Ir was observed on the electrode surface (**Figure 25 a**). Some micro-cracks were found on the surface at a higher magnification. Energy dispersive spectroscopy (EDS) was done to identify the percentage of Pt and Ir on the electrode surface (**Figure 25 b**). A percentage of 59% for Pt and 41% of Ir was measured on one electrode, comparable with previous results [179].

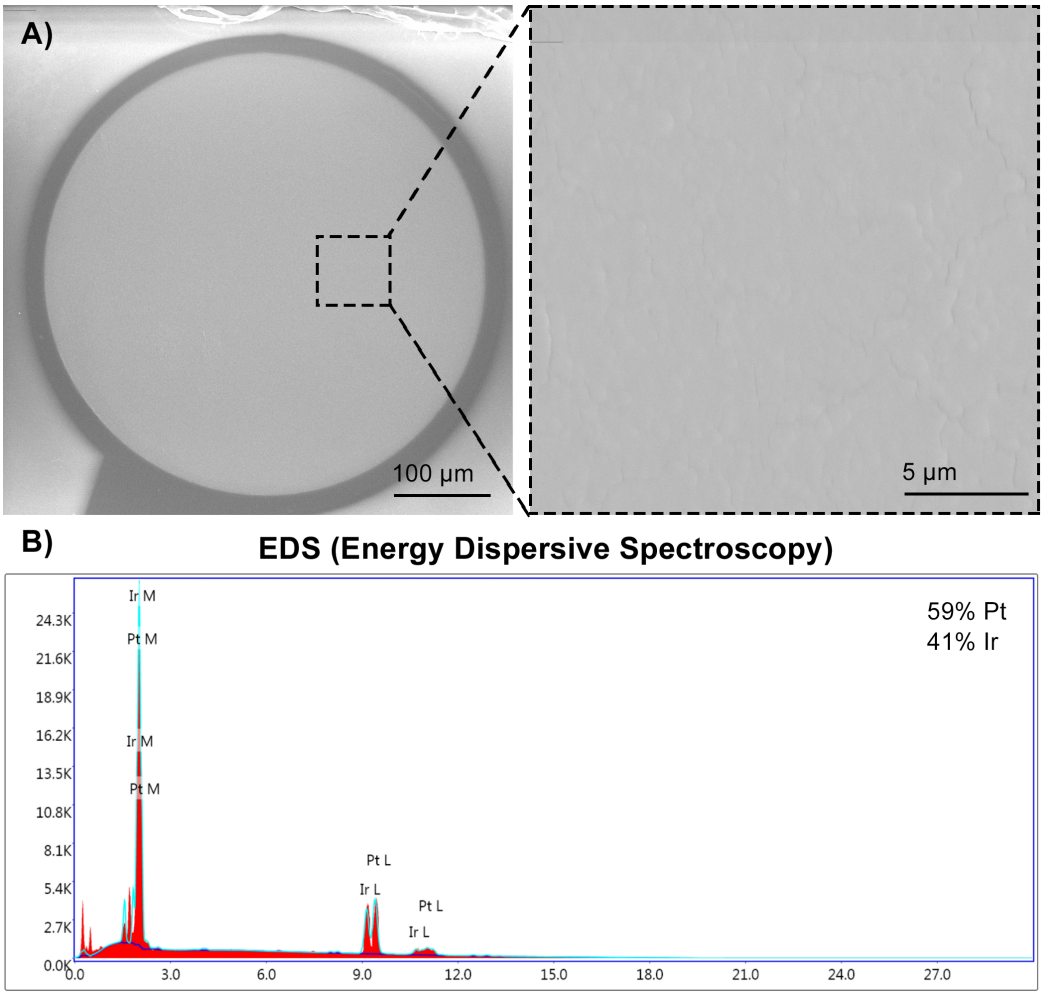

Figure 25 SEM image and EDS characterization of one representative electrode. (a) SEM image of one electrode demonstrated the insulation of polyimide and the Pt/Ir alloy coating on the electrode surface. (b) Chemical spectra from the EDS map on the electrode active surface indicated two different peaks associated to Pt and Ir both at 9 keV and 11 keV.

4.4.4 Surgical simulation

To minimize the incision on the sclera, the full-field prosthesis should be folded as compactly as possible. The excellent flexibility of PDMS guarantees the foldability and the hydrogel allows the fixation of a temporary shape after dehydration of the multilayered prosthesis. The FFA was rolled up with water-soluble PVA film and fitted into a plastic straw, which we previously cut one side open to allow it to be wrapped around the rolled-up electrode.

Then, the rolled electrode array in the straw was dried at room temperature overnight. After removing the straw, the final diameter of the rolled-up FFA was 8 mm (**Figure 26**).

The device was implanted in one of two fashions, with each fashion performed in one pig eye: either a rolled insertion or by a "Petal Walk" technique, where the device was not rolled, but each petal was individually introduced through the scleral tunnel. To provide a better understanding of the interaction of the electrode array with the pig eye, the method of “open-sky” was adopted to cut the pig eye almost half-open. We found the deployed electrode array formed a continuous 3D curvature fitting to the eye and covered a wide field of the retina. After taking the electrode array out from the eye, the radius of curvature was measured 15.15 mm and the recovery rate was 96.97% compared with the curvature before implantation.

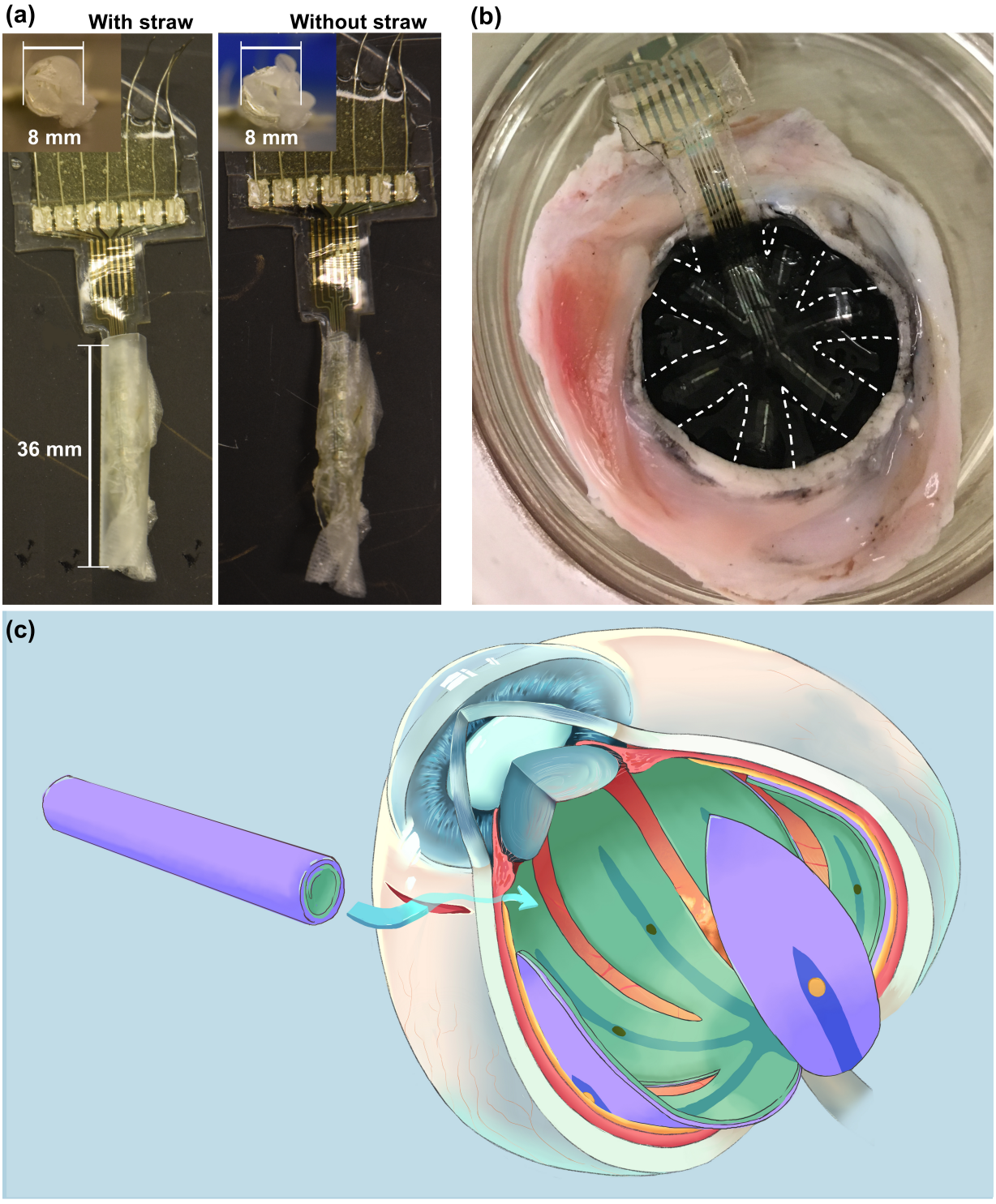

Figure 26 Simulation surgery to implant the multilayered device. (a) Preparation of the device before implantation. The multilayered prosthesis was rolled up with PVA film and placed into a straw with one side cut open. The inset was the cross-section of the rolled-up device, and the diameter was measured as 8 mm. After dehydration and the removal of the straw, the device stayed fixed and compact at a diameter of 8 mm. (b) Photo of the fully deployed multilayered electrode in pig eye after open-sky treatment. Dotted white line outlined the edges of the 6 petals. (c) Conceptual art of implanting the FFA in the eye.

4.4.5 Electrical performance evaluation after acute ex-vivo implantation

The implanted FFA was extracted from the eye and 6 electrodes on one array were assessed to evaluate the effects of deployment and implantation on electrical performance. 6 electrodes were based on the implantation of one FFA in the pig eye, and one electrode lost its connection after the implantation. The average impedance of these electrodes at 1 kHz was 2.11 ± 1.97 kΩ, measured after acute *ex vivo* implantation. The distribution of the impedance at 1 kHz was shown in **Figure 27 a**. Notably, the mean impedance decreased after the implantation. The CSC*c* remained 12.62 ± 7.56 mC/cm^2 after acute *ex vivo* implantation (**Figure 27 b**). Comparing electrodes after hydrogel coating and after implantation with outliers included, there was no statistically significant change of the impedance, the components of the model fitting (**Table 3**), and the CSC$_C$. The CSC*c* after acute *ex vivo* implantation was still significantly higher than CSC*c* before electroplating with a *p*-value of 8.90×10^{-4}. When excluding the outliers, we found that α and C showed significant change after acute implantation.

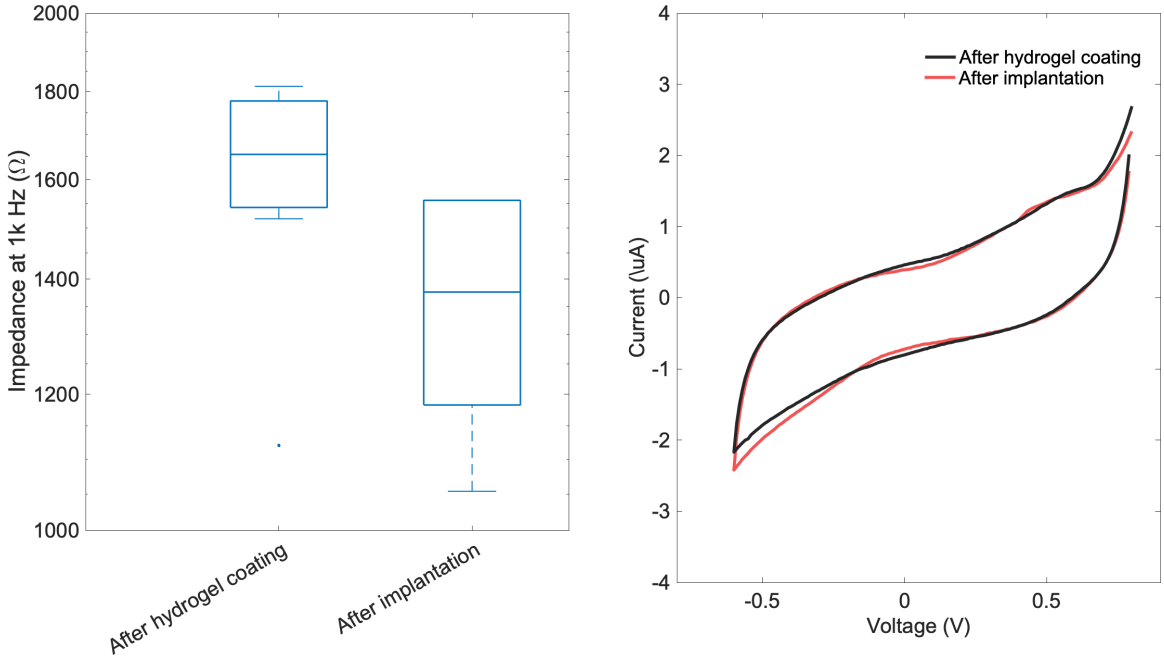

Figure 27 Impedance characterization of electrodes (n=6). (A) A box-and-whisker plot demonstrated the impedance of electrodes at 1 kHz after hydrogel coating and after implantation. The box represented the range of data between the first and the third quartile, and the whiskers represented the maximum and minimum data points without outliers (labeled in dots). The solid line inside the box was the median value. (B) CV curve of one electrode showed CV after hydrogel coating in black, and after implantation in red.

Table 3 List of all the components extracted from the equivalent circuit model shown in **Figure 23** and two-tailed *p*-value using paired t-test, including the electrolyte resistance (Ru), the admittance (Y0), the exponent (α) of the constant phase element (CPE), and the parasitic capacitance (C). Evaluations were made both with outliers (6 electrodes) and without outliers (4 electrodes). AH: after hydrogel coating, AI: after implantation. *p*-values from two-tailed paired t-test were included here. *p:* *p*-value of all data; *p':* *p*-value of data with outliers excluded.

	Ru/Ω		Y0/(S×s$^{\alpha}$)		α		C/F	
AH	1583.44 ± 3848.57		$1.42\times10^{-5} \pm 6.62\times10^{-7}$		0.652 ± 0.007		$2.58\times10^{-11} \pm 2.03\times10^{-12}$	
AI	1617.15 ± 12.014		$9.47\times10^{-6} \pm 1.90\times10^{-7}$		0.679 ± 0.004		$4.46\times10^{-11} \pm 2.77\times10^{-12}$	
p-value	p	p'	p	p'	p	p'	p	p'
AH vs. AI	0.438	0.053	0.080	0.061	0.567	0.038	0.248	0.001

4.5 Discussion

A foldable and flexible full-field epiretinal prosthesis can greatly benefit patients with RP to generate visual responses not only in the fovea but also in the peripheral retina. We developed a multilayered and responsive epiretinal prosthesis based on hydrogel, PDMS, and a polyimide-based electrode array. The FFA was fabricated in a planar fashion, and most of the fabrication procedures comply with cleanroom procedures. The device formed a 3D curvature in an aqueous environment, fitting the curvature of the retina. Our previous study has shown that the curvature could be customized by changing the formula of the hydrogel [111]. Currently, the radius of curvature among different devices demonstrated a variation due to the technical limitations of the mold for the hydrogel layer, but a more precise control of the thickness of customized hydrogels by using a finer spacer [183] and spin coating [184] is possible. Furthermore, there are studies exploring photo-sensitive polyimide coated with hydrogel as shape-morphable sensors [96]. The biocompatibility of those new materials needs to be assessed further for biomedical applications. Additionally, benzophenone, the photoinitiator bonding PDMS and hydrogel, may impose carcinogenic risks. A rigorous protocol removing excessive benzophenone from cured PDMS can alleviate the risks. Other biocompatible photoinitiators are also under development for future applications [185].

Then, we evaluated the electrical performance of the FFA. We found that contaminations from SEM and residual PDMS caused a variation of both impedance and CSC_C of the naïve electrodes, but electrodeposition effectively cleaned the electrode surface and improved the electrical properties of the electrodes, due to the properties of the Pt/Ir alloy [179]. After

electrodeposition, the standard deviation of the impedance at 1 kHz was reduced to 5.53%. This variation is similar to that found with a recent report of PDMS based microelectrode impedance [100]. Hydrogel coating increased the impedance and lowered the CSC_C. However, the reduced electrical capabilities are offset by the benefit of positioning the electrodes close to the retina, where a lower stimulus threshold is expected. We also noticed that the hydrogel coating was thinner at electrode sites and at area laminated with polyimide. It is possible that metal layers and polyimide allowed less UV light penetration compared with PDMS, which made metals and polyimide functioning as a natural photomask to pattern the hydrogel. In the future, precise micro-patterning the hydrogel with photomasks can be explored to leave electrodes completely free of the hydrogel coating [186].

Surgery simulation was performed using pig eyes to evaluate the process of implanting the novel multilayered device. Because our device can be rolled up and fixed at a compact shape with a diameter of 8 mm, the incision needed on the sclera was 1.2 cm, and the deployed electrode array had a diameter of 34 mm. Compared with Argus II with a 5 mm incision for a device with a diameter of 3 mm [9], the size-to-incision ratio was much higher. Optimizing the fabrication process to produce a thinner electrode array could further reduce the rolled-up diameter and leads to a smaller sclerectomy. The water-soluble PVA film used is a commercial grade film, but other thin films are available, such as oral thin films for drug delivery [187]. Synthesized PVA films with different solubility are also reported [188]. In addition, the “Petal Walk” technique can be applied to implant the device as an alternative because of its excellent flexibility. The unfolded prothesis covered most of the eye and formed a 3D configuration to conform to the retina. Notably, the size of the substrate of the electrode array covered a visual field of 113°, while the pilot study with 7 electrodes only covered 57°. Conceivably, an electrode

array could be designed to provide visual perception in the far periphery using approach we describe here. Since the interface was covered by hydrogel, the low Young's modulus of the hydrogel may limit damage to the retina.

We found that statistical significance with an alpha level of 0.05 was different with and without outliers. With continuous optimization, outliers can be minimized but cannot be eliminated. It is meaningful to consider the data, both with and without the outliers, to provide a thorough expectation for future fabrication. Since our goal was a demonstration of a full-field retinal array with 3D curvature, we included process steps, such as manual opening of PDMS holes in the top layer, that may have introduced variability. Instrumentation to more precisely pattern PDMS [100] was not available for this project. Process refinement and increasing the sample size will likely reduce the variability we noted in our electrical measurements.

4.6 Conclusion

We successfully fabricated a multilayered and responsive epiretinal array providing full-field coverage of the retina. The device is flexible and can reconfigure to a 3D curvature responding to moisture. Electrodeposition of Pt/Ir alloy greatly improved the electrical performance of the electrodes. We demonstrated a feasibility study of implanting the FFA with a compact shape in the pig eye, and the device spontaneously deployed in the eye.

Because of its flexibility, compact ability, and spontaneous deployment into a 3D shape, this FFA can be modified in design and provides new solutions to other neural applications, including peripheral nerve cuff.

Chapter 5 Summary of Contributions and Recommendations

5.1 Conclusion

Neural interfaces rely on the development of flexible and conformable electrode arrays to seamlessly interact with the targeted tissues. Notably, retinal prosthesis must have an interface with a 3D shape conforming to the curvature of the retina, wide coverage to restore peripheral vision, and a compact shape during implantation. Here, I develop a responsive multilayered epiretinal array consisting of hydrogel, polyimide-based electrode array, and silicone with the above-mentioned features. I also characterized the electrical performance of the electrode array and verified the feasibility of implanting the multilayered retinal array in pig eyes. I discuss the potential to apply this multilayered hybrid in other neural interfaces and discuss future directions for further research.

In Chapter 2, I developed the protocol for fabricating PDMS/hydrogel bilayer strips and characterized the bilayer system to lay the solid foundation for its application in the full-field array (FFA) [111]. Based on the knowledge of the effects of the hydrogel pre-solution formula on the properties of the polymerized hydrogel, we tuned the initial monomer concentration of the hydrogel pre-solution and found the curvature of the PDMS/hydrogel bilayer increased with the initial monomer concentration. We also found that with increased initial monomer concentration, the thickness and Young's modulus of the hydrogel layer increased, while the expansion strain decreased. Timoshenko's model verified how Young's modulus, thickness, and expansion strain of both layers affected the bilayer curvature and fitted well with the experimental data, which

provided us with rational design guidance for customized curvature of the bilayer. We also investigated the interface of the PDMS/hydrogel bilayer and proved that benzophenone, as the bonding agent, provided robust adhesion between the two layers, while the bonds formed by silane appeared unstable in the aqueous environment in the long term.

In Chapter 3, I explored two methods of fabricating electrodes on flexible substrates and made a sandwiched electrode array consisting of PDMS/polyimide-based electrode array/PDMS as the basis for the multilayered retinal prosthesis. I found that because PDMS is sensitive to temperature, organic solvents, and vacuum, microelectrode array fabrication procedures resulted in disconnected electrodes and cracks on the surface using the parylene C coated PDMS substrate. Furthermore, opening the electrode sites on PDMS was difficult with wet etching because of undesirable openings across the surface. Therefore, I developed a protocol combining the polyimide-based electrode array and two layers of PDMS. Polyimide guaranteed a high yield of functional electrodes and functioned as the direct substrate and the insulation layer for metal electrodes. The two PDMS layers, sandwiching the polyimide-based electrode array, provided both the mechanical support and an interface with the hydrogel layer. The top layer of PDMS was opened manually with the help of alignment marks.

In Chapter 4, I fabricated the FFA with a hydrogel layer, characterized the FFA, and investigated the feasibility of implanting the array in pig eyes. This work verified that different treatments on the electrodes affected the electrical performance of the electrodes. Electrodeposition of the electrodes with Pt/Ir lowered the impedance and increased the CSC_c effectively. While hydrogel coating increased the impedance and reduced the CSC_c, they remained improved compared with before electrodeposition. The variation of the electrical performance before electrodeposition was induced by contaminations but was reduced after

electrodeposition. I also investigated the feasibility of implanting the FFA in pig eyes. The FFA was able to be folded compactly and fixed at a temporary shape to minimize the scleral incision. The multilayered array was inserted into the pig eye either by “Petal walk” or at a compact shape, proving the flexibility of the implantation. After implantation, the FFA self-deployed into a 3D curvature fitting the curvature of the retina and covered a maximal visual field of 57° (maximally 113.9° calculated based on the size of the substrate). Compared to the wide-field photovoltaic array under development, our prosthesis covers a larger area on the retina and has more controllable implantation assisted by the compact shape [78]. In addition, our FFA uses hydrogel, which has a low modulus of 100 kPa, as the shape-changing motivator, and it is softer than shape memory polymers used in another study [30]. In general, the FFA provides full-field coverage together with excellent mechanical properties.

5.2 Future directions

5.2.1 Optimization of current full-field array

Chapters 2 and 3 show the FFA with hydrogel has the potential to function as a full-field epiretinal prosthesis. Future work should continue to optimize the current fabrication protocol from the following aspects: integrating high-resolution electrodes, opening precise electrode sites on PDMS, and simplifying layers.

The current pilot study only includes 7 electrodes in total, covering 57° of the visual field. Ideally, the fovea, where central vision is, should be stimulated with an electrode grid with higher spetial resolution than the peripheral retina [78]. One approach is to fabricate denser electrodes on polyimide since polyimide is capable of fabricating high-density electrodes with a diameter of 10 μm [189]. To note, a higher density of electrodes requires a high-throughput characterization and stimulation system [190]. Another approach is to integrate readily made

high density electrode arrays between the two layers of PDMS in the central area. For example, the diamond substrate device with 256 electrodes can potentially be readily integrated between the PDMS two layers [191]. While the central area will have an acceptable compromise in flexibility and curvature, the peripheral vision can still be covered by the flexible multilayered arms with the hydrogel, further improving visual acuity and coverage. Similarly, penetrating electrodes like carbon fibers can also be readily integrated into the multilayered system with a reduced distance from ganglion cells [179].

As for precise openings on the PDMS, laser ablation with a fine alignment can make accurate openings [100]. 3D printing of PDMS can pattern the PDMS and avoid opening the electrode sites after curing [107]. Other techniques, such as dry etching, can take a relatively long time to thoroughly expose the electrode sites [166].

When the number of layers in a hybrid system increases, the probability of delamination and failure of the device will increase. To simplify the current FFA, it is worth exploring other materials to bond with hydrogel. For example, the photo-sensitive polyimide can potentially function as both the substrate for electrodes and interface for hydrogel [96]. On the other hand, fabricating flexible electrodes on PDMS using novel materials can avoid the use of polyimide as the intermediate layer [106], [192].

Future optimization of the current FFA can improve the stimulation resolution and longevity of the device. The hydrogel hybrid system is a platform that allows integration with different devices, providing better conformability and wider coverage for current devices.

5.2.2 Broad applications in neural interfaces

Many neural interfaces desire conformable electrode arrays. For example, the peripheral nerve cuff has used smart polymers to conform to a curved surface and adapt to the peripheral

nerve [28], [29], [31]. Using hydrogel as the active actuator to form a 3D surface instead of shape memory polymers guarantees not only the softness but also offers a wide selection of stimuli [178]. In addition to moisture, light, biomolecules, and electrical field can function as the trigger of reconfiguration. Therefore, the responsive electrode array with hydrogel can be compact to facilitate the surgical procedures, then conform to the surface as needed. Organs with organic curvature such as the heart, the bladder, the peripheral nerves can all take advantage from this design. Furthermore, more complicated shapes other than continuous 3D curves are possible to adapt to more complicated surfaces [92].

Hydrogel-hybrid-based shape-morphable electrode arrays have broad applications in other neural interfaces. This thesis may provide insights to researchers developing neural interfaces that are conformable and minimally invasive.

Bibliography

[1] S. F. Cogan, "Neural Stimulation and Recording Electrodes," *Annu. Rev. Biomed. Eng.*, vol. 10, no. 1, pp. 275–309, 2008.

[2] C. Marquez-Chin and M. R. Popovic, "Functional electrical stimulation therapy for restoration of motor function after spinal cord injury and stroke: A review," *Biomed. Eng. Online*, vol. 19, no. 1, pp. 1–25, 2020.

[3] R. Chen, A. Canales, and P. Anikeeva, "Neural recording and modulation technologies," *Nat. Rev. Mater.*, vol. 2, no. 2, pp. 1–16, 2017.

[4] P. M. Lewis, R. H. Thomson, J. V. Rosenfeld, and P. B. Fitzgerald, "Brain Neuromodulation Techniques: A Review," *Neuroscientist*, vol. 22, no. 4, pp. 406–421, 2016.

[5] A. Jackson and J. B. Zimmermann, "Neural interfaces for the brain and spinal cord - Restoring motor function," *Nat. Rev. Neurol.*, vol. 8, no. 12, pp. 690–699, 2012.

[6] J. S. Perlmutter and J. W. Mink, "Deep brain stimulation," *Annu. Rev. Neurosci.*, vol. 29, pp. 229–257, 2006.

[7] S. F. Lempka and P. G. Patil, "Innovations in spinal cord stimulation for pain," *Curr. Opin. Biomed. Eng.*, vol. 8, pp. 51–60, 2018.

[8] A. A. Eshraghi, R. Nazarian, F. F. Telischi, S. M. Rajguru, E. Truy, and C. Gupta, "The Cochlear Implant: Historical Aspects and Future Prospects," *Anat. Rec.*, vol. 295, no. 11, pp. 1967–1980, 2012.

[9] D. L. Cheng, P. B. Greenberg, and D. A. Borton, "Advances in Retinal Prosthetic Research: A Systematic Review of Engineering and Clinical Characteristics of Current Prosthetic Initiatives," *Curr. Eye Res.*, vol. 42, no. 3, pp. 334–347, 2017.

[10] K. E. Jones, P. K. Campbell, and R. A. Normann, "A glass/silicon composite intracortical electrode array," *Ann. Biomed. Eng.*, vol. 20, no. 4, pp. 423–437, 1992.

[11] K. D. Wise, J. B. Angell, and A. Starr, "An Integrated-Circuit Approach to Extracellular Microelectrodes," *IEEE Trans. Biomed. Eng.*, vol. BME-17, no. 3, pp. 238–247, 1970.

[12] M. A. Hopcroft, W. D. Nix, and T. W. Kenny, "What is the Young's modulus of silicon?," *J. Microelectromechanical Syst.*, vol. 19, no. 2, pp. 229–238, 2010.

[13] R. Biran, D. C. Martin, and P. A. Tresco, "Neuronal cell loss accompanies the brain tissue response to chronically implanted silicon microelectrode arrays," *Exp. Neurol.*, vol. 195, no. 1, pp. 115–126, 2005.

[14] T. EJ, "Electrical stimulation of neural tissue to evoke behavioral responses," *J. Neurosci. Methods*, vol. 65 VN-r, no. 1, pp. 1–17, 1996.

[15] S. A. Bentil and R. B. Dupaix, "Simulations of hydrogel-coated neural microelectrodes to assess biocompatibility improvement using strain as a metric for micromotion," *Biomed. Phys. Eng. Express*, vol. 4, no. 3, 2018.

[16] A. Carnicer-Lombarte, S. T. Chen, G. G. Malliaras, and D. G. Barone, "Foreign Body Reaction to Implanted Biomaterials and Its Impact in Nerve Neuroprosthetics," *Front. Bioeng. Biotechnol.*, vol. 9, no. April, pp. 1–22, 2021.

[17] T. D. Y. Kozai *et al.*, “Mechanical failure modes of chronically implanted planar silicon-based neural probes for laminar recording,” *Biomaterials*, vol. 37, pp. 25–39, 2015.
[18] M. Ferguson, D. Sharma, D. Ross, and F. Zhao, “A Critical Review of Microelectrode Arrays and Strategies for Improving Neural Interfaces,” *Adv. Healthc. Mater.*, vol. 8, no. 19, 2019.
[19] J. Rivnay, H. Wang, L. Fenno, K. Deisseroth, and G. G. Malliaras, “Next-generation probes, particles, and proteins for neural interfacing.,” *Sci. Adv.*, vol. 3, no. 6, p. e1601649, 2017.
[20] J. L. Skousen, M. J. Bridge, and P. A. Tresco, “A strategy to passively reduce neuroinflammation surrounding devices implanted chronically in brain tissue by manipulating device surface permeability,” *Biomaterials*, vol. 36, pp. 33–43, 2015.
[21] P. R. Patel *et al.*, “Insertion of linear 8.4 μm diameter 16 channel carbon fiber electrode arrays for single unit recordings,” *J. Neural Eng.*, vol. 12, no. 4, 2015.
[22] B. Ji *et al.*, “Flexible and stretchable opto-electric neural interface for low-noise electrocorticogram recordings and neuromodulation in vivo,” *Biosens. Bioelectron.*, vol. 153, no. October 2019, p. 112009, 2020.
[23] J. Liu *et al.*, “Syringe-injectable electronics,” *Nat. Nanotechnol.*, vol. 10, no. 7, pp. 629–635, 2015.
[24] G. Schiavone *et al.*, “Soft, Implantable Bioelectronic Interfaces for Translational Research,” *Adv. Mater.*, vol. 32, no. 17, pp. 1–10, 2020.
[25] Y. Shi, R. Liu, L. He, H. Feng, Y. Li, and Z. Li, “Recent Development of Implantable and Flexible Nerve Electrodes,” *Smart Mater. Med.*, vol. 1, no. June, pp. 131–147, 2020.
[26] T. Ware, D. Simon, R. L. Rennaker, and W. Voit, “Smart polymers for neural interfaces,” *Polym. Rev.*, vol. 53, no. 1, pp. 108–129, 2013.
[27] S. M. Won, E. Song, J. Zhao, J. Li, J. Rivnay, and J. A. Rogers, “Recent Advances in Materials, Devices, and Systems for Neural Interfaces,” *Adv. Mater.*, vol. 30, no. 30, 2018.
[28] T. Ware *et al.*, “Three-dimensional flexible electronics enabled by shape memory polymer substrates for responsive neural interfaces,” *Macromol. Mater. Eng.*, vol. 297, no. 12, pp. 1193–1202, 2012.
[29] Y. Zhang *et al.*, “Climbing-inspired twining electrodes using shape memory for peripheral nerve stimulation and recording,” *Sci. Adv.*, vol. 5, no. 4, p. eaaw1066, 2019.
[30] J. Wang, Q. Zhao, Y. Wang, Q. Zeng, T. Wu, and X. Du, “Self-Unfolding Flexible Microelectrode Arrays Based on Shape Memory Polymers,” vol. 1900566, pp. 1–7, 2019.
[31] C. M. Tringides *et al.*, “Viscoelastic surface electrode arrays to interface with viscoelastic tissues,” *Nat. Nanotechnol.*, vol. 16, no. 9, pp. 1019–1029, 2021.
[32] A. Garcia-Sandoval *et al.*, “Chronic softening spinal cord stimulation arrays,” *J. Neural Eng.*, vol. 15, no. 4, p. 045002, 2018.
[33] S. S. Bhattacharya and C. F. Chakarova, “Retinitis Pigmentosa,” *Brenner’s Encycl. Genet. Second Ed.*, vol. 12, pp. 199–203, 2013.
[34] S. K. Verbakel *et al.*, “Non-syndromic retinitis pigmentosa,” *Prog. Retin. Eye Res.*, vol. 66, no. March, pp. 157–186, 2018.
[35] R. R. A. Bourne *et al.*, “Magnitude, temporal trends, and projections of the global prevalence of blindness and distance and near vision impairment: a systematic review and meta-analysis,” *Lancet Glob. Heal.*, vol. 5, no. 9, pp. e888–e897, 2017.
[36] J. Cehajic-Kapetanovic, M. S. Singh, E. Zrenner, and R. E. MacLaren, “Bioengineering strategies for restoring vision,” *Nat. Biomed. Eng.*, 2022.

[37] D. Hartong, E. Berson, and T. Dryja, “Retinitis pigmentosa Prevalence and inheritance patterns,” *Lancet*, vol. 368, pp. 1795–1809, 2006.
[38] A. L. Wang, D. K. Knight, T. T. T. Vu, and M. C. Mehta, “Retinitis pigmentosa: Review of current treatment,” *Int. Ophthalmol. Clin.*, vol. 59, no. 1, pp. 263–280, 2019.
[39] V. Gaillet *et al.*, “Spatially selective activation of the visual cortex via intraneural stimulation of the optic nerve,” *Nat. Biomed. Eng.*, vol. 4, no. 2, pp. 181–194, 2020.
[40] K. Stingl *et al.*, “Subretinal Visual Implant Alpha IMS - Clinical trial interim report,” *Vision Res.*, vol. 111, pp. 149–160, 2015.
[41] M. M. K. Muqit *et al.*, “PRIMA subretinal wireless photovoltaic microchip implantation in non-human primate and feline models,” *PLoS One*, vol. 15, no. 4, pp. 1–16, 2020.
[42] S. Niketeghad and N. Pouratian, “Brain Machine Interfaces for Vision Restoration: The Current State of Cortical Visual Prosthetics,” *Neurotherapeutics*, vol. 16, no. 1, pp. 134–143, 2019.
[43] H. Petrs-Silva and R. Linden, “Advances in gene therapy technologies to treat retinitis pigmentosa,” *Clin. Ophthalmol.*, vol. 8, pp. 127–136, 2013.
[44] J. N. Weiss and S. Levy, “Stem Cell Ophthalmology Treatment Study: Bone marrow derived stem cells in the treatment of Retinitis Pigmentosa,” *Stem Cell Investig.*, vol. 5, no. June, pp. 1–9, 2018.
[45] D. G. Birch, L. D. Bennett, J. L. Duncan, R. G. Weleber, and M. E. Pennesi, “Long-term Follow-up of Patients With Retinitis Pigmentosa Receiving Intraocular Ciliary Neurotrophic Factor Implants,” *Am. J. Ophthalmol.*, vol. 170, pp. 10–14, 2016.
[46] J. L. Duncan *et al.*, “Inherited Retinal Degenerations : Current Landscape and Knowledge Gaps,” vol. 7, no. 4, 2018.
[47] A. T. Fahim, S. P. Daiger, and R. G. Weleber, “Nonsyndromic Retinitis Pigmentosa Overview Clinical Characteristics of Nonsyndromic Retinitis Pigmentosa Clinical Manifestations of Retinitis Pigmentosa,” 2019.
[48] J. D. Weiland, W. Liu, and M. S. Humayun, “Retinal Prosthesis,” *Annu. Rev. Biomed. Eng.*, vol. 7, no. 1, pp. 361–401, 2005.
[49] M. S. Humayun *et al.*, “Interim results from the international trial of second sight’s visual prosthesis,” *Ophthalmology*, vol. 119, no. 4, pp. 779–788, 2012.
[50] L. Da Cruz *et al.*, “The Argus II epiretinal prosthesis system allows letter and word reading and long-term function in patients with profound vision loss,” *Br. J. Ophthalmol.*, vol. 97, no. 5, pp. 632–636, 2013.
[51] E. Zrenner, “Fighting blindness with microelectronics,” *Sci. Transl. Med.*, vol. 5, no. 210, 2013.
[52] R. E. MacLaren, “Electronic retinal implant surgery,” *Eye*, vol. 31, no. 2, pp. 191–195, 2017.
[53] K. Stingl *et al.*, “Subretinal Visual Implant Alpha IMS - Clinical trial interim report,” *Vision Res.*, vol. 111, pp. 149–160, 2015.
[54] D. Palanker, Y. Le Mer, S. Mohand-Said, and J. A. Sahel, “Simultaneous perception of prosthetic and natural vision in AMD patients,” *Nat. Commun.*, vol. 13, no. 1, pp. 1–6, 2022.
[55] Y. Yamauchi *et al.*, “Comparison of electrically evoked cortical potential thresholds generated with subretinal or suprachoroidal placement of a microelectrode array in the rabbit,” *J. Neural Eng.*, vol. 2, no. 1, 2005.

[56] E. Bloch, Y. Luo, and L. da Cruz, "Advances in retinal prosthesis systems," *Ther. Adv. Ophthalmol.*, vol. 11, pp. 1–16, 2019.
[57] L. Yue, V. Wuyyuru, A. Gonzalez-Calle, J. D. Dorn, and M. S. Humayun, "Retina-electrode interface properties and vision restoration by two generations of retinal prostheses in one patient-one in each eye," *J. Neural Eng.*, vol. 17, no. 2, 2020.
[58] H. C. Stronks and G. Dagnelie, "The functional performance of the Argus II retinal prosthesis," *Expert Rev. Med. Devices*, vol. 11, no. 1, pp. 23–30, 2014.
[59] I. Second Sight Medical Products, "Argus II Retinal Prosthesis System Surgeon Manual," *Second Sight Med. Prod. Inc, Sylmar, CA*, 2013.
[60] J. Sommerhalder and A. Pérez Fornos, "Prospects and Limitations of Spatial Resolution," in *Artificial Vision*, 2017, pp. 29–45.
[61] H. Xu *et al.*, "First human results with the 256 channel intelligent micro implant eye (IMIE 256)," *Transl. Vis. Sci. Technol.*, vol. 10, no. 10, pp. 1–12, 2021.
[62] A. M. Sayed *et al.*, "Mobility improvement of patients with peripheral visual field losses using novel see-through digital spectacles," *PLoS One*, vol. 15, no. 10, p. e0240509, 2020.
[63] G. Dagnelie, P. Keane, V. Narla, L. Yang, J. Weiland, and M. Humayun, "Real and virtual mobility performance in simulated prosthetic vision," *J. Neural Eng.*, vol. 4, no. 1, 2007.
[64] M. Beyeler, A. Rokem, G. M. Boynton, and I. Fine, "Learning to see again: Biological constraints on cortical plasticity and the implications for sight restoration technologies," *J. Neural Eng.*, vol. 14, no. 5, 2017.
[65] S. C. Chen, G. J. Suaning, J. W. Morley, and N. H. Lovell, "Simulating prosthetic vision: II. Measuring functional capacity," *Vision Res.*, vol. 49, no. 19, pp. 2329–2343, 2009.
[66] M. Beyeler, D. Nanduri, J. D. Weiland, A. Rokem, G. M. Boynton, and I. Fine, "A model of ganglion axon pathways accounts for percepts elicited by retinal implants," *Sci. Rep.*, vol. 9, no. 1, pp. 1–16, 2019.
[67] A. T. Chuang, C. E. Margo, and P. B. Greenberg, "Retinal implants: A systematic review," *Br. J. Ophthalmol.*, vol. 98, no. 7, pp. 852–856, 2014.
[68] R. H. Spector, "Chap 116 Visual fields," *Clin. methods Hist. Phys. Lab. Exam. 3rd Ed.*, pp. 565–572, 1990.
[69] C. J. Abbott *et al.*, "Safety studies for a 44-channel suprachoroidal retinal prosthesis: A chronic passive study," *Investig. Ophthalmol. Vis. Sci.*, vol. 59, no. 3, pp. 1410–1424, 2018.
[70] L. N. Ayton *et al.*, "An update on retinal prostheses," *Clin. Neurophysiol.*, vol. 131, no. 6, pp. 1383–1398, 2020.
[71] M.-N. Delyfer *et al.*, "Adapted Surgical Procedure for Argus II Retinal Implantation: Feasibility, Safety, Efficiency, and Postoperative Anatomic Findings," *Ophthalmol. Retin.*, vol. 2, no. 4, pp. 276–287, 2017.
[72] A. Ray, L. L. H. Chan, A. Gonzalez, M. S. Humayun, and J. D. Weiland, "Impedance as a method to sense proximity at the electrode-retina interface," *IEEE Trans. Neural Syst. Rehabil. Eng.*, vol. 19, no. 6, pp. 696–699, 2011.
[73] E. D. Demaine, M. L. Demaine, J. Iacono, and S. Langerman, "Wrapping spheres with flat paper," *Comput. Geom. Theory Appl.*, vol. 42, no. 8, pp. 748–757, 2009.
[74] H. Ameri, T. Ratanapakorn, S. Ufer, H. Eckhardt, M. S. Humayun, and J. D. Weiland, "Toward a wide-field retinal prosthesis," *J. Neural Eng.*, vol. 6, no. 3, 2009.
[75] F. Waschkowski *et al.*, "Development of very large electrode arrays for epiretinal stimulation (VLARS)," *Biomed. Eng. Online*, vol. 13, no. 1, pp. 1–15, 2014.

[76] C. Choi *et al.*, “Human eye-inspired soft optoelectronic device using high-density MoS2-graphene curved image sensor array,” *Nat. Commun.*, vol. 8, no. 1, 2017.
[77] Y. Liu *et al.*, “Parylene origami structure for introcular implantation,” *2013 Transducers Eurosensors XXVII 17th Int. Conf. Solid-State Sensors, Actuators Microsystems, TRANSDUCERS EUROSENSORS 2013*, no. June, pp. 1549–1552, 2013.
[78] L. Ferlauto *et al.*, “Design and validation of a foldable and photovoltaic wide-field epiretinal prosthesis,” *Nat. Commun.*, vol. 9, no. 1, p. 992, 2018.
[79] J. Wang, Q. Zhao, H. Cui, Y. Wang, H. Chen, and X. Du, “Tunable shape memory polymer mold for multiple microarray replications,” *J. Mater. Chem. A*, vol. 6, no. 48, pp. 24748–24755, 2018.
[80] Z. Xia, “Biomimetic Principles and Design of Advanced Engineering Materials,” 2016.
[81] R. M. Erb, J. S. Sander, R. Grisch, and A. R. Studart, “Self-shaping composites with programmable bioinspired microstructures,” *Nat. Commun.*, vol. 4, pp. 1–8, 2013.
[82] M. D. Hager, S. Bode, C. Weber, and U. S. Schubert, “Shape memory polymers: Past, present and future developments,” *Prog. Polym. Sci.*, vol. 49–50, pp. 3–33, 2015.
[83] C. Ma *et al.*, “Bioinspired Anisotropic Hydrogel Actuators with On–Off Switchable and Color-Tunable Fluorescence Behaviors,” *Adv. Funct. Mater.*, vol. 28, no. 7, 2018.
[84] H. J. Huang, Y. L. Tsai, S. H. Lin, and S. H. Hsu, “Smart polymers for cell therapy and precision medicine,” *J. Biomed. Sci.*, vol. 26, no. 1, pp. 1–11, 2019.
[85] M. R. Pfau and M. A. Grunlan, “Smart scaffolds: shape memory polymers (SMPs) in tissue engineering,” *J. Mater. Chem. B*, vol. 9, no. 21, pp. 4287–4297, 2021.
[86] J. Kunzelman, T. Chung, P. T. Mather, and C. Weder, “Shape memory polymers with built-in threshold temperature sensors,” *J. Mater. Chem.*, vol. 18, no. 10, pp. 1082–1086, 2008.
[87] A. Kirillova and L. Ionov, “Shape-changing polymers for biomedical applications,” *J. Mater. Chem. B*, vol. 7, no. 10, pp. 1597–1624, 2019.
[88] V. Bansal, P. K. Sharma, N. Sharma, O. P. Pal, and R. Malviya, *Shape-Memory Polymers*, vol. 226. 2010.
[89] J. Wang, Q. Zhao, Y. Wang, Q. Zeng, T. Wu, and X. Du, “Shape-Programmable Electronics: Self-Unfolding Flexible Microelectrode Arrays Based on Shape Memory Polymers (Adv. Mater. Technol. 11/2019),” *Adv. Mater. Technol.*, vol. 4, no. 11, p. 1970063, 2019.
[90] Y. Liu *et al.*, “Morphing electronics enable neuromodulation in growing tissue,” *Nat. Biotechnol.*, vol. 38, no. 9, pp. 1031–1036, 2020.
[91] X. Peng and H. Wang, “Shape changing hydrogels and their applications as soft actuators,” *J. Polym. Sci. Part B Polym. Phys.*, vol. 56, no. 19, pp. 1314–1324, 2018.
[92] O. Erol, A. Pantula, W. Liu, and D. H. Gracias, “Transformer Hydrogels: A Review,” *Adv. Mater. Technol.*, vol. 4, no. 4, pp. 1–27, 2019.
[93] D. H. Gracias, “Stimuli responsive self-folding using thin polymer films,” *Curr. Opin. Chem. Eng.*, vol. 2, no. 1, pp. 112–119, 2013.
[94] H. Yuk, T. Zhang, G. A. Parada, X. Liu, and X. Zhao, “Skin-inspired hydrogel-elastomer hybrids with robust interfaces and functional microstructures,” *Nat. Commun.*, vol. 7, no. May, pp. 1–11, 2016.
[95] S. Liu, E. Boatti, K. Bertoldi, and R. Kramer-Bottiglio, “Stimuli-induced bi-directional hydrogel unimorph actuators,” *Extrem. Mech. Lett.*, vol. 21, pp. 35–43, 2018.

[96] D. Karnaushenko, D. D. Karnaushenko, D. Makarov, S. Baunack, R. Schäfer, and O. G. Schmidt, "Self-Assembled On-Chip-Integrated Giant Magneto-Impedance Sensorics," *Adv. Mater.*, vol. 27, no. 42, pp. 6582–6589, 2015.
[97] J. Viventi *et al.*, "Flexible, foldable, actively multiplexed, high-density electrode array for mapping brain activity in vivo," *Nat. Neurosci.*, vol. 14, no. 12, pp. 1599–1605, 2011.
[98] L. Xu *et al.*, "Materials and fractal designs for 3D multifunctional integumentary membranes with capabilities in cardiac electrotherapy," *Adv. Mater.*, vol. 27, no. 10, pp. 1731–1737, 2015.
[99] J. A. Rogers, T. Someya, Y. Huang, J. A. Rogers, T. Someya, and Y. Huang, "Materials and Mechanics for Stretchable Electronics," vol. 327, no. 5973, pp. 1603–1607, 2010.
[100] I. R. Minev *et al.*, "Electronic dura mater for long-term multimodal neural interfaces," *Science (80-.).*, vol. 347, no. 6218, pp. 159–163, 2015.
[101] A. Victor, J. Ribeiro, and F. F. Araújo, "Study of PDMS characterization and its applications in biomedicine: A review," *J. Mech. Eng. Biomech.*, vol. 4, no. 1, pp. 1–9, 2019.
[102] R. Seghir and S. Arscott, "Controlled mud-crack patterning and self-organized cracking of polydimethylsiloxane elastomer surfaces," *Sci. Rep.*, vol. 5, no. October, pp. 1–16, 2015.
[103] T. Adrega and S. P. Lacour, "Stretchable gold conductors embedded in PDMS and patterned by photolithography: Fabrication and electromechanical characterization," *J. Micromechanics Microengineering*, vol. 20, no. 5, 2010.
[104] M. Shur *et al.*, "Soft Printable Electrode Coating for Neural Interfaces," *ACS Appl. Bio Mater.*, vol. 3, no. 7, pp. 4388–4397, 2020.
[105] D. Yan *et al.*, "Ultracompliant Carbon Nanotube Direct Bladder Device," *Adv. Healthc. Mater.*, vol. 8, no. 20, pp. 1–11, 2019.
[106] F. Xu and Y. Zhu, "Highly conductive and stretchable silver nanowire conductors," *Adv. Mater.*, vol. 24, no. 37, pp. 5117–5122, 2012.
[107] D. Afanasenkau *et al.*, "Rapid prototyping of soft bioelectronic implants for use as neuromuscular interfaces," *Nat. Biomed. Eng.*, vol. 4, no. 10, pp. 1010–1022, 2020.
[108] Z. Yan *et al.*, "Thermal Release Transfer Printing for Stretchable Conformal Bioelectronics," *Adv. Sci.*, vol. 4, no. 11, 2017.
[109] Z. Pu *et al.*, "A flexible precise volume sensor based on metal-on-polyimide electrodes sandwiched by PDMS channel for microfluidic systems," *Microfluid. Nanofluidics*, vol. 23, no. 12, pp. 1–11, 2019.
[110] J. H. Moon, D. H. Baek, Y. Y. Choi, K. H. Lee, H. C. Kim, and S. H. Lee, "Wearable polyimide-PDMS electrodes for intrabody communication," *J. Micromechanics Microengineering*, vol. 20, no. 2, 2010.
[111] M. Zhou, D. H. Kang, J. Kim, and J. D. Weiland, "Shape morphable hydrogel/elastomer bilayer for implanted retinal electronics," *Micromachines*, vol. 11, no. 4, p. 392, 2020.
[112] L. Montero De Espinosa, W. Meesorn, D. Moatsou, and C. Weder, "Bioinspired Polymer Systems with Stimuli-Responsive Mechanical Properties," *Chem. Rev.*, vol. 117, no. 20, pp. 12851–12892, 2017.
[113] L. Ionov, "Bioinspired microorigami by self-folding polymer films," *Macromol. Chem. Phys.*, vol. 214, no. 11, pp. 1178–1183, 2013.
[114] M. A. C. Stuart *et al.*, "Emerging applications of stimuli-responsive polymer materials," *Nat. Mater.*, vol. 9, no. 2, pp. 101–113, 2010.

[115] L. Ionov, “Actuating Hydrogel Thin Films,” in *Responsive Polymer Surfaces: Dynamics in Surface Topography*, 2017, pp. 137–157.
[116] W. Xu *et al.*, “Ultrathin thermoresponsive self-folding 3D graphene,” *Sci. Adv.*, vol. 3, no. 10, 2017.
[117] G. Stoychev, N. Puretskiy, and L. Ionov, “Self-folding all-polymer thermoresponsive microcapsules,” *Soft Matter*, vol. 7, no. 7, pp. 3277–3279, 2011.
[118] L. Vannozzi, I. C. Yasa, H. Ceylan, A. Menciassi, L. Ricotti, and M. Sitti, “Self-Folded Hydrogel Tubes for Implantable Muscular Tissue Scaffolds,” *Macromol. Biosci.*, vol. 18, no. 4, pp. 1–9, 2018.
[119] H. Li, G. Go, S. Y. Ko, J. O. Park, and S. Park, “Magnetic actuated pH-responsive hydrogel-based soft micro-robot for targeted drug delivery,” *Smart Mater. Struct.*, vol. 25, no. 2, 2016.
[120] X. Li, X. Cai, Y. Gao, and M. J. Serpe, “Reversible bidirectional bending of hydrogel-based bilayer actuators,” *J. Mater. Chem. B*, vol. 5, no. 15, pp. 2804–2812, 2017.
[121] V. Magdanz, G. Stoychev, L. Ionov, S. Sanchez, and O. G. Schmidt, “Stimuli-responsive microjets with reconfigurable shape,” *Angew. Chemie - Int. Ed.*, vol. 53, no. 10, pp. 2673–2677, 2014.
[122] Y. Ma, Y. Zhang, B. Wu, W. Sun, Z. Li, and J. Sun, “Polyelectrolyte multilayer films for building energetic walking devices,” *Angew. Chemie - Int. Ed.*, vol. 50, no. 28, pp. 6254–6257, 2011.
[123] J. Macron, A. P. Gerratt, and S. P. Lacour, “Thin Hydrogel–Elastomer Multilayer Encapsulation for Soft Electronics,” *Adv. Mater. Technol.*, vol. 1900331, p. 1900331, 2019.
[124] C. Yu *et al.*, “Electronically programmable, reversible shape change in two- and three-dimensional hydrogel structures,” *Adv. Mater.*, vol. 25, no. 11, pp. 1541–1546, 2013.
[125] X. Li, S. Lin, J. Liang, Y. Zhang, H. Oigawa, and T. Ueda, “Fiber-optic temperature sensor based on difference of thermal expansion coefficient between fused silica and metallic materials,” *IEEE Photonics J.*, vol. 4, no. 1, pp. 155–162, 2012.
[126] S. K. T. Ravindran, M. Kroener, and P. Woias, “A bimetallic micro heat engine for pyroelectric energy conversion,” *Procedia Eng.*, vol. 47, no. 1, pp. 33–36, 2012.
[127] E. M. White, J. Yatvin, J. B. Grubbs, J. A. Bilbrey, and J. Locklin, “Advances in smart materials: Stimuli-responsive hydrogel thin films,” *J. Polym. Sci. Part B Polym. Phys.*, vol. 51, no. 14, pp. 1084–1099, 2013.
[128] J. Kim, C. Kim, Y. S. Song, S. G. Jeong, T. S. Kim, and C. S. Lee, “Reversible self-bending soft hydrogel microstructures with mechanically optimized designs,” *Chem. Eng. J.*, vol. 321, pp. 384–393, 2017.
[129] G. Stoychev, S. Zakharchenko, S. Turcaud, J. W. C. Dunlop, and L. Ionov, “Shape-programmed folding of stimuli-responsive polymer bilayers,” *ACS Nano*, vol. 6, no. 5, pp. 3925–3934, 2012.
[130] J. P. Baker, L. H. Hong, H. W. Blanch, and J. M. Prausnitz, “Effect of Initial Total Monomer Concentration on the Swelling Behavior of Cationic Acrylamide-Based Hydrogels,” *Macromolecules*, vol. 27, no. 6, pp. 1446–1454, 1994.
[131] J. Baselga, I. Hernández-Fuentes, I. F. Piérola, and M. A. Llorente, “Elastic Properties of Highly Cross-Linked Polyacrylarnide Gels,” *Macromolecules*, vol. 20, no. 12, pp. 3060–3065, 1987.

[132] N. Weiss, T. Van Vliet, and A. Silberberg, “Influence of Polymerization Initiation Rate on Permeability of Aqueous Polyacrylamide Gels.,” *J. Polym. Sci. Part A-2, Polym. Phys.*, vol. 19, no. 10, pp. 1505–1512, 1981.
[133] S. Sheth, E. Jain, A. Karadaghy, S. Syed, H. Stevenson, and S. P. Zustiak, “UV Dose Governs UV-Polymerized Polyacrylamide Hydrogel Modulus,” *Int. J. Polym. Sci.*, vol. 2017, 2017.
[134] X. Zhao, T. Supervisor, and R. Abeyaratne, “Tough Wet Adhesion of Hydrogel on Various Materials - Mechanism and Application Tough Wet Adhesion of Hydrogel on Various Materials - Mechanism and Application,” pp. 1–87, 2016.
[135] T. Fujie, A. Desii, L. Ventrelli, B. Mazzolai, and V. Mattoli, “Inkjet printing of protein microarrays on freestanding polymeric nanofilms for spatio-selective cell culture environment,” *Biomed. Microdevices*, vol. 14, no. 6, pp. 1069–1076, 2012.
[136] S. Alam, G. M. A. Khan, S. M. A. Razzaque, M. N. Alam, and M. I. H. Mondal, “Swelling property of the polyacrylamide hydrogel prepared by γ-ray irradiation,” *J. Polym. Mater.*, vol. 25, no. 4, pp. 645–651, 2008.
[137] N. Orakdogen and O. Okay, “Effect of initial monomer concentration on the equilibrium swelling and elasticity of hydrogels,” *Eur. Polym. J.*, vol. 42, no. 4, pp. 955–960, 2006.
[138] M. Y. Kizilay and O. Okay, “Effect of initial monomer concentration on spatial inhomogeneity in poly(acrylamide) gels,” *Macromolecules*, vol. 36, no. 18, pp. 6856–6862, 2003.
[139] B. Y. S. Timoshenko, “Analysis of bi-metal thermostats,” no. l, pp. 233–255.
[140] W. Guo, M. Li, and J. Zhou, “Modeling programmable deformation of self-folding all-polymer structures with temperature-sensitive hydrogels,” *Smart Mater. Struct.*, vol. 22, no. 11, 2013.
[141] M. D. B. Reinhard Rüchel, “Scanning electron microscopic observations of polyacrylamide gels,” *Anal. Biochem.*, vol. 68, no. 2, pp. 415–428, 1975.
[142] J. E. Lovie-Kitchin, G. P. Soonng, S. E. Hassan, and R. L. Woods, “Visual Field Size Criteria for Mobility,” *Optom. Vis. Sci.*, vol. 87, no. 12, pp. 948–957, 2010.
[143] G. Yin, Y. X. Wang, Z. Y. Zheng, H. Yang, L. Xu, and J. B. Jonas, “Ocular axial length and its associations in Chinese: The Beijing eye study,” *PLoS One*, vol. 7, no. 8, 2012.
[144] J. Thiel and G. Maurer, “Swelling equilibrium of poly(acrylamide) gels in aqueous salt and polymer solutions,” *Fluid Phase Equilib.*, vol. 165, no. 2, pp. 225–260, 1999.
[145] A. K. Ahuja *et al.*, “Factors Affecting Perceptual Threshold in Argus II Retinal Prosthesis Subjects,” *Transl. Vis. Sci. Technol.*, vol. 2, no. 4, p. 1, 2013.
[146] Elias Greenbaum & David Zhou, *Implantable Neural Prostheses 1*. 2009.
[147] A. Petrossians, J. J. Whalen III, J. D. Weiland, and F. Mansfeld, “Electrodeposition and Characterization of Thin-Film Platinum-Iridium Alloys for Biological Interfaces,” *J. Electrochem. Soc.*, vol. 158, no. 5, p. D269, 2011.
[148] C. De Balthasar *et al.*, “Factors affecting perceptual thresholds in epiretinal prostheses,” *Investig. Ophthalmol. Vis. Sci.*, vol. 49, no. 6, pp. 2303–2314, 2008.
[149] R. K. Shamsudeen, S. Nair, and V. G. Jayakumari, “Equilibrium swelling, conductivity and electroactive characteristics of polyacrylamide hydrogels,” *Indian J. Eng. Mater. Sci.*, vol. 13, no. 1, pp. 62–68, 2006.
[150] N. Chou, J. Jeong, and S. Kim, “Crack-free and reliable lithographical patterning methods on PDMS substrate,” *J. Micromechanics Microengineering*, vol. 23, no. 12, 2013.

[151] N. Bowden, S. Brittain, A. G. Evans, J. W. Hutchinson, and G. M. Whitesides, "Spontaneous formation of ordered structures in thin films of metals supported on an elastomeric polymer," *Nature*, vol. 393, no. 6681, pp. 146–149, 1998.
[152] E. L. Berson, "Retinitis pigmentosa: The Friedenwald lecture," *Investig. Ophthalmol. Vis. Sci.*, vol. 34, no. 5, pp. 1659–1676, 1993.
[153] P. Herse, "Retinitis pigmentosa: visual function and multidisciplinary management," *Clin. Exp. Optom.*, vol. 88, no. 5, pp. 335–350, 2005.
[154] H. Ameri, T. Ratanapakorn, S. Ufer, H. Eckhardt, M. S. Humayun, and J. D. Weiland, "Toward a wide-field retinal prosthesis," *J. Neural Eng.*, vol. 6, no. 3, 2009.
[155] J. Rivnay, H. Wang, L. Fenno, K. Deisseroth, and G. G. Malliaras, "Next-generation probes, particles, and proteins for neural interfacing," *Sci. Adv.*, vol. 3, no. 6, pp. 1–20, 2017.
[156] X. Li *et al.*, "PDMS-Parylene Hybrid, Flexible Micro-ECoG Electrode Array for Spatiotemporal Mapping of Epileptic Electrophysiological Activity from Multicortical Brain Regions," *ACS Appl. Bio Mater.*, vol. 4, no. 11, pp. 8013–8022, 2021.
[157] K. Y. Lee *et al.*, "Development of a Polydimethylsiloxane-Based Electrode Array for Electrocorticography," *Adv. Mater. Interfaces*, vol. 7, no. 24, 2020.
[158] J. N. Lee, C. Park, and G. M. Whitesides, "Solvent Compatibility of Poly(dimethylsiloxane)-Based Microfluidic Devices," *Anal. Chem.*, vol. 75, no. 23, pp. 6544–6554, 2003.
[159] D. W. Lee and J. S. Park, "Feasibility study of PDMS-based thermal microactuators," *Sensors Mater.*, vol. 19, no. 8, pp. 497–504, 2007.
[160] L. Guo, K. W. Meacham, S. Hochman, and Stephen P. DeWeerth, "A PDMS-Based Conical-Well Microelectrode Array for Surface Stimulation and Recording of Neural Tissues," *IEEE Trans Biomed Eng*, vol. 57, no. 10, pp. 2485–2494, 2010.
[161] B. Balakrisnan, S. Patil, and E. Smela, "Patterning PDMS using a combination of wet and dry etching," *J. Micromechanics Microengineering*, vol. 19, no. 4, 2009.
[162] Y. Chen, W. Pei, R. Tang, S. Chen, and H. Chen, "Conformal coating of parylene for surface anti-adhesion in polydimethylsiloxane (PDMS) double casting technique," *Sensors Actuators, A Phys.*, vol. 189, pp. 143–150, 2013.
[163] C. Hassler, R. P. Von Metzen, P. Ruther, and T. Stieglitz, "Characterization of parylene C as an encapsulation material for implanted neural prostheses," *J. Biomed. Mater. Res. - Part B Appl. Biomater.*, vol. 93, no. 1, pp. 266–274, 2010.
[164] H. G. Park, H. C. Jeong, Y. H. Jung, and D. S. Seo, "Control of the wrinkle structure on surface-reformed poly(dimethylsiloxane) via ion-beam bombardment," *Sci. Rep.*, vol. 5, no. July, pp. 1–8, 2015.
[165] J. Garra, T. Long, J. Currie, T. Schneider, R. White, and M. Paranjape, "Dry etching of polydimethylsiloxane for microfluidic systems," *J. Vac. Sci. Technol. A Vacuum, Surfaces, Film.*, vol. 20, no. 3, pp. 975–982, 2002.
[166] K. W. Meacham, R. J. Giuly, L. Guo, S. Hochman, and S. P. DeWeerth, "A lithographically-patterned, elastic multi-electrode array for surface stimulation of the spinal cord," *Biomed. Microdevices*, vol. 10, no. 2, pp. 259–269, Apr. 2008.
[167] N. Lucas, S. Demming, A. Jordan, P. Sichler, and S. Büttgenbach, "An improved method for double-sided moulding of PDMS," *J. Micromechanics Microengineering*, vol. 18, no. 7, 2008.

[168] M. Schuettler, C. Henle, J. Ordonez, G. J. Suaning, N. H. Lovell, and T. Stieglitz, "Patterning of silicone rubber for micro-electrode array fabrication," *Proc. 3rd Int. IEEE EMBS Conf. Neural Eng.*, pp. 53–56, 2007.
[169] J. M. Kim, D. R. Oh, J. Sanchez, S. H. Kim, and J. M. Seo, "Fabrication of polydimethylsiloxane (PDMS) - Based multielectrode array for neural interface," *Proc. Annu. Int. Conf. IEEE Eng. Med. Biol. Soc. EMBS*, pp. 1716–1719, 2013.
[170] L. Guo, K. W. Meacham, S. Hochman, and S. P. DeWeerth, "A PDMS-based conical-well microelectrode array for surface stimulation and recording of neural tissues," *IEEE Trans. Biomed. Eng.*, vol. 57, no. 10 PART 1, pp. 2485–2494, 2010.
[171] S. Rezaei, Y. Xu, and S. W. Pang, "Control of neural probe shank flexibility by fluidic pressure in embedded microchannel using PDMS/PI hybrid substrate," *PLoS One*, vol. 14, no. 7, pp. 1–15, 2019.
[172] M. A. Eddings, M. A. Johnson, and B. K. Gale, "Determining the optimal PDMS-PDMS bonding technique for microfluidic devices," *J. Micromechanics Microengineering*, vol. 18, no. 6, 2008.
[173] D. Borton, S. Micera, J. Del R. Millán, and G. Courtine, "Personalized neuroprosthetics," *Sci. Transl. Med.*, vol. 5, no. 210, 2013.
[174] S. Rizzo, L. Cinelli, L. Finocchio, R. Tartaro, F. Santoro, and N. Z. Gregori, "Assessment of Postoperative Morphologic Retinal Changes by Optical Coherence Tomography in Recipients of an Electronic Retinal Prosthesis Implant," *JAMA Ophthalmol.*, vol. 137, no. 3, pp. 272–278, 2019.
[175] T. Ware, D. Simon, K. Hearon, T. H. Kang, D. J. Maitland, and W. Voit, "Thiol-click chemistries for responsive neural interfaces," *Macromol. Biosci.*, vol. 13, no. 12, pp. 1640–1647, 2013.
[176] S. J. Jeon, A. W. Hauser, and R. C. Hayward, "Shape-Morphing Materials from Stimuli-Responsive Hydrogel Hybrids," *Acc. Chem. Res.*, vol. 50, no. 2, pp. 161–169, 2017.
[177] H. Yuk, B. Lu, and X. Zhao, "Hydrogel bioelectronics," *Chem. Soc. Rev.*, vol. 48, no. 6, pp. 1642–1667, 2019.
[178] X. Liu, J. Liu, S. Lin, and X. Zhao, "Hydrogel machines," *Mater. Today*, vol. xxx, no. xx, pp. 14–19, 2020.
[179] E. della Valle *et al.*, "Electrodeposited Platinum Iridium Enables Microstimulation With Carbon Fiber Electrodes," *Front. Nanotechnol.*, vol. 3, no. December, pp. 1–11, 2021.
[180] T. Ratanapakorn, H. Ameri, M. S. Humayun, and J. D. Weiland, "Enucleated eye model for intraocular retinal prosthesis implantation," *Ophthalmic Surg. Lasers Imaging*, vol. 37, no. 4, pp. 341–343, 2006.
[181] V. Bhardwaj and G. P. Rajeshbhai, "Axial length, anterior chamber depth-a study in different age groups and refractive errors," *J. Clin. Diagnostic Res.*, vol. 7, no. 10, pp. 2211–2212, 2013.
[182] D. S. Holder and A. Khan, "Use of polyacrylamide gels in a saline-filled tank to determine the linearity of the Sheffield Mark 1 electrical impedance tomography (EIT) system in measuring impedance disturbances," *Physiol. Meas.*, vol. 15, no. 2A, 1994.
[183] J. Yoon, S. Cai, Z. Suo, and R. C. Hayward, "Poroelastic swelling kinetics of thin hydrogel layers: Comparison of theory and experiment," *Soft Matter*, vol. 6, no. 23, pp. 6004–6012, 2010.
[184] B. Chollet *et al.*, "Multiscale Surface-Attached Hydrogel Thin Films with Tailored Architecture," *ACS Appl. Mater. Interfaces*, vol. 8, no. 18, pp. 11729–11738, 2016.

[185] R. Taschner, P. Gauss, P. Knaack, and R. Liska, “Biocompatible photoinitiators based on poly-α-ketoesters,” *J. Polym. Sci.*, vol. 58, no. 2, pp. 242–253, 2020.
[186] F. Yanagawa, S. Sugiura, and T. Kanamori, “Hydrogel microfabrication technology toward three dimensional tissue engineering,” *Regen. Ther.*, vol. 3, pp. 45–57, 2016.
[187] R. Sevinç Özakar and E. Özakar, “Current overview of oral thin films,” *Turkish J. Pharm. Sci.*, vol. 18, no. 1, pp. 111–121, 2021.
[188] P. W. S. H. Lai Wah Chan Jin Song Hao, “Evaluation of Permeability and Mechanical Properties of Composite Polyvinyl Alcohol Films,” *Chem. Pharm. Bull.*, vol. 47, no. 10, pp. 1412–1416, 1999.
[189] S. Srinivasan *et al.*, “Polyimide Electrode-Based Electrical Stimulation Impedes Early Stage Muscle Graft Regeneration,” *Front. Neurol.*, vol. 10, no. March, 2019.
[190] T. L. Massey, J. R. Gleick, and R. U. M. Haque, “Automated Multiplexed Potentiostat System (AMPS) for High-Throughput Characterization of Neural Interfaces,” *BioCAS 2021 - IEEE Biomed. Circuits Syst. Conf. Proc.*, pp. 2–6, 2021.
[191] A. Ahnood *et al.*, “Diamond Devices for High Acuity Prosthetic Vision,” *Adv. Biosyst.*, vol. 1, no. 1–2, pp. 1–10, 2017.
[192] K. Tybrandt *et al.*, “High-Density Stretchable Electrode Grids for Chronic Neural Recording,” *Adv. Mater.*, vol. 30, no. 15, 2018.